https://lib.uliege.be https://matheo.uliege.be

Mémoire

Auteur : Mamoudou Taganga, Samsia
Promoteur(s) : Bousquet, Eric
Faculté : Faculté des Sciences
Diplôme : Master en sciences physiques, à finalité approfondie
Année académique : 2024-2025
URI/URL : http://hdl.handle.net/2268.2/22964

Avertissement à l'attention des usagers :

Tous les documents placés en accès ouvert sur le site le site MatheO sont protégés par le droit d'auteur. Conformément aux principes énoncés par la "Budapest Open Access Initiative"(BOAI, 2002), l'utilisateur du site peut lire, télécharger, copier, transmettre, imprimer, chercher ou faire un lien vers le texte intégral de ces documents, les disséquer pour les indexer, s'en servir de données pour un logiciel, ou s'en servir à toute autre fin légale (ou prévue par la réglementation relative au droit d'auteur). Toute utilisation du document à des fins commerciales est strictement interdite.

Par ailleurs, l'utilisateur s'engage à respecter les droits moraux de l'auteur, principalement le droit à l'intégrité de l'oeuvre et le droit de paternité et ce dans toute utilisation que l'utilisateur entreprend. Ainsi, à titre d'exemple, lorsqu'il reproduira un document par extrait ou dans son intégralité, l'utilisateur citera de manière complète les sources telles que mentionnées ci-dessus. Toute utilisation non explicitement autorisée ci-avant (telle que par exemple, la modification du document ou son résumé) nécessite l'autorisation préalable et expresse des auteurs ou de leurs ayants droit.

University of Liège

Faculty of Sciences – Department of Physics

Can chirality in materials be a new order parameter?

Author:
Samsia Mamoudou Taganga

Promoter:
Dr. Eric Bousquet

Reading Committee:

Dr. François Damanet
Dr. Stéphane Dorbolo
Prof. Philippe Ghosez

Master's thesis submitted in fulfilment of the requirements
for the Master's degree in Physical Sciences

Academic Year 2024–2025

Acknowledgements

First, I would like to sincerely thank my supervisor, Dr. Eric Bousquet, for his continuous support, insightful guidance, and constructive feedback throughout this work. His expertise and availability were instrumental in shaping the direction of this thesis.

I also extend my gratitude to Prof. F. Damanet, Prof. S. Dorbolo, and Prof. P. Ghosez for accepting to be part of my reading committee and for their valuable insights.

I would like to warmly thank M. Braun, F. Gómez-Ortiz, and A. Zabalo Alonso for their assistance, productive discussions, and generous advice throughout the different steps of this project.

The computational work was possible thanks to the computational resources provided by the Consortium des Équipements de Calcul Intensif (CÉCI).

Last but not least, I am deeply grateful to my friends and family for their constant encouragement, understanding, and support throughout this journey.

Contents

Chapter 1

Introduction

1.1 Introduction

The concept of chirality, which describes objects that cannot be superimposed onto their mirror image, is an omnipresent and important property across many scientific fields [1, 2, 3]. From the handedness of elementary particles in fundamental physics to the specific enantiomeric forms of molecules essential for life in biology and pharmacology, chirality dictates interactions and properties at multiple scales. In the fields of condensed matter physics and materials science, structural chirality in crystalline solids has emerged as a fascinating area of research [1, 4]. It promises many innovative physical phenomena and potential technological applications [5].

Chiral materials can exhibit unique responses to external stimuli, particularly to electromagnetic fields [6]. One of the most direct and well-known consequences of structural chirality is Natural Optical Activity (NOA). NOA is the ability of a material to rotate the plane of polarisation of transmitted light in the absence of external magnetic fields. Beyond NOA, structural chirality has been increasingly associated with other exciting properties. It includes non-linear optical effects, magneto-chiral dichroism, spin-selective transport in spintronic devices, and enantioselective catalysis [4].
As a result, the discovery and design of new chiral materials have become major goals in contemporary materials research. It goes with the desire to have a deeper understanding of how chirality arises and interacts with other physical properties.

This master's thesis explores the fundamental question of whether structural chirality itself can be treated as a primary order parameter in displacive phase transitions. Such transitions are characterised by continuous atomic displacements from a high-symmetry, achiral parent phase to a lower-symmetry, chiral daughter phase. Identifying chirality as an order parameter in this context would offer a powerful theoretical framework. Rooted in Landau theory, it could describe, predict, and possibly control such symmetry-breaking phenomena.

To address this question, this work focuses on tin(II) fluoride (SnF_2) as a representative model system. SnF_2 is known for its rich polymorphism, including experimentally observed chiral phases [7, 8, 9, 10], and the presence of a stereochemically active lone pair on the Sn^{2+} cation. The latter is often a driving force for structural distortions. Using first-principles calculations based on Density Functional Theory (DFT) and Density Functional Perturbation Theory (DFPT), an investigation is conducted on a phonon-driven pathway [11, 12]. It follows a transition from a hypothetical achiral rutile-type parent phase of SnF_2 to its chiral γ-phase. The evolution of structural chirality (quantified by helicity [13]) and its direct physical consequence, natural optical activity, are systematically studied along this transition pathway.

This manuscript is organised as follows: Chapter 2 provides a comprehensive background on the concepts of chirality and optical activity, including their historical development, crystallographic requirements, and methods for their quantification. Chapter 3 explains the theoretical and computational framework behind the first-principles calculations of this work. It focuses on DFT and DFPT. Chapter 4 presents the original research on SnF_2. It includes the characterisation of its polymorphs, the identification of a suitable achiral parent phase, the detailed analysis of the phonon-driven transition to a chiral state, and an investigation into the role of the Sn^{2+} lone pair. Finally, Chapter 5 will summarise the main findings and discuss perspectives for future research.

1.2 Motivations

The central question of this thesis, "*Can chirality in materials be a new order parameter?*", originates from an attempt to extend the understanding of symmetry-breaking mechanisms in solids. While chirality is a familiar concept in chemistry and biology, its emergence in crystals is drawing more and more attention in condensed matter physics.

Conventionally, ferroic orders like ferroelectricity or ferromagnetism are described by a continuous order parameter that evolves across a phase transition. Recent studies suggest that structural chirality might play a similar role in displacive transitions between achiral and chiral phases. As reviewed in depth by Bousquet et al. [4], the idea uncovers the possibility of treating chirality as more than just a geometric feature. It could be a fundamental ordering principle, coupled to measurable responses such as Natural Optical Activity (NOA). Classifying chirality as a ferroic order would imply the potential of switching and controlling it by a conjugate field, opening vast possibilities for new technological applications.

One of the biggest challenges is the definition of a quantitative measure of chirality that is appropriate for periodic solids. In this work, helicity is used as a continuous measurement derived from atomic displacements. It is proposed as a candidate for a chiral order parameter, and its behaviour is studied during a displacive transition.
This approach is supported by recent theoretical studies [11, 12]. They show that phonon instabilities at high-symmetry points can drive transitions from achiral to chiral phases. In such cases, the amplitude of the unstable mode often correlates with the emergence of chirality.

This thesis is motivated by the desire to evaluate whether structural chirality can behave as an order parameter in phonon-driven transitions. It also seeks to study its relation to observable properties like NOA. In addition, it aims to investigate the role of lone-pair electrons in enabling such transitions. The understanding gained from this specific study on SnF is expected to contribute to the broader understanding of chiral phenomena in condensed matter and the development of new parameters to describe phase transitions.

Chapter 2

Chirality and Natural Optical Activity

As mentioned in the introduction, one of the most direct consequences of structural chirality in matter is natural optical activity (NOA). It corresponds to a material rotating the plane of polarisation of transmitted light. This phenomenon is not a curiosity but a fundamental feature of chirality at the macroscopic scale.

This chapter focuses on the exploration of the theoretical framework of chirality and its principal observable consequence, natural optical activity. It will begin by defining chirality and tracing its historical discovery. Then, it explores its connection to crystallographic symmetry and finally details the physical origin of optical activity. These elements are crucial to understanding the central subject of this thesis and will be frequently referred to in later chapters.

2.1 Definition of Chirality

Chirality is a fundamental geometric property describing the asymmetry of an object. It refers to the lack of mirror symmetry in an object. It means that by taking a chiral object and its mirror reflection, it is impossible to superimpose them. The easiest example is the left and right hands. They are each other's image by mirror symmetry. However, it is impossible to overlay them perfectly.

Conversely, an object that can be superimposed onto its mirror image is called *achiral*.

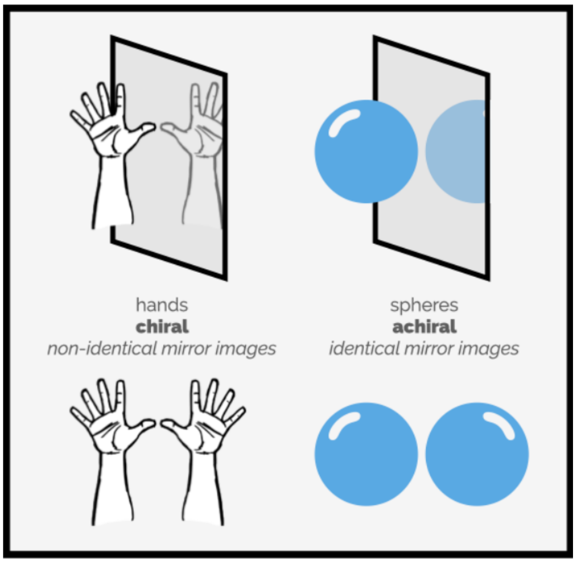

Figure 2.1: Example of chiral and achiral objects (Inspired from [14]). Hands are chiral, as they can be differentiated from each other. This is not the case of a sphere, as the object and its mirror image are identical and superimposable.

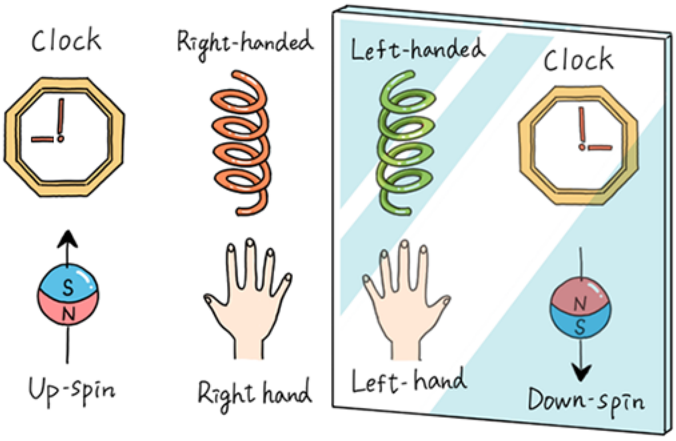

Figure 2.2: This figure illustrates the concept of handedness. On the left side of the image, objects are right-handed, and on the right side, there are left-handed objects. (Inspired by [15]).

In order to classify chiral objects, the notion of *handedness* is used. It was inspired by the notable example of hands as chiral objects. It describes the sense in which an object twists or rotates. A common convention relies on the "right-hand rule": the thumb indicates the axis direction, and the fingers show the direction of rotation. For a helix, if the thumb is pointing upward and the sense of rotation is anticlockwise, the material is *right-handed* or *dextrorotatory*. In the opposite case, it is *left-handed*, *levorotatory*, as shown in Figure 2.2.

Therefore, chirality refers to the absence of mirror symmetry in an object. Handedness separates chiral objects in terms of their orientation [4]. However, the two notions do not necessarily exist together, as shown in Fig. 2.3 below.

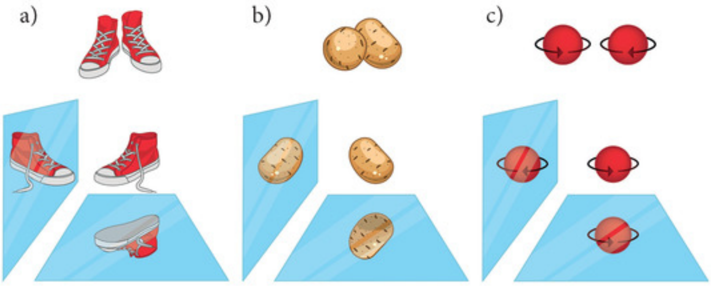

Figure 2.3: A mirror is applied to three types of objects to accentuate the notions of chirality and handedness. a) Shoes are chiral and handed. Both objects are non-superimposable, and it is possible to distinguish a left and a right shoe. b) A potato is chiral but not handed. Once again, both objects are different; however, it is not possible to distinguish a right or a left potato. c) A spinning ball can exhibit a sense and, therefore, be handed, as it will be rotating left or right. But it is not chiral [1].

2.2 History of chirality

To understand how chirality has evolved to be defined as it is today, it is interesting to see the evolution of the concept over time. The following section starts with the discovery of chirality and focuses on different aspects that are interesting for the study. This is mainly established thanks to the article "Petite histoire de la chiralité, de Pasteur à la physique d'aujourd'hui" published in August 2024 [16].

2.2.1 From Early Optics to Crystal Observations

The history of chirality is deeply connected to the development of optics and crystallography. It started in 1809 when Etienne-Louis Malus (1775-1812) published an article on a new property of reflected and refracted light: its polarisation [17]. This marked the beginning of more significant discoveries in optics and crystallography.

Building on this, in 1811, François Arago (1786-1853) conducted experiments observing that slices of quartz crystals could rotate the plane of polarisation of polarised light [18]. This phenomenon was termed "**natural optical activity**". A year later, Jean-Baptiste Biot (1774-1862) confirmed Arago's results and uncovered another phenomenon: some quartz rotated the light in one direction, while others rotated it in the opposite direction by the same magnitude [19]. This indicated a structural difference within the quartz itself.
Interestingly, René-Just Haüy (1743-1822), considered the father of modern crystallography, had already noticed that certain quartz crystals exhibited asymmetrical faces breaking the overall symmetry of the crystal ten years prior [20]. He called this effect hemihedry and specifically plagyhedry for the type seen in quartz crystals. However, he thought it was a crystallographic irregularity and did not directly link chirality to crystal structure. His work still formed the foundation for crystallography and later studies on the phenomenon, such as Biot's [21].

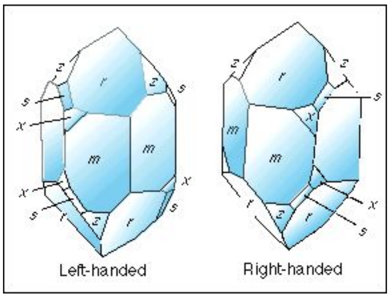

Figure 2.4: Schematic representation of the two irregular forms of quartz crystals observed (Image from Pinterest).

The definite link between the macroscopic crystal shape and the optical properties was established by John Herschel (1792-1871) in 1820. He observed that quartz crystals exhibiting hemihedral facets in one direction were constantly rotating the light in a way. In contrast, those with facets in the opposite direction did the contrary [22]. Once again, the rotation power has the same absolute value but opposite signs. This proved that the optical activity was intrinsically linked to the asymmetrical, non-superimposable mirror-image shapes of the crystals themselves. Therefore, chirality made its scientific debut as a crystallographic property linked to light interaction.

2.2.2 Extension to molecules

Jean Baptiste Biot extended his studies beyond crystals. He showed in 1815 that organic mixtures or vapours also exhibit a rotatory power. This suggested that the property was not exclusive to the solid-state crystalline state [23]. It led him to the conclusion that the origin might be at the molecular level. However, the nature of this molecular asymmetry remained elusive.

The breakthrough connection was established by Louis Pasteur (1822-1895) in 1848. He conducted experiments on tartaric acid salts. Natural tartaric acid was known to be optically active, but a synthetic version called racemic tartaric acid was optically inactive, despite having an identical chemical composition.

Pasteur carefully crystallised a salt of this racemic acid and observed the small crystals under a microscope. He noticed that they were not uniform: some exhibited hemihedral facets orientated in one way, while others had mirror-image facets orientated the opposite way, much like the two forms of quartz described by Haüy and Herschel [24].
Pasteur was able to separate the crystals based on their distinct morphology. Dissolving each one separately in water, he realised that one mixture was optically active in one direction and the other in the other direction. This led him to conclude that racemic tartaric acid is a mixture of two forms of tartaric acid: the dextrorotatory and its mirror image, the levorotatory. Mixing the two solutions in equal amounts resulted in an optically inactive solution, recreating the racemic acid's property. The mirror-image molecular forms were later called **enantiomers** by Johannes Wislicenus in 1884 [25].
His experiments demonstrated that molecular asymmetry could dictate the macroscopic crystal shape but also interaction with polarised light. This introduced the concept of molecular chirality, extending it beyond solid-state physics into the realm of chemistry.

Figure 2.5: Jean-Baptiste Biot observing with the microscope the studies of Louis Pasteur on crystallography in his laboratory of the Collège de France in 1848. (Drawing of Hermann Vogel [16].)

Pasteur also noted the profound connection between chirality and living things [26]. He speculated that biological processes inherently prefer one enantiomer over another. Just like tartaric acid, which only exists in one form, numerous molecules in biological systems only exist in one enantiomeric form. For example, it is the left-handed (L) one for amino acids, while it is the right-handed (R) one for carbohydrates. This phenomenon is known as *homochirality*. The term was introduced by Kelvin in 1904 [27]. Its origin remains unknown, even though many hypotheses have been formulated [28].

2.2.3 Theoretical foundation

While Pasteur had demonstrated that molecular chirality existed and had macroscopic consequences, a question remained: how does the asymmetry arise at the atomic level? In 1874, Jacobus Henricus Van't Hoff (1852–1911) and Joseph Achille Le Bel (1847–1930) independently provided an answer. They laid the foundations for stereochemistry. It is the branch of chemistry that studies the spatial arrangement of atoms in molecules and their influence on their physical and chemical properties.

Van't Hoff proposed a model using the three-dimensional structure of molecules. He suggested that when a carbon atom is bonded to four different substituents, the resulting structure forms a tetrahedron, lacking mirror symmetry. This tetrahedral arrangement creates a **chiral centre**. This leads to two non-superimposable mirror-image forms of the molecule, the enantiomers. His model provided the first theoretical explanation for Pasteur's earlier observations on tartaric acid.

At the same time, in France, Le Bel reached similar conclusions [29]. Rather than focusing on the asymmetry of a single carbon atom, Le Bel emphasised the asymmetry of the molecule as a whole. According to him, chirality results from the overall spatial distribution of atoms within the molecule, not just from an individual chiral centre.
Together, Van't Hoff and Le Bel provided the theoretical foundations linking the three-dimensional structure of molecules to their observed properties.

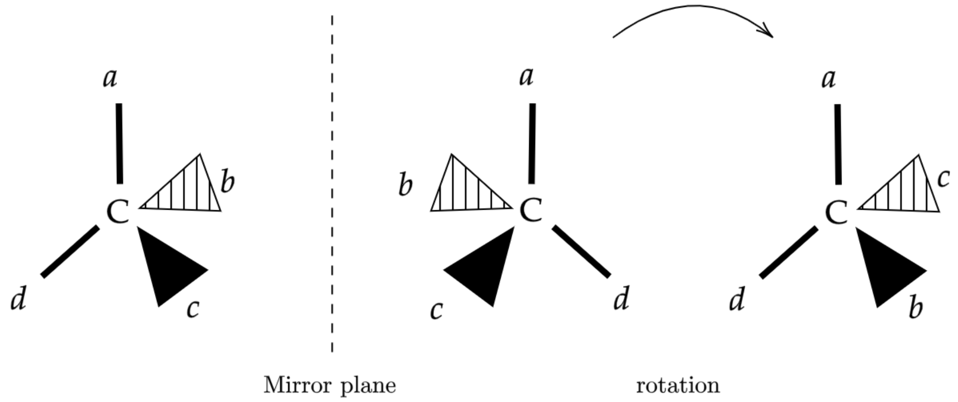

Figure 2.6: Example of a chiral molecule featuring a central carbon. It is bound to four distinct constituents (a, b, c, d). Its mirror image is non-superposable, forming a pair of enantiomers.

2.2.4 Formalisation in physics

The relationship between symmetry and physical properties was further investigated by Pierre Curie. In 1894, he formulated a general principle stating that the symmetry elements of a cause must be found in its effects. Conversely, any asymmetry in an effect must originate from an asymmetry in the cause. Pierre Curie highlighted the important role of symmetry breaking, stating the famous sentence:"*C'est la dissymétrie qui crée le phénomène*" (Dissymmetry creates the phenomenon) [30]. In this context, dissymmetry refers to the lack of improper symmetry elements (which is explained in the section 2.3.2). Curie's principle provided a powerful tool applicable across physics, linking the presence or absence of physical phenomena (like optical activity or piezoelectricity) to the symmetry group of the crystal or molecule.

The concept of **chirality** was formally formulated for the first time in 1894 by Lord Kelvin during a conference at Oxford University Junior Scientific Club [31, 32]. He defined it based on its geometrical nature: "*I call any geometrical figure, or group of points, 'chiral', and say that it has chirality if its image in a plane mirror, ideally realised, cannot be brought to coincide with itself.*". The term *chirality* derives from the word *kheir*, meaning hand in Greek. This definition remains the standard definition, particularly in chemistry, where chirality is omnipresent.

At this stage, enantiomers were primarily distinguished by their opposite interaction with polarised light and potentially different crystal shapes. Therefore, they were considered equivalent unless symmetry played a significant role.
However, the two forms can manifest different behaviours if they interact with another chiral entity. It can be a chiral molecule, a chiral crystal, or a biological system (which is inherently chiral). This phenomenon is called *chiral recognition*. It was observed around 1960 with the drug thalidomide. While one enantiomer was useful to treat pregnancy sickness, the other one was toxic, leading to foetal malformation [33]. This highlighted the importance of chirality in pharmacology and biochemistry,

forming the base of enantioselective analytical chemistry, where the goal is to separate enantiomers.

At this point, chirality seems to be purely a geometric notion. However, while being deeply connected to molecular and crystal structures, it extends beyond geometric objects. It also applies to dynamic physical phenomena, notably to circularly polarised light (CPL). CPL exists in two forms, left-handed (L-CPL) and right-handed (R-CPL), where the electric field vector traces out a helix in space as the wave propagates. Both forms are mirror images of each other.
This led to a more fundamental and physically encompassing definition of chirality proposed by Laurence Barron in 1986 [34]. This will not go into further details, as it is unnecessary in the following discussion.

2.2.5 Conclusion

In conclusion, the scientific story of chirality unfolds from early observations of light interaction with crystals (Malus, Arago, Biot, Haüy, Herschel) to the understanding of its molecular origins and structural basis (Pasteur, van't Hoff, Le Bel). It was then formalised as a fundamental concept based on symmetry by Curie and Kelvin. It had profound implications in chemistry and biology, particularly highlighted by the principle of chiral recognition and the mystery of homochirality. Finally, the concept has been broadened within physics (Barron) to encompass dynamic systems and fundamental symmetries like space inversion and time reversal.
Chirality thus stands as a multidisciplinary concept. It is essential for understanding structure and interaction from the molecular scale to macroscopic materials and even fundamental physical laws. Despite significant progress, key questions remain, notably the origin of biological homochirality and the precise interaction between chirality and various physical fields and forces.

2.3 Chirality and crystallography

In crystallography, classifying materials in terms of their symmetry is essential for various reasons. It allows a better understanding of their physical and chemical properties. That classification relies on structural parameters such as unit cell dimensions and applicable symmetry operations.
This categorisation is briefly reviewed to provide a clear overview. Then, the focus is shifted toward symmetry operations that either preserve or break with chirality, along with the reasons behind that. This will allow a focus on space groups that can exhibit chirality.
Therefore, this section will explore the symmetry constraints that define chiral and achiral space groups.

2.3.1 Reminder

Crystalline materials in three dimensions are categorised into 230 space groups. Those groups are classified based on multiple criteria. Each criterion refines the classification, which leads to groups that include increasingly specific structures. This section is mainly based on the article reviewing crystallographic space groups published in 2010 by Zbigniew Dauter [35].

7 Crystal Systems

Crystalline solids exhibit long-range periodic order. Based on the overall symmetry of their atomic arrangement, they can be categorised into seven fundamental groups known as the **crystal systems**. Each system represents a distinct class of symmetry possible for a periodic structure in three dimensions.
By convention, one chooses a unit cell that reflects the highest possible symmetry of the lattice. The symmetry constraints specific to each crystal system impose conditions on the relationships between the unit cell lattice parameters (a, b, c) and the angles between them (α, β, γ).

The seven crystal systems and the geometric conditions imposed by their respective symmetries are summarised in Figure 2.7.

- **Cubic**
  - $a = b = c$
  - $\alpha = \beta = \gamma = 90°$
  - *Symmetry:* 4 threefold axes
- **Tetragonal**
  - $a = b \neq c$
  - $\alpha = \beta = \gamma = 90°$
  - *Symmetry:* 1 fourfold axis
- **Orthorhombic**
  - $a \neq b \neq c$
  - $\alpha = \beta = \gamma = 90°$
  - *Symmetry:* 3 perpendicular twofold axes or/and mirrors
- **Rhombohedral**
  - $a = b = c$
  - $\alpha = \beta = \gamma \neq 90°$
  - *Symmetry:* 1 threefold axis
- **Hexagonal**
  - $a = b \neq c$
  - $\alpha = \beta = 90°, \gamma = 120°$
  - *Symmetry:* 1 sixfold axis
- **Monoclinic**
  - $a \neq b \neq c$
  - $\alpha = \beta = 90° \neq \gamma$
  - *Symmetry:* 1 twofold axis and/or mirrors
- **Triclinic**
  - $a \neq b \neq c$
  - $\alpha \neq \beta \neq \gamma$
  - *Symmetry:* Only inversion centre possible

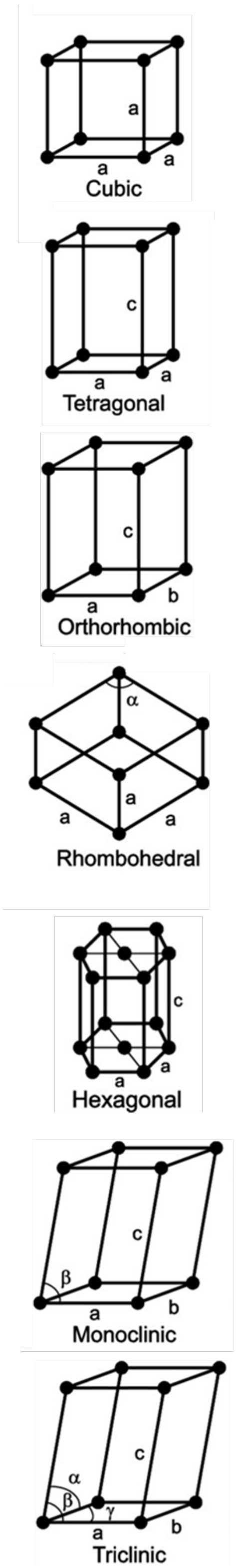

Figure 2.7: Description of the seven different crystalline systems in three dimensions (Images taken from the article [36]).

It is important to clarify the meaning of $\neq$ here. It is understood as "it does not have to be equal".

Therefore, a crystal may have equal angles or cell parameters but be a low-symmetry structure. It will depend on its symmetry. That is why the characteristic symmetry of each system is explicitly mentioned in its description.

14 Bravais lattices

However, crystal systems do not fully describe how atoms are arranged in space. They are based on the unit cell geometry (angles and cell parameters). Another classification is needed to consider the atomic arrangement within the unit cell. *Bravais lattice* are introduced. They describe all possible arrangements to fill space with a periodic pattern. There are four types of placement, defined below. Combining those two features, the 7 crystal systems expand into 14 Bravais lattices. The combination of the latter with the crystal structure results in lattices.

Those centring are necessary as the choice for a unit cell follows a rule. The cell should be the smallest and the simplest, but have the highest possible symmetry. The four unit cell types are presented as follows.

- Primitive configuration, noted **P**: Atoms are located at the corners of the cell. That type is present for every system. There is an exception for the rhombohedral structure. It is denoted **R** to differentiate, as it can be reformulated in a hexagonal structure.
- Body-centred configuration, noted **I**: Atoms are on the corner, and one is located at the centre of the cell. It is present when the system exhibits $\alpha = \beta = \gamma = 90°$.
- Face-centred configuration, noted **F** : Atoms are still present on the corner. Six additional atoms are present on each face. It exists for cubic and orthorhombic systems.
- Base-centred configuration, noted **A**,**B** or **C**. Atoms are still present on the corners. Then, there are two additional ones on opposite faces. Depending on the face, it is called A, B or C.

As seen in Figure 2.8, not all crystal systems combine with the four-centring type. This is because a lot of combinations are equivalent to each other. This reduces the number of necessary lattices to 14.

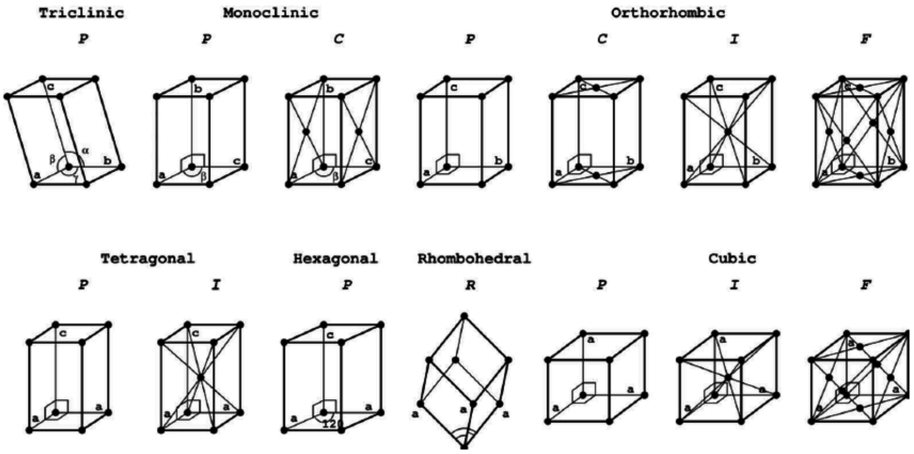

Figure 2.8: Representation of the 14 Bravais lattices in crystallography. (Inspired from [35]).

32 points groups

The seven crystallographic systems can be divided into 32 subgroups. These are called *crystallographic point groups*. They contain the symmetry operations that leave the unit cell invariant with respect to a fixed point.

To fully understand those, it is important to introduce symmetry operations. These operations transform an object but keep the structure in the same state. They can be divided into two main types:

proper and improper rotations. The first simply consists of rotations around an axis, while the latter includes rotoinversions, which combine a rotation and inversion at one point. Translations in space are excluded since they do not leave a fixed point invariant.
The international notation, called Hermann-Mauguin notation, is based on these symmetry elements. It specifies the number of rotations necessary to restore an object to its initial orientation. The different angles of an n-fold rotation are given by:

$$k.\frac{2\pi}{n}, \quad k \in \mathbb{N}$$

For example, a 3-fold rotation means there are three possible angles: $\frac{2\pi}{3}$, $\frac{4\pi}{3}$, and 2π. By convention, rotations follow the anticlockwise direction. The different possible rotations are 1, 2, 3, 4, 6.
Improper rotations are represented by a bar above the number (or sometimes a minus sign before it). In a similar way to proper rotations, the different symmetry elements are denoted $\bar{1}$, $\bar{2}$, $\bar{3}$, $\bar{4}$, $\bar{6}$. They present two particular cases:

- $\bar{1}$ simply corresponds to an inversion, as 1 is the identity.
- $\bar{2}$ corresponds to a reflection, as a rotation of π combined with an inversion has the same effect as a mirror. Therefore, it is often noted m.

Now that the different possible symmetries leaving a fixed point have been introduced, it is necessary to define a point group. It is represented by a maximum of three symbols. Each one corresponds to a specific crystallographic direction. However, the meaning and order of these symbols depend on the crystal system. The resulting groups are detailed in Tab. 2.1, with explanations provided below.

- Cubic systems: The first symbol describes the symmetry along the equivalent directions x, y, and z. The second character is always '3', which is characteristic of a cubic structure. It refers to the four diagonals being threefold axes. The third one is reserved for diagonal mirror planes if necessary.
- Tetragonal, hexagonal, and rhombohedral systems: The first symbol represents the symmetry along the z-axis. The second symbol describes the symmetry along the x and y directions. The third one represents the symmetry along the diagonals of the plane xy. The last two are not always present.
- Orthorhombic systems: Three symbols describe the symmetry along the x, y, and z axes, respectively.
- Monoclinic systems: A single symbol describes the symmetry along the y-axis direction.
- Triclinic systems: A single symbol is used to indicate the presence ($\bar{1}$) or the absence (1) of an inversion centre.
- If an axis has a perpendicular mirror plane, it is denoted by a fraction (e.g., $2/m$).

System	**Internation notation**
Cubic	23, $m\bar{3}$, 432, $\bar{4}3m$, $m\bar{3}m$
Tetragonal	4, $\bar{4}$, $4/m$, 422, $\bar{4}2m$, $4mm$, $4/m\ mm$
Orthorhombic	222, $mm2$, mmm
Rhombohedral	3, $\bar{3}$, 32, $3m$, $\bar{3}m$
Hexagonal	6, $\bar{6}$, $6/m$, 622, $\bar{6}2m$, $6mm$, $6/m\ mm$
Monoclinic	2, m, $2/m$
Triclinic	1, $\bar{1}$

Table 2.1: The 32 different point groups depending on the crystal structure.

230 Space groups

The concept of a *point group* applies to finite objects. However, in periodic crystals, a large number of identical cells are stacked on top of each other in three dimensions. The key principles behind these structures are translation and periodicity.
Therefore, a new concept is brought: *space groups*. It combines point group symmetry with the possible translations of the crystal lattice, defined by the Bravais lattice.
This introduces two additional symmetry operations: screw axes and glide planes.
Screw axes are denoted as n_p. It corresponds to a combination of a rotation of $\frac{2\pi}{n}$ with a translation of p/n along the rotational axis. The different screw axes are 2_1, 3_1, 3_2, 4_1, 4_2, 4_3, 6_1, 6_2, 6_3, 6_4, and 6_5.
A glide plane consists of a mirror plane followed by a translation along a specific direction. The different glide planes are denoted by a, b, c, n, d, and e, and each letter corresponds to a different translation. The choice of the face depends on the mirror plane.

- a, b, c: It corresponds to *axial glide planes*. These describe a translation of $1/2$ in the direction of x, y, or z, respectively. The corresponding translational components are $a/2$, $b/2$, or $c/2$.
- n: It corresponds to *diagonal glide planes*. They describe a translation of $1/2$ along the diagonal of the face. The translational component is $\frac{a+b}{2}$, $\frac{b+c}{2}$ or $\frac{a+c}{2}$.
- d: It corresponds to *diamond glide planes*. They describe a translation of $1/4$ along the diagonal of the face. The translational component is $\frac{a+b}{4}$, $\frac{b+c}{4}$ or $\frac{a+c}{4}$.
- e: It corresponds to *double glide planes*. They describe two axial glide planes. The translational component are $a/2$ and $b/2$, $b/2$ and $c/2$, or $a/2$ and $c/2$.

These additional symmetry elements associated with Bravais lattices expand the 32 point groups into 230 space groups. For a more detailed discussion, one can refer to the article by Zbigniew Dauter (2010) [35], which goes into greater detail. The introduction presented here is sufficient for understanding the following sections.

2.3.2 Symmetry requirements for chirality

As presented in the first section, chirality refers to the absence of mirror symmetry in an object. In crystallography, the concept is closely related: a chiral space group is one that lacks any symmetry operations that map a structure onto its mirror image.
The full set of symmetry operations considered in three dimensions is composed of mirrors, inversion centres, rotations, and translations. By combining these, three additional symmetry operations appear: rotoinversions, glide planes, and screw axes.
It is possible to classify these symmetry elements into two main groups:

- Those that preserve the orientation of the crystal.
- Those that invert the orientation.

This notion is fundamental. By definition, a chiral material cannot be superimposed on its mirror image. Especially if it has a specific handedness, it cannot be switched to the other one.

A pair of a chiral structure and its mirror image is called a set of *enantiomers*. The two structures have the same chemical structure and most physical properties. The only difference is their orientation, resulting in interesting phenomena. Therefore, a chiral material can exist under two enantiomeric forms: a right-handed and a left-handed version.

The goal is to identify the symmetry operations that invert the orientation of a structure and thus break chirality. The most straightforward one is a mirror plane. A simple illustration is provided below in Fig. 2.9. Mirror symmetry transforms an object into its enantiomer, and so, destroys chirality. The second critical symmetry element is the inversion centre. The latter imposes the coexistence of the structure and its enantiomer, leading to an achiral structure, as illustrated below.

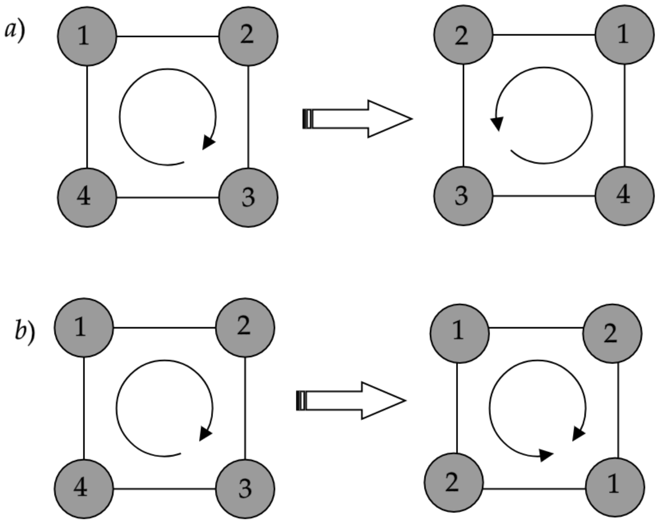

Figure 2.9: a) A square with numbered corners is reflected across a mirror plane positioned at its centre. The resulting image shows that the orientation has been reversed. Therefore, mirrors do not preserve orientation, breaking chirality. b) A square with numbered corners possesses an inversion centre. This forces atoms on opposite corners to be identical. In that configuration, the square possesses both orientations at the same time. However, a chiral structure must have a single handedness. Therefore, chirality is broken.

As a result, improper rotations that contain an inversion centre also break chirality. Since mirror planes and inversion centres are components of improper rotations ($\bar{n}$), it is likewise for glide planes, as they contain mirrors.

The symmetry operations compatible with chirality are those remaining: proper rotations and screw axes. Of the 230 space groups, 165 contain improper symmetry elements, leaving 65 possible space groups. These are known as *Sohncke groups*. These are the groups compatible with chirality.

Among them, twenty-two are *enantiomorphic groups*. These consist of pairs of groups, where each group in a pair describes one enantiomorphic form of a chiral structure. They describe chiral structures that exist in two distinct enantiomorphic forms. Each pair consists of

- a space group containing a screw axis n_p,

- its associated group with the screw axis n_{n-p},

where $p \neq \frac{n}{2}$. This guarantees that a single space group will not possess enantiomers simultaneously. A visual representation is presented in Figure 2.10 below.
To determine which space groups are compatible with chirality, a useful starting point is point groups. Those compatible with chirality are listed. Each space groups is then classed depending on their symmetry, particularly the screw axes. The results are presented in Tab. 2.2.

System	**Compatible point groups**	**Sohncke groups**	
		Non-enantiomorphic space groups	**Enantiomorphic space groups**
Triclinic	1	P1 (1)	
Monoclinic	2	P2 (3), P2$_1$ (4), C2 (5)	
Orthorhombic	222	P222 (16), P222$_1$ (17), P2$_1$2$_1$2 (18), P2$_1$2$_1$2$_1$ (19), C222$_1$ (20), C222 (21), F222 (22), I222 (23), I2$_1$2$_1$2$_1$ (24)	
Tetragonal	4	P4 (75), P4$_2$ (77), I4 (79), I4$_1$ (80)	P4$_1$ (76), P4$_3$ (78)
	422	P422 (89), P42$_1$2 (90), P4$_2$22 (93) P4$_2$2$_1$2 (94), I422 (97), I4$_1$22 (98)	P4$_1$22 (91), P4$_3$22 (95); P4$_1$2$_1$2 (92), P4$_3$2$_1$2 (96)
Rhombohedral	3	P3 (143), R3 (146)	P3$_1$ (144), P3$_2$ (145)
	32	P312 (149), P321 (150), R32 (155)	P3$_1$12 (151), P3$_2$12 (153); P3$_1$21 (152), P3$_2$21 (154)
Hexagonal	6	P6 (168), P6$_3$ (173)	P6$_1$ (169) , P6$_5$ (170); P6$_2$ (171), P6$_4$ (172)
	622	P622 (177), P6$_3$22 (182)	P6$_1$22 (178), P6$_5$22 (179); P6$_2$22 (180), P6$_4$22 (181)
Cubic	23	P23 (195),F23 (196), I23 (197), P2$_1$3 (198), I2$_1$3 (199)	
	432	P432 (207), P4$_2$32 (208), F432 (209), F4$_1$32 (210), I432 (211), I4$_1$32 (214)	P4$_3$32 (212), P4$_1$32 (213),

Table 2.2: Sohncke groups, derived from the chiral point groups compatible with chirality.
Enantiomorphic space groups: A crystal structure belonging to one of these groups is necessarily chiral and possesses a distinct handedness. Its mirror image (enantiomorph) belongs to the other space group in the pair. These groups describe structures analogous to the shoes in Fig. 2.3.
Non-enantiomorphic Sohncke groups: These groups lack improper symmetry operations but are not enantiomorphic. While compatible with chirality, they do not form enantiomorphic pairs. A chiral structure within such a group might not have a handedness (analogous to the potato in Fig. 2.3), and the space group can accommodate both enantiomers simultaneously.

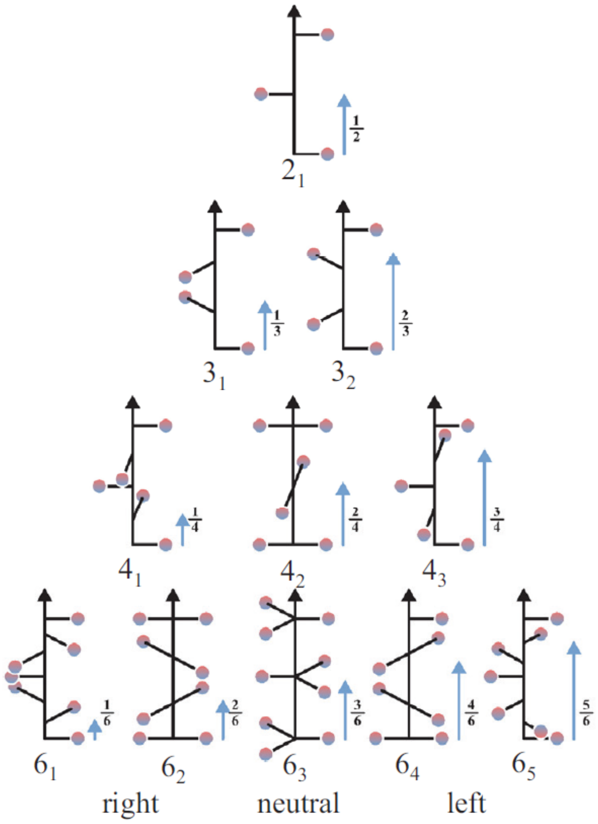

Figure 2.10: Visual representation of screw axes n_p used in chiral space groups. Each diagram illustrates the fractional translation and rotation of atoms along the principal axis. The handedness is determined by the value of p: axes with $p < \frac{n}{2}$ are right-handed, those with $p > \frac{n}{2}$ are left-handed, and $p = \frac{n}{2}$ gives an achiral or "neutral" configuration. This classification forms the basis of enantiomorphic pairs in Sohncke space groups. (Adapted from [1]).

2.4 Measure of Chirality

Quantifying the degree of chirality and determining the handedness (left or right) in crystal solids is a complex challenge. This is due to the periodic nature and potential complexity of these structures. Various approaches have been developed, often based on geometry or molecular chemistry. Each one has its own advantages and limitations when applied to extended solids [4, 1].

2.4.1 Approaches based on geometry

Early methods focused on quantifying chirality based purely on geometric properties, measuring how much a structure deviates from being achiral. Below are presented the most widely used methods to quantify chirality symmetry in extended solids.

Continuous Chirality Measure (CCM)

It evaluates the deviation compared to the closest achiral structure. Defined as a continuous measurement, it allows a measure even for weakly chiral structures. Proposed initially for molecules by Avnir and coworkers [37, 38], the CCM evaluates the "distance" of a given structure P from the set of all achiral structures $\{P_{ach}\}$. It quantifies the minimal amount of distortion needed to transform the chiral object into an achiral one. For a set of N points (e.g., atomic positions in a molecule or motif) such that $P = \{\mathbf{r}_i\}$, the CCM is often defined as:

$$s(P)^2 = \min_{P_{ach} \in Achiral} \left[\frac{1}{N} \sum_{i=1}^{N} |\mathbf{r}_i - \mathbf{r}'_i|^2 \right] \tag{2.1}$$

where $\mathbf{r}'_i$ are the coordinates of the corresponding points in the closest achiral structure P_{ach}. The measure $s(P)$ is then typically normalised to range from 0 (achiral) to 1 or 100 (representing a maximally chiral reference structure).

It provides a continuous value, allowing comparison even for weakly chiral structures. Furthermore, this definition has an intuitive geometric meaning. However, defining and finding the "closest" achiral structure can be computationally challenging, especially for periodic systems. It also does not provide information about the handedness (left vs. right).

Hausdorff distance

Another geometric approach to consider the differences between two sets of points A and B is the Hausdorff distance $d_H(A, B)$. The idea is to measure how dissimilar these two sets of points are by considering the greatest difference from each set's perspective. First, for every point in set A, its closest neighbour in set B is found, and the distance between the two is measured. The largest of these distances, noted $h(A, B)$, describes how far set A extends from set B at its most extreme point. Mathematically, this is expressed as:

$$h(A, B) = \sup_{a \in A} \left(\inf_{b \in B} d(a, b) \right)$$

where $d(a, b)$ is the Euclidean distance between point a and point b. The same thing is realised for every point in the set B. The closest neighbour in the set A is identified, and the largest distance tells how far set B extends from set A at its most extreme point. This distance is denoted $h(B, A)$ and expressed in a similar way to $h(A, B)$.
The Hausdorff distance $d_H(A, B)$ is then simply the larger of these two values:

$$d_H(A, B) = \max\{h(A, B), h(B, A)\} \tag{2.2}$$

In simpler terms, it's the greatest distance you'd have to travel from a point in one set to reach the closest point in the other set, considering all possible starting points. In the context of chirality, it is used to quantify how different a structure A is from its mirror image B [39, 40]. To apply this measure, the two structures need to be optimally superimposed. If, even after this best possible alignment, the Hausdorff distance $d_H(A, B)$ remains greater than zero, it means the structure and its mirror image cannot be perfectly matched. It indicates that the structure is chiral. The amplitude of $d_H(A, B)$ then provides a measure of how chiral the structure is.
This measure is mathematically well-defined and useful for complex shapes where point-to-point correspondence is difficult. Nonetheless, it can be sensitive to single outlier points. In the context of chirality, obtaining the optimal superposition between a structure and its mirror image is necessary but can be computationally demanding. Like CCM, it quantifies the "degree" of chirality but does not provide information about the handedness.

While these geometric methods are conceptually valuable and often effective for simple objects or molecules, they face limitations in determining handedness and so, distinguishing enantiomers (determining handedness). Their application to infinite, periodic structures is also non-trivial and can become complex to apply without relying on specific motifs or finite clusters.

2.4.2 Helicity as a Handedness Measure

While geometric measures quantify the degree of deviation from an achiral structure, they do not give information about the handedness of a structure. To address this need in periodic systems, Gómez-Ortiz et al. [13] recently proposed a method based on the concept of **helicity**. In fluid dynamics, helicity measures the extent to which the flow direction aligns with the direction of rotation (vorticity).

This concept can be adapted to crystals. The "flow" is interpreted as a vector field $\mathbf{v}(\mathbf{r})$ representing atomic displacements from some reference positions. The helicity, $\mathcal{H}$, then measures how spiralling this pattern of atomic displacement is within the crystal's unit cell. It is then defined as the integral over the unit cell volume Ω:

$$\mathcal{H} = \int_{\Omega} d^3r\, \mathbf{v}(\mathbf{r}) \cdot \left[\vec{\nabla} \times \mathbf{v}(\mathbf{r})\right] \tag{2.3}$$

To use this formula, the first step is to define the atomic displacement $\mathbf{u}_k$ for each atom k. These discrete displacements are then used to construct the continuous vector field $\mathbf{v}(\mathbf{r})$ needed for the integral. The atomic displacements are often calculated using computational methods like DFT for static structures or DFPT for vibrations.

$\mathcal{H}$ is non-zero only if the displacement field $\mathbf{v}(\mathbf{r})$ lacks improper symmetries (mirror planes, inversion centres). Therefore, a non-zero $\mathcal{H}$ implies chirality in the displacement pattern. Furthermore, its sign indicates the handedness of the displacement field: positive for right-handed and negative for left-handed, by convention.

This method directly provides information about the handedness. It can quantify the chirality associated with specific structural arrangements. Also, it is designed to apply to periodic crystal systems. However, static structures require a well-defined (and sometimes non-unique) achiral reference.

In summary, this helicity-based approach offers a promising way to quantify handedness in crystals. It connects structural asymmetry to concrete atomic displacement patterns, which are relevant for understanding phase transitions and more. It is illustrated in Figure 2.11 that compares the three measures.

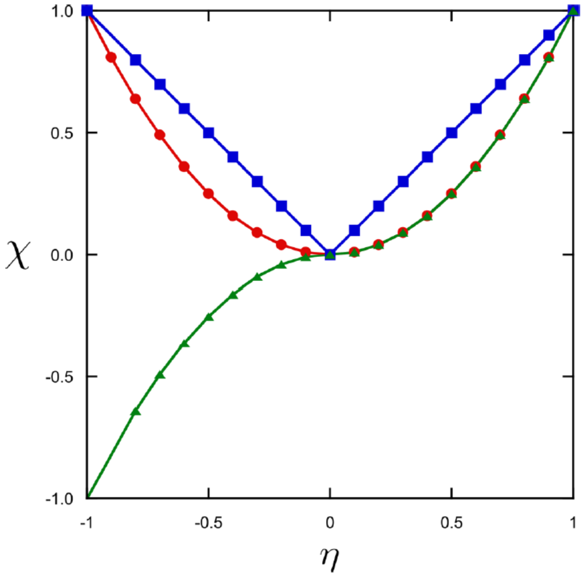

Figure 2.11: Comparison of the evolution of the different chiral measures as a function of the amplitude of the chiral distortion η in a crystal. Positive (negative) values of η correspond to the transition towards the right (left) enantiomorphic phase. Red dots, blue squares, and green triangles respectively correspond to CCM, Hausdorff, and helicity measures. The values of the different measures have been normalised to display a value of 1 at the optimal amplitude of the chiral distortion (η = 1). (Adapted from F. Gòmez-Ortiz [13]).

2.5 Natural optical activity

As seen in the section 2.2, the notions of natural optical activity and chirality are deeply bound, as the former is one of the most direct macroscopic effects of the latter. This section explores the fundamental principles behind this concept. It also provides the challenges associated with its measurement and the symmetry conditions required for its existence.

2.5.1 Physical origin

Linearly polarised light can be described as a superposition of left-circularly polarised (L-CPL) and right-circularly polarised (R-CPL) light of equal amplitude and phase.

In some anisotropic media, the inherent structural handedness causes the material to interact differently with L-CPL and R-CPL. This results in different refractive indices for the two components, n_L and n_R. As the light propagates through the medium over a distance L, this difference in refractive index leads to a phase difference between the L-CPL and R-CPL components. The superposition of the components upon exiting the material results in linearly polarised light whose plane of polarisation has been rotated by an angle ρL compared to the incident light. The rotation angle per unit length, ρ, is given by:

$$\rho(\lambda) = \frac{\pi}{\lambda}(n_L - n_R) \tag{2.4}$$

where λ is the vacuum wavelength of the light. This difference $(n_L - n_R)$ is often referred to as *circular birefringence*. While this difference is typically very small (in the range of 10^{-5} to 10^{-7}), it accumulates over macroscopic distances, leading to measurable rotation angles [41, 42].

Considering visible light ($\lambda \approx 500$ nm) and a difference of $\Delta n \approx 10^{-6}$, it gives a rotatory power with a value around 0.3 degree/mm. For example:

- $\alpha-$Quartz (SiO_2): It exhibits a strong rotation of about 21.7 degrees per millimetre along its optical axis for sodium D-light (λ=589 nm) [42]. This corresponds to a $\Delta n \approx 7 * 10^{-5}$.
- Tellurium (Te): Elemental Tellurium exhibits extremely large optical rotation. In the infrared, it can reach values over 100 degrees per millimetre [43].

Even a rotation of just 1 degree per millimetre (corresponding to $\Delta n \approx 3 * 10^{-6}$) would result in a 10-degree rotation after passing through a 1 cm thick crystal, which is readily detectable with standard polarimeters. The phenomenon is illustrated in Figure 2.12.

The sign of the rotation defines the material's handedness from an optical perspective. Viewed along the beam direction towards the light source, if the sense of rotation of the polarisation is clockwise, the material is described as left-handed (levorotatory) and right-handed (dextrorotatory) if the sense of rotation is anticlockwise.

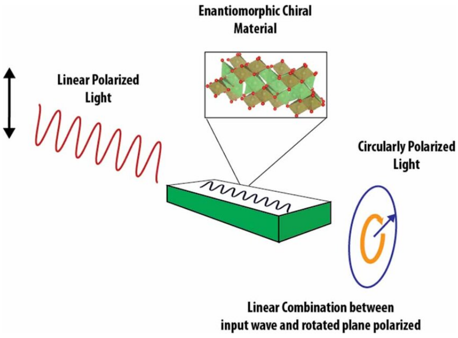

Figure 2.12: Schematic illustration of optical activity. Due to different refractive indices for L-CPL and R-CPL ($n_L \neq n_R$), the plane of polarisation rotates as the light propagates. (Figure adapted from [4]).

Natural optical activity (NOA) is a specific type of optical activity that occurs in the absence of any external field (a magnetic field or mechanical stress). Unlike other forms of polarization rotation, NOA is an intrinsic property: it arises simply from the structural properties of the material (circular birefringence). A main characteristic of NOA is its reciprocal nature, as shown in Figure 2.13.

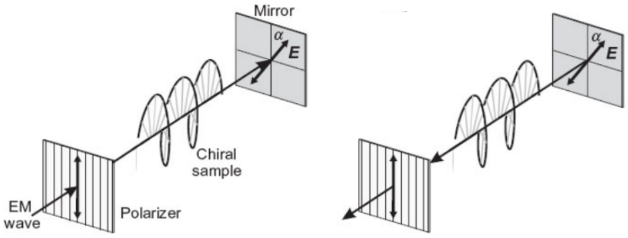

Figure 2.13: Illustration of the reciprocity of natural optical activity. Light passing through a chiral medium (left) experiences a rotation. When the light is reflected and crosses the medium again, the rotation is in the opposite direction. It leads to a net-zero rotation for a round trip through the medium. (Inspired from [44]).

2.5.2 Measurements of NOA

Experimentally observing and quantifying NOA can be challenging. In anisotropic chiral crystals, light propagating in an arbitrary direction will generally experience circular birefringence (NOA) but also linear birefringence. Linear birefringence arises when a material exhibits different refractive indices for light linearly polarised along two orthogonal directions. As a result, if linearly polarised light enters such a crystal, its components along two perpendicular directions travel at different speeds.
Typically, linear birefringence is orders of magnitude larger than circular birefringence. When both are present, the dominant linear birefringence makes it difficult to isolate and accurately measure weaker optical rotation due to NOA.

To overcome this issue, NOA measurements are often performed under specific conditions where linear birefringence disappears by symmetry. It is the case for crystals possessing only one optical axis, called uniaxial crystals. In those crystals, linear birefringence is null when light propagates along the optical axis. Along this specific direction, the refractive indices for all linear polarisations perpendicular to the optical axis are equal. In such a configuration, the observed rotation per unit length ρ is directly related to a specific component of the gyration tensor. This *gyration tensor* g is a second-rank axial tensor that describes how circular birefringence appears in a material [42, 45].

The crystal studied in this thesis (chiral phase of tin(II) fluoride) belongs to the 422 point group. It therefore corresponds to a uniaxial crystal. Its optical axis coincides with the crystallographic c-axis in tetragonal systems, which is assumed to be parallel to the z Cartesian direction. In that case, the gyration tensor has a known form:

$$\mathbf{g}(\omega) = \begin{pmatrix} g_{11}(\omega) & 0 & 0 \\ 0 & g_{11}(\omega) & 0 \\ 0 & 0 & g_{33}(\omega) \end{pmatrix}$$

For light propagating along that particular direction (c-axis) and in the low-frequency limit ($\omega \to 0$), the rotation is often expressed in terms of $\bar{\rho}$:

$$\bar{\rho} = \frac{g_{33}}{2(\hbar c)^2} \tag{2.5}$$

$$\text{such that } \rho(\omega) \simeq (\hbar\omega)^2 \bar{\rho}. \tag{2.6}$$

Being the one measured experimentally, $\bar{\rho}$ is typically reported in units of deg/[mm(eV)^2].
These considerations guide experimental and theoretical strategies for measuring NOA. The focus is put on the components of the gyration tensor relevant for observing NOA along specific high-symmetry directions.
Recent theoretical developments have enabled the computation of NOA from first principles, notably through linear response approaches within DFPT [4, 46]. This is developed in Section 3.3.4.

As NOA is linked to the structural properties of a material, it was long believed it could only arise in chiral structures. However, this is not the case, as discussed in the next subsection.

2.5.3 Symmetry conditions for optical activity

Like chirality, optical activity is deeply restricted by symmetry. However, the two are not equivalent: optical activity can happen in a wider range of crystal classes than chirality.
Chirality requires the absence of improper symmetry operations such as mirror planes, inversion centres, and rotoinversions. Only 11 of the 32 crystallographic point groups meet this criterion; these are the point groups compatible with chirality, as shown in Tab. 2.2.
On the other hand, optical activity is governed by the form of the optical activity tensor. Called *gyration tensor* g, it is a second-rank axial tensor that describes how circular birefringence appears in a material. It will be seen in greater detail in Section 3.3.4. The presence or absence of certain symmetry operations imposes constraints on which components of this tensor may be non-zero.

As shown by Nye and others [42], the necessary condition for optical activity in a crystal is that the symmetry group does not force the optical activity tensor to vanish. This means that some non-chiral point groups including ones with mirrors or rotoinversions still allow non-zero optical activity. A key example is the point group m, which is not chiral as it contains a mirror plane. However, it allows certain components of the optical activity tensor to survive.
There is a total of eighteen optically active crystal classes. Those correspond to crystallographic point groups which are non-centrosymmetric [1]. Therefore, all chiral point groups are optically active, but some non-chiral ones also are. This distinction is summarised in Tab. 2.3.

System	Point group	Chiral	Optical active
Triclinic	1	✓	✓
Monoclinic	2	✓	✓
	m		✓
Orthorhombic	222	✓	✓
	$mm2$		✓
Tetragonal	4, 422	✓	✓
	$\bar{4}$, $\bar{4}2m$		✓
	$4mm$		✓
Rhombohedral	3, 32	✓	✓
	$3m$		✓
Hexagonal	6, 622	✓	✓
	$6mm$		✓
Cubic	23, 432	✓	✓

Table 2.3: Relationship between crystallographic point groups, chirality, and optical activity. Chiral point groups are those that lack improper symmetry operations. Optically active point groups are those that allow non-zero components of the optical activity tensor. Note that some point groups are optically active without being chiral.

---

[1] A point group is said to be *centrosymmetric* if it contains an inversion centre ($\bar{1}$). Otherwise, it is non-centrosymmetric.

The definition taken here for optically active is that the point group must exhibit a non-zero gyration tensor g. However, it is possible to be more restrictive if another criterion is used: observation of optical rotation. In that case, point groups $3m$, $4mm$, and $6mm$ do not fulfil the condition. This leads to 15 optically active classes.
In this work, the criterion used is the one explained earlier: a non-zero gyration tensor g.

Chapter 3

Theoretical and Computational Framework

This work relies on computational simulations performed using the ABINIT software. It is an international and open-source code. ABINIT is based on Density Functional Theory (DFT), a powerful quantum mechanical method widely used to investigate the electronic structure and properties of materials. To understand the results presented later, this section provides a concise overview of the foundations of DFT. It also mentions Density Functional Perturbation Theory(DFPT) as it is used for the study of some physical properties.
The mathematical framework presented in this part is largely inspired by the course "Quantum Modelling of Materials Properties" taught by Prof. Philippe Ghosez at the University of Liège. Some elements are also inspired by the doctoral thesis of Asier Zabalo [47] and the master's thesis of Louis Bastogne [48].

3.1 The Many-Body Problem

Studying material properties requires solving the many-body Schrödinger equation for a system of interacting nuclei and electrons:

$$\hat{H}(\mathbf{r},\mathbf{R})\,\Phi(\mathbf{r},\mathbf{R}) = E\,\Phi(\mathbf{r},\mathbf{R}) \tag{3.1}$$

The full Hamiltonian $\hat{H}(\mathbf{r},\mathbf{R})$ includes kinetic energy terms for both nuclei ($T_i(\mathbf{R})$) and electrons ($T_e(\mathbf{r})$). It also includes potential energy terms for nucleus-nucleus repulsion ($U_{ii}(\mathbf{R})$), electron-electron repulsion ($U_{ee}(\mathbf{r})$), and electron-nucleus attraction ($U_{ie}(\mathbf{r},\mathbf{R})$):

$$\hat{H}(\mathbf{r},\mathbf{R}) = T_i(\mathbf{R}) + U_{ii}(\mathbf{R}) + T_e(\mathbf{r}) + U_{ee}(\mathbf{r}) + U_{ie}(\mathbf{r},\mathbf{R}).$$

The explicit form of each term is expressed by:

$$\begin{aligned}
T_i(\mathbf{R}) &= -\sum_k \frac{\hbar^2}{2M_k}\nabla_k^2, \\
U_{ii}(\mathbf{R}) &= +\sum_{k<k'} \frac{Z_k Z_{k'} e^2}{|\mathbf{R}_k - \mathbf{R}_{k'}|}, \\
T_e(\mathbf{r}) &= -\sum_i \frac{\hbar^2}{2m_e}\nabla_i^2, \\
U_{ee}(\mathbf{r}) &= +\sum_{i<j} \frac{e^2}{|\mathbf{r}_i - \mathbf{r}_j|}, \\
U_{ie}(\mathbf{r},\mathbf{R}) &= -\sum_{i,k} \frac{Z_k e^2}{|\mathbf{r}_i - \mathbf{R}_k|}.
\end{aligned}$$

m_e and M_K respectively correspond to the mass of electrons and nuclei. e is the electron charge, while Z_k represents the atomic number of atom k. Solving this equation directly is computationally complicated for all but the simplest systems due to the large number of coupled degrees of freedom.

A crucial simplification is the *Born-Oppenheimer (BO) Approximation*. Due to the large mass difference between nuclei (M_k) and electrons (m_e), electrons are assumed to adjust to the positions of the much slower nuclei instantaneously. This allows decoupling of the electronic and nuclear motions. It is possible to treat the nuclear positions $\mathbf{R}$ as fixed parameters when solving for the electronic structure. The problem reduces to solving the *electronic Schrödinger equation* for a fixed ionic configuration $\mathbf{R}$:

$$\hat{H}_{el}(\mathbf{r};\mathbf{R})\psi(\mathbf{r};\mathbf{R}) = E_{el}(\mathbf{R})\psi(\mathbf{r};\mathbf{R}),$$

where the *electronic Hamiltonian* is:

$$\hat{H}_{el}(\mathbf{r};\mathbf{R}) = T_e(\mathbf{r}) + U_{ee}(\mathbf{r}) + U_{ie}(\mathbf{r};\mathbf{R}).$$

In that case, the total energy of the electronic system is expressed as:

$$E_{el} = \langle\psi|\hat{H}_{el}|\psi\rangle \quad . \tag{3.2}$$

Here, $\psi(\mathbf{r};\mathbf{R})$ is the electronic wavefunction (depending parametrically on $\mathbf{R}$) and $E_{el}(\mathbf{R})$ is the electronic energy for that specific ionic arrangement. The total energy within the BO approximation is then $E_{tot}(\mathbf{R}) \approx E_{el}(\mathbf{R}) + U_{ii}(\mathbf{R})$, where $U_{ii}(\mathbf{R})$ is the classical nucleus-nucleus repulsion, which is easily calculated. The main challenge remains solving the electronic Schrödinger equation for $E_{el}(\mathbf{R})$ and $\psi(\mathbf{r};\mathbf{R})$. It is complex due to the electron-electron interaction term $U_{ee}(\mathbf{r})$, which couples the coordinates of all electrons.

3.2 Density Functional Theory (DFT)

DFT offers a formally exact reformulation of the many-body problem. It shifts the focus from the complex many-body wavefunction $\psi(\mathbf{r}_1, ..., \mathbf{r}_N)$ to the much simpler electron density $n(\mathbf{r})$. Then, it is possible to obtain the system's energy using an auxiliary system of independent electrons. This section presents the main theorems and notions behind DFT and its adaptation to the physics of condensed matter.

3.2.1 The Hohenberg-Kohn Theorems

The foundation of DFT rests on two theorems proved by Hohenberg and Kohn in 1964 [49]. They are based on the notion of $v_{ext}(\mathbf{r})$, linked to U_{ie}. In this context, it corresponds to the external potential created by fixed nuclei,

$$v_{ext}(\mathbf{r}) = \sum_k \frac{-Z_k e^2}{|\mathbf{r} - \mathbf{R}_k|}. \tag{3.3}$$

1. **First HK Theorem:** The external potential $v_{ext}(\mathbf{r})$ and thus, the Hamiltonian of the system, is exclusively determined by the electron density $n(\mathbf{r})$. The energy of the system can be uniquely determined thanks to a functional of the density. It can be expressed as follows:

$$E[n(\mathbf{r})] = F[n(\mathbf{r})] + \int v_{ext}(\mathbf{r})\, n(\mathbf{r})\, d^3r,$$
$$\text{with } F[n(\mathbf{r})] = T_e[n(\mathbf{r})] + U_{ee}[n(\mathbf{r})]$$

   Since $v_{ext}(\mathbf{r})$ fixes the Hamiltonian $\hat{H}_{el}$, all system properties can be expressed as functionals of $n(\mathbf{r})$, including the many-body wavefunction itself. $F[n]$ is an independent functional, independent of the external potential.

2. **Second HK Theorem:** For any external potential $v_{ext}(\mathbf{r})$, an energy functional $E[n(\mathbf{r})]$ can be defined such that the exact ground-state energy E_0 is the global minimum value of this functional, achieved only when the input density $n(\mathbf{r})$ is the true ground-state density $n_0(\mathbf{r})$. This establishes a variational principle for the density:

$$E_0[n_o(\mathbf{r})] = \min_n\{E[n(\mathbf{r})]\} \tag{3.4}$$

These theorems are profound: they replace the need to find the complex wavefunction ψ with the task of finding the density $n(\mathbf{r})$ that minimises the energy functional $E[n]$. It brings the problem from a $3N$ to 3 dimensions, where N is the number of electrons. This simplifies the matter. However, the exact form of the universal functional $F[n(\mathbf{r})]$ is unknown. While the classical component of the electron-electron interaction $U_{ee}[n(\mathbf{r})]$ is well-defined in terms of density, it is particularly the kinetic energy functional $T_e[n(\mathbf{r})]$ and the non-classical parts of $U_{ee}[n(\mathbf{r})]$ that do not have known exact expressions in terms of $n(\mathbf{r})$.

3.2.2 The Kohn-Sham Approach

The Kohn-Sham formulation provides a practical way to implement DFT [50]. The key idea is to replace the difficult problem of interacting electrons with a problem of fictitious *non-interacting* electrons moving in an effective potential $v_{eff}(\mathbf{r})$. It is designed such that the ground-state density of this system is identical to the ground-state density $n_0(\mathbf{r})$ of the original interacting system.

The non-interacting electrons are described by single-particle wavefunctions, called Kohn-Sham orbitals, $\phi_i(\mathbf{r})$, obtained by solving the self-consistent Kohn-Sham equations:

$$\left(-\frac{\hbar^2}{2m_e}\nabla^2 + v_{\text{eff}}(\mathbf{r})\right)\phi_i(\mathbf{r}) = \epsilon_i\phi_i(\mathbf{r}) \quad \forall i \in \{1, ..., N\}. \tag{3.5}$$

The ground-state electron density is then constructed from these occupied Kohn-Sham orbitals:

$$n(\mathbf{r}) = \sum_{i=1}^{N} |\phi_i(\mathbf{r})|^2. \tag{3.6}$$

The effective potential $v_{\text{eff}}(\mathbf{r})$ is defined as:

$$v_{\text{eff}}(\mathbf{r}) = v_{ext}(\mathbf{r}) + v_H(\mathbf{r}) + v_{xc}(\mathbf{r}). \tag{3.7}$$

It includes:

- $v_{ext}(\mathbf{r})$: The external potential from the nuclei expressed as presented in Eq.(3.3).
- $v_H(\mathbf{r}) = e^2\int\frac{n(\mathbf{r}')}{|\mathbf{r}-\mathbf{r}'|}d^3r'$: The Hartree potential, describing the classical electrostatic repulsion between electrons via the charge density $n(\mathbf{r})$.
- $v_{xc}(\mathbf{r})$: The exchange-correlation potential. This term encapsulates all the complex, many-body quantum mechanical effects (exchange due to the Pauli principle and electron correlation) that were deliberately omitted by considering non-interacting electrons.

The total electronic energy functional in the Kohn-Sham scheme is written as:

$$E_{el}[n] = T_s[n] + E_{ext}[n] + E_H[n] + E_{xc}[n], \tag{3.8}$$

where

- $T_s[n] = \sum_{i=1}^{N}\int\phi_i^*(\mathbf{r})\left(-\frac{\hbar^2}{2m_e}\nabla^2\right)\phi_i(\mathbf{r})d^3r$: kinetic energy of non-interacting KS electrons. It is different from $T_e[n]$, the true kinetic energy of electrons.

- $E_{ext}[n] = \int v_{ext}(\mathbf{r})n(\mathbf{r})d^3r$: potential energy due to external potential,
- $E_H[n] = \frac{e^2}{2}\int\int \frac{n(\mathbf{r})n(\mathbf{r}')}{|\mathbf{r}-\mathbf{r}'|}d^3r\, d^3r'$: Hartree energy describing classical Coulomb energy,
- $E_{xc}[n]$: exchange-correlation energy. It includes the difference between $T_s[n]$ and $T_e[n]$

The crucial point is that the Kohn-Sham approach cleverly isolates all the difficult many-body complexities into the exchange-correlation functional $E_{xc}[n]$. While formally exact, the exact form of $E_{xc}[n]$ is unknown.

3.2.3 Exchange-correlation functional

Therefore, practical DFT calculations rely on *approximations* for $E_{xc}[n]$ [51].
The exchange-correlation energy $E_{xc}[n]$ physically represents the decrease in energy due to the formation of the "exchange-correlation hole" around each electron. A region appears where the probability of finding another electron is reduced due to Pauli exclusion (exchange) and Coulomb repulsion (correlation). The two most widely used approximations are presented below.

Local Density Approximation (LDA)

In this approximation, the electronic density $n(\mathbf{r})$ around a point $\mathbf{r}$ is considered homogeneous. In that case, it is possible to write the exchange-correlation energy term as:

$$E_{xc}^{LDA}[n(\mathbf{r})] = \int n(\mathbf{r})\, \epsilon_{xc}^{LDA}[n(\mathbf{r})]\, d^3r, \tag{3.9}$$

where $\epsilon_{xc}^{LDA}[n(\mathbf{r})]$ corresponds to the exchange and correlation energy per electron of a uniform electron gas with density $n(\mathbf{r})$. It can yield excellent results in certain situations, for example, if $n(\mathbf{r})$ is varying slowly enough. However, it ignores subtle changes in $n(\mathbf{r})$, which may still lead to meaningful consequences.

Generalized Gradient Approximation (GGAs)

To consider those possible fluctuations, another approximation is used. It improves the accuracy of LDA by adding gradient information, $\nabla n(\mathbf{r})$. This allows the consideration of small variations. In that case, the exchange-correlation term is expressed as:

$$E_{xc}^{GGA}[n(\mathbf{r})] = \int n(\mathbf{r})\, \epsilon_{xc}^{GGA}[n(\mathbf{r}), \nabla n(\mathbf{r})]\, d^3r. \tag{3.10}$$

Different GGA functionals have been proposed: their difference lies in the mathematical form of ϵ_{xc}^{GGA}. A widely used example is the Perdew-Burke-Ernzerhof (PBE) functional [52]. It was designed to satisfy several exact constraints without empirical parameters. For the calculations presented in this thesis, the functional employed here is PBE-sol [53]. It represents an appropriate and commonly used choice within the GGA family, as it is the best one for bulk solids in many cases.

3.2.4 Iterative resolution

The Kohn-Sham equations are non-linear because the effective potential $v_{\text{eff}}(\mathbf{r})$ (Eq. 3.7) itself depends on the electron density $n(\mathbf{r})$ and the density is derived from the Kohn-Sham orbitals $\phi_i(\mathbf{r})$ that are solutions to these very equations. This means that the equations need to be solved through an iterative method called Self-Consistent Field (SCF) method. The goal is to find a density $n(\mathbf{r})$ that generates an effective potential $v_{\text{eff}}(\mathbf{r})$. This potential, when used to solve the Kohn-Sham equations, has to yield orbitals that reproduce the same density $n(\mathbf{r})$.

The SCF cycle, illustrated schematically in Figure 3.1, typically proceeds as follows for a fixed atomic configuration. An initial random guess is made for the wavefunction. This allows the calculations for the electronic density $n(\mathbf{r})$. Using that input density, the Hartree potential $v_H(\mathbf{r})$ and the exchange-correlation potential $v_{xc}(\mathbf{r})$ are constructed. Combined with the external potential, this defines the effective potential $v_{eff}(\mathbf{r})$. Kohn-Sham equations are solved to obtain a new set of orbitals ϕ_i and therefore, a new density $n(\mathbf{r})$. This output density is compared with the input one. If the difference is smaller than a predefined tolerance ϵ, self-consistency is reached. The calculations are stopped, and converged properties like total energy, forces on atoms, and stress tensor can be computed. In the opposite case, the input and output densities are mixed to produce a new input density for the next iteration.

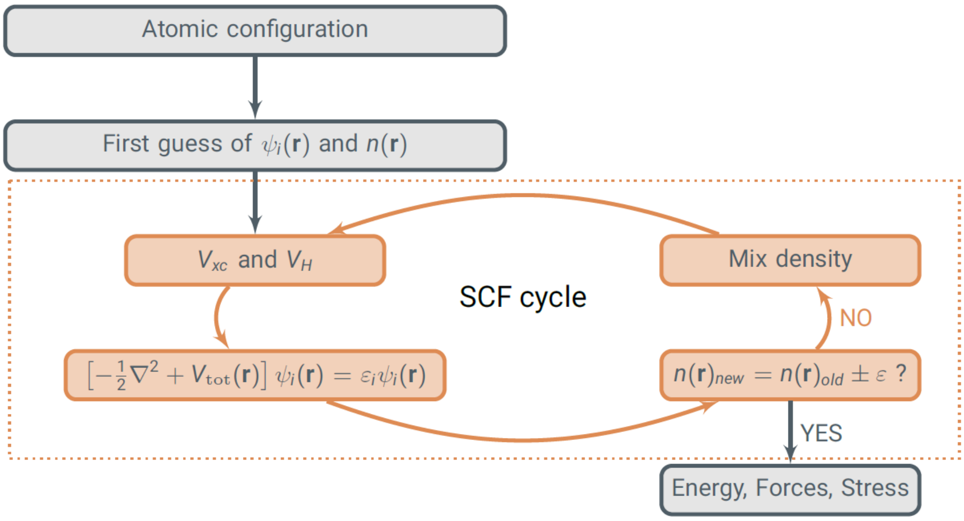

Figure 3.1: Schematic representation of the Self-Consistent Field (SCF) cycle used to solve the Kohn-Sham equations. Starting from an initial guess for orbitals and the electron density, the effective potential is constructed. The Kohn-Sham equations are solved and produce new orbitals and density, and this new density is compared to the input one. If not converged within a tolerance ϵ, the density is mixed, and the cycle repeats until self-consistency is achieved. Physical properties like energy, forces, and stress can be calculated at that point. (Adapted from L. Bastogne [54]).

3.2.5 Periodic solids

The systems considered in this thesis are crystalline solids. They are characterised by a periodic arrangement of identical unit cells in 3D space. To apply DFT effectively to these condensed matter systems, many key concepts related to their periodicity must be incorporated into the Kohn-Sham framework. The first step is to consider periodic boundary conditions: Born-von Karman conditions. They model the crystal as an infinitely repeating structure. This framework allows us to focus on the properties of a single primitive unit cell.

Bloch's Theorem

In a crystalline solid, atoms are arranged periodically. It means that the potential experienced by electrons repeats identically from one cell to another. In such periodic potentials, there exists a theorem that dictates the form of the electronic wavefunctions (Kohn-Sham orbitals in the studied case): Bloch's theorem [55, 56]. The wavefunctions can be written as:

$$\phi_{n,\mathbf{k}}(\mathbf{r}) = u_{n,\mathbf{k}}(\mathbf{r})e^{i\mathbf{k}\cdot\mathbf{r}}, \tag{3.11}$$

where $u_{n,\mathbf{k}}(\mathbf{r})$ is a function that has the same periodicity as the lattice ($u_{n,\mathbf{k}}(\mathbf{r}+\mathbf{R}) = u_{n,\mathbf{k}}(\mathbf{r})$ for any lattice vector $\mathbf{R}$), n is the band index [1] , and $\mathbf{k}$ is a wavevector in the first Brillouin Zone (BZ), which is the primitive cell in reciprocal space. This formulation leads naturally to describing electronic properties in reciprocal space, where one only needs to consider $\mathbf{k}$-points within the BZ. Properties of the crystal are then obtained by integrating over this zone.

Plane-Wave Basis Sets

A common and powerful approach for solving the Kohn-Sham equations in periodic solids is to expand the Bloch wavefunctions using a basis set of plane waves. Since $u_{n,\mathbf{k}}(\mathbf{r})$ is cell-periodic, it can be expanded as a Fourier series involving reciprocal lattice vectors $\mathbf{G}$. It has to satisfy the relations:

$$e^{i\mathbf{G}\cdot\mathbf{r}} = 1 \Leftrightarrow \mathbf{G}\cdot\mathbf{r} = 2\pi n \quad \text{with } n \in \mathbb{N}$$

Consequently, each Bloch function $\phi_{n,\mathbf{k}}(\mathbf{r})$ can be written as:

$$\phi_{n,\mathbf{k}}(\mathbf{r}) = \sum_{\mathbf{G}} C_{n,k}(\mathbf{G}) e^{i(\mathbf{k}+\mathbf{G})\cdot\mathbf{r}} \tag{3.12}$$

where $C_{n,\mathbf{k}}(\mathbf{G})$ are the expansion coefficients. In practice, only plane waves below a given kinetic energy (the cut-off energy E_{cut}) are included:

$$\frac{\hbar^2}{2m_e}|\mathbf{k}+\mathbf{G}|^2 < E_{cut}. \tag{3.13}$$

A higher E_{cut} enhances the precision of the description but also increases the computational cost. This parameter allows the control to find the balance between computational cost and accuracy.

Brillouin Zone Integration

In this context, calculating macroscopic properties (e.g., the total energy or electron density) requires integrating quantities over the first Brillouin zone. Computationally, this continuous integral is approximated by a discrete sum over a finite grid of $\mathbf{k}$-points, known as k-point sampling:

$$\int_{BZ} g(\mathbf{k}) d^3k \simeq \sum_i w_i \, g(\mathbf{k}_i) \tag{3.14}$$

where $\mathbf{k}_i$ are specific points in the BZ and w_i are their associated weights. The density of this k-point mesh is another crucial convergence parameter.

The Pseudo-potential Approximation

In the proximity of nuclei, the potential is very strong. This causes the wavefunctions of core electrons to vary rapidly. Accurately resolving these oscillations would require very high cut-off energies and thus be computationally expensive. However, since core electrons typically do not contribute significantly to chemical and physical properties, they can be "frozen", and only valence electrons are considered. The main idea is to replace the strong ionic potential and the core electrons with an effective potential that acts only on the valence electrons. It is called a pseudo-potential.

This approximation preserves the important scattering properties of the system while significantly reducing the computational cost. For the calculations in this work, optimised norm-conserving Vanderbilt pseudo-potentials (ONCVPSP) [57] were used (version 0.4), which are known for their accuracy and efficiency (available on the website Pseudo Dojo).

---

[1] The band index n labels the different energy bands in the crystal. For each wavevector $\mathbf{k}$ in the Brillouin zone, multiple allowed energy levels (or bands) exist, corresponding to different quantum states. The index n simply distinguishes between them: $n = 1$ for the lowest energy band, $n = 2$ for the next one, and so on.

3.3 Density Functional Perturbation Theory (DFPT)

Density functional theory provides a powerful framework for the calculations of ground-state properties of materials. However, many phenomena are linked to energy derivatives. They necessitate the study of the system's responses to external perturbations around the ground state. To compute those responses efficiently and accurately, DFT is extended to Density Functional Perturbation Theory (DFPT) through a perturbation on the external potential.
In this section, that theory is briefly introduced through a reminder about perturbation theory before diving into DFPT. Then, a few physical properties are presented.

3.3.1 General perturbation theory

The main idea of perturbation theory is to study how the properties of a quantum system change when a small perturbation is applied adiabatically. It begins by considering that the solutions for the unperturbed system are known. In our case, the Hamiltonian of the system and its solutions follow Kohn-Sham equations (Eq. (3.5)). It can be re-expressed as:

$$\hat{H}^{(0)}\phi_i^{(0)} = \epsilon_i^{(0)}\phi_i^{(0)} \quad \forall i \in \{1, ..., N\}$$

with the orthonormalization condition $\langle\phi_i^{(0)}|\phi_j^{(0)}\rangle = \delta_{ij}$. The Hamiltonian $\hat{H}^{(0)}$ is defined as:

$$\hat{H}^{(0)} = -\frac{\hbar^2}{2m_e}\nabla^2 + v_{ext}(\mathbf{r}) + v_H(\mathbf{r}) + v_{xc}(\mathbf{r}). \tag{3.15}$$

Then, a parametric perturbation is added to the external potential $v_{ext}(\mathbf{r})$ through the parameter λ. The latter characterises the perturbation strength. The perturbed Hamiltonian $\hat{H}(\lambda)$ can be written as a power series of that parameter λ. The same thing works for the eigenvalues ϵ_i and the wavefunctions ϕ_i:

$$\begin{aligned} H(\lambda) &= H^{(0)} + \lambda H^{(1)} + \lambda^2 H^{(2)} + \mathcal{O}(\lambda^3), \\ \epsilon_i(\lambda) &= \epsilon_i^{(0)} + \lambda\epsilon_i^{(1)} + \lambda^2\epsilon_i^{(2)} + \mathcal{O}(\lambda^3), \\ \psi_i(\lambda) &= \psi_i^{(0)} + \lambda\psi_i^{(1)} + \lambda^2\psi_i^{(2)} + \mathcal{O}(\lambda^3), \end{aligned}$$

with the notation $X^{(n)} = \frac{1}{n!}\frac{d^nX}{d\lambda^n}\Big|_{\lambda=0}$ $(X = H,\ \epsilon_i,\ \phi_i)$. These expansions are substituted into the Schrödinger equation for the perturbed system, $H(\lambda)|\phi_i(\lambda)\rangle = \epsilon_i(\lambda)|\phi_i(\lambda)\rangle$. Considering terms of the same order in λ, one can derive expressions for the corrections $\epsilon_i^{(n)}$ and $\phi_i^{(n)}$.

An important result is the Hellman-Feynman theorem, which states that the first-order correction to the energy, $\epsilon_i^{(1)}$, can be calculated entirely from the unperturbed wavefunctions $\phi_i^{(0)}$ as the expectation value of the first-order perturbation Hamiltonian $H^{(1)}$:

$$\epsilon_i^{(1)} = \langle\psi_i^{(0)}|H^{(1)}|\psi_i^{(0)}\rangle.$$

However, to calculate higher-order energy corrections, it is necessary to know higher-order corrections to the wavefunctions $\psi_i^{(1)}$. The "$2n+1$ theorem" of perturbation theory states that if the wavefunctions are known up to order n, the corrections to energy can be known up to order $2n+1$. This is particularly powerful, as it often allows accurate calculation of second-order energy derivatives (related to many physical responses) using only first-order wavefunctions. Many ways are possible to obtain those, but they will not be explored in this thesis.

3.3.2 Density Functional Perturbation Theory

Now that the theory behind perturbation theory has been presented, a brief description of DFPT is provided. DFPT applies these perturbation concepts within the Kohn-Sham DFT formalism. The "perturbation" can be any change that modifies the Kohn-Sham Hamiltonian, such as atomic displacements, the application of an electric or magnetic field on the crystal, or a change in cell parameters (strain).

In DFPT, the response of the system to a chosen infinitesimal perturbation is computed. The formalism focuses on how the self-consistent Kohn-Sham quantities (mainly the effective potential $v_{\text{eff}}(\mathbf{r})$ and the electron density $n(\mathbf{r})$) change as a function of this perturbation.
Since the Kohn-Sham equations are solved self-consistently, a perturbation in the external potential $\lambda v_{\text{ext}}^{(1)}$ leads to a direct modification of the Hamiltonian but also affects the Hartree and exchange-correlation potentials via the induced change in the electron density $\lambda n^{(1)}(\mathbf{r})$.
DFPT formalism provides equations to compute these first-order changes in the Kohn-Sham orbitals $\phi_i^{(1)}$, and the density $n^{(1)}(\mathbf{r})$. It is usually done by solving linearised equations such as the Sternheimer equation [58]:

$$(H^{(0)} - \varepsilon_i^{(0)})|\phi_i^{(1)}\rangle = -(H^{(1)} - \varepsilon_i^{(1)})|\phi_i^{(0)}\rangle$$

Once the first-order wavefunction is obtained, a wide range of second-order physical quantities can be derived. This is allowed by the $2n+1$ theorem, also present in DFPT [59]. Here are a few examples of the physical variables derived for the first-order wavefunctions:

Derivative		$\frac{\partial E}{\partial u}$	$\frac{\partial E}{\partial \mathcal{E}}$
1st Derivative		$\mathbf{F}$ (Forces)	$\mathbf{P}$ (Polarisation)
2nd Derivative	$\frac{\partial E}{\partial u}$	IFCs (Phonons)	Z^* (Born charges)
	$\frac{\partial E}{\partial \mathcal{E}}$	Z^*	$\boldsymbol{\epsilon}^{\infty}$ (Dielectric tensor)

Table 3.1: Summary of physical quantities accessible via first and second derivatives of the total energy with respect to atomic displacements $\mathbf{u}$ and homogeneous electric field $\boldsymbol{\mathcal{E}}$.

Those quantities play a central role in this thesis. For instance, forces $\mathbf{F}$ are used to relax atomic positions and identify the equilibrium structure. Phonons provide information on the stability of a structure as explained in Sec. 3.3.3. Furthermore, derivatives up to order 3 will be computed to evaluate natural optical activity, as developed in Sec. 3.3.4.

3.3.3 Atomic displacements and homogeneous electric field

Two of the most common applications of DFPT are the study of lattice dynamics (phonons) and the response to homogeneous electric fields. As they will be mentioned in this work, a brief description is provided.

Phonons correspond to a periodic displacement of atoms from their equilibrium positions. They necessitate the second derivatives of the total energy with respect to these atomic displacements, which define the matrix of interatomic force constants (IFCs),

$$C_{\kappa\alpha,\kappa'\beta}(a,b) = \frac{\partial^2 E_{\text{tot}}}{\partial u_{\kappa\alpha}^a \partial u_{\kappa'\beta}^b},$$

where $u_{\kappa\alpha}^a$ is the atomic displacement of atom κ from its equilibrium position along α direction ($\alpha \in \{x, y, z\}$) in the unit cell a. The Fourier transform of these IFCs gives the dynamical matrix at wavevector $\mathbf{q}$. Diagonalising the dynamical matrix gives the phonon frequencies $\omega_m(\mathbf{q})$ and the corresponding eigenvectors for each phonon mode m [60]. A positive phonon frequency, $\omega_m(\mathbf{q}) > 0$, indicates a stable structure, while an imaginary one indicates some instabilities.

Another important perturbation in periodic solids is the application of a homogeneous electric field $\boldsymbol{\mathcal{E}}$. The total energy's response to these perturbations allows access to some important quantities. The first derivative of the total energy with respect to $\boldsymbol{\mathcal{E}}$ gives the macroscopic electric polarisation $\mathbf{P}$. It characterises how the system electrically responds to the applied field. The electronic dielectric tensor $\boldsymbol{\epsilon}^{\infty}$ is the second-order total energy response due to two electric fields. It describes how the field is screened inside the material. In the low-frequency limit, it can be expressed as:

$$\epsilon_{\alpha\beta}(\omega) = \delta_{\alpha\beta} - \frac{4\pi}{\Omega}\frac{\partial^2 E_{\text{tot}}}{\partial\mathcal{E}_\alpha\partial\mathcal{E}_\beta}, \tag{3.16}$$

where Ω corresponds to the volume of the unit cell, E_{tot} to the total energy, and $\mathcal{E}$ to the electric field. Meanwhile, the mixed second derivatives with respect to atomic displacements $\mathbf{u}$ and electric field $\boldsymbol{\mathcal{E}}$ define the Born effective charge tensor Z^*. It defines a measure of the coupling between atomic motion and macroscopic polarisation. These quantities are central to understanding electromechanical and dielectric properties in solids.

3.3.4 Calculation of NOA tensor

NOA is a phenomenon describing the spatial dispersion of the dielectric response of a material, specifically the first-order correction in the wavevector $\mathbf{q}$ of light to the dielectric tensor ε^{∞} [45].

$$\epsilon_{\alpha\beta}(\omega,\mathbf{q}) \simeq \epsilon_{\alpha\beta}(\omega,\mathbf{q}=\mathbf{0}) + i\sum_{\gamma} q_\gamma \eta_{\alpha\beta\gamma}(\omega), \tag{3.17}$$

where the $\omega \to 0$ limit of the first term on the right-hand side can be computed via Eq. (3.16), and $\eta_{\alpha\beta\alpha}$ is the natural optical activity tensor.

As explained in the section 2.5, NOA manifests through the rotation of the plane of polarisation of light propagating through a medium. In the framework of DFPT, it can be computed as a third-order derivative of the ground-state energy.

The calculation is implemented in ABINIT based on the work of Zabalo and Stengel [46]. It focuses on the static limit, $\omega \to 0$, and on systems respecting time-reversal symmetry. In such cases, the components of the NOA tensor tend towards finite values,

$$\eta_{\alpha\beta\gamma} \equiv \eta_{\alpha\beta\gamma}(\omega \to 0). \tag{3.18}$$

The NOA tensor is related to the first $\mathbf{q}$-derivative of this dielectric tensor. This means the NOA tensor can be equivalently treated as a third derivative of the total energy with respect to two electric field components and one wavevector component representing the spatial variation:

$$\eta_{\alpha\beta\gamma} = \frac{\partial}{\partial q_\gamma}\left(\frac{\partial^2 E_{\text{etot}}}{\partial\mathcal{E}_\alpha^{-\mathbf{q}}\partial\mathcal{E}_\beta^{\mathbf{q}}}\right)\Bigg|_{\mathbf{q}=\mathbf{0}}. \tag{3.19}$$

The exact prefactors and expressions can be found in Ref. [46].

For systems respecting time-reversal symmetry and having a transparent regime, the NOA tensor is antisymmetric. It means that its components are real and satisfy $\eta_{\alpha\beta\gamma}(\omega) = -\eta_{\beta\alpha\gamma}(\omega)$. It makes the tensor possess only 9 independent components in general. Those are directly related to the nine components of the gyration tensor $g_{\alpha\beta}(\omega)$.

As it is equivalent, optical activity is often described by the gyration tensor $g_{\alpha\beta}(\omega)$. It can be constructed from $\eta_{\alpha\beta\gamma}$ using the Levi-Civita symbol ϵ_{ijk} to avoid redundancy:

$$g_{\alpha\beta}(\omega) = \frac{1}{2}\sum_{\gamma,\delta}\epsilon_{\gamma\delta\alpha}\eta_{\gamma\delta\beta}(\omega). \tag{3.20}$$

In this study, as the point group of the chiral phase of SnF_2 is 422, the NOA tensor has the form described in Tabular. 3.2. By symmetry, there are only two independent coefficients.

$\eta_{\alpha\beta\gamma}$		γ		
		1	2	3
$\alpha\beta$	11	.	.	.
	12	.	.	η_{123}
	13	.	η_{132}	.
	21	.	.	$-\eta_{123}$
	22	.	.	.
	23	$-\eta_{132}$	.	.
	31	.	$-\eta_{132}$	.
	32	η_{132}	.	.
	33	.	.	.

Table 3.2: Form of the NOA tensor for a crystal belonging to the 422 point group.

Its components are directly related to the components of the gyration tensor presented in subsection 2.5.2: $\eta_{123} = g_{33}$ and $\eta_{132} = g_{11}$.
Therefore, the results from DFPT calculations will allow the direct obtention of the rotary power $\bar{\rho}$.

Chapter 4

Personal work

Now that the formalism has been introduced, the central question can be explored. The goal is to find if a relation links a measure of chirality to natural optical activity. In order to answer that question, a material is chosen, SnF_2. It is chosen for its rich polymorphism, which includes a chiral phase. This characteristic, along with theoretical considerations, supports the hypothesis of the existence of an achiral higher-symmetry parent phase. That hypothetical phase can be connected to the low-symmetry chiral phase by a displacive phonon-driven soft mode transition. Therefore, it serves as a reference so its properties are studied. The transition is then characterised and studied for the energy, the helicity, and the optical activity.

SnF_2 is selected as the compound of interest as it presents similarities with K_3NiO_2 [4, 12]. The similarities are about the structural phases and will be explored in Section 4.2. This allows the existence of the achiral high-symmetry phase. Furthermore, it presents a lone pair of electrons on Sn^{2+}, which might influence the transition. This hypothesis is therefore explored to investigate the mechanisms leading to the emergence of chiral phases under specific structural conditions.

All calculations presented in this work were performed using the ABINIT software, with the PBE-sol exchange-correlation functional [53] and Optimised Norm-Conserving Vanderbilt (ONCVPSP) pseudo potentials [57]. Values of the energy cut-off (ECUT) and the **k**-point were confirmed after convergence tests presented in Appendix A.

4.1 SnF_2 : Polymorphism

SnF_2 is known for having three crystallographic forms depending on the temperature. They are respectively called $\alpha-$, $\beta-$, and $\gamma-SnF_2$. This section will describe those 3 phases and present the relation between them.

4.1.1 Properties and Utilities

Tin(II) fluoride (SnF_2) is a relatively simple binary compound. Yet, it has attracted significant attention due to its interesting structural behaviour and potential to host chirality-related properties in the solid state.

From a chemical and physical perspective, SnF_2 presents many intriguing characteristics. Firstly, its electronic properties are interesting. It is considered an insulator but can also be viewed as a wide-gap semiconductor. The precise electronic characteristics mainly depend on the tin(II) fluoride polymorphic form (via the temperature) and the presence of defects or impurities. The material is also known for its relatively low melting point (around 210-220°C for the γ-phase) compared to many other inorganic fluorides, which has implications for its processing and stability at elevated temperatures[61].

Thermodynamically, SnF_2 presents a rich phase diagram with several known polymorphs (α, β, and γ-SnF_2). Each one possesses distinct crystal structures and stability ranges. It will be detailed in Section 4.1.3. These phase transitions themselves are a subject of study, often being displacive and linked to subtle changes in atomic coordination and bonding [8]. Also, tin(II) fluoride contains Sn^{2+} cations with an active lone pair of electrons. This lone pair plays a central role in its structural distortions and low-symmetry phases. This will be explored more explicitly in Section 4.4 as an instigator for some phenomena. These features make it an interesting crystal to study symmetry-breaking mechanisms and displacive transitions.

Besides its interesting properties, SnF_2 also has many practical applications. The most famous one is being an ingredient in toothpaste, as it exhibits antibacterial properties. It plays an important role in preventing dental caries and enamel erosion [62]. Others also pointed out its potential applications in the synthesis of other tin-containing compounds (certain types of glass manufacturing and potentially as a component in fluoride-ion batteries or solid electrolytes) [63, 64, 65]. However, these applications of tin(II) fluoride are less widespread than its dental ones.
This dual nature, combining practical utility with fundamental scientific behaviour, makes SnF_2 an ideal case study for investigating the emergence of chirality and its physical consequences in simple inorganic compounds.

4.1.2 Experimental crystallographic structures

As explained, tin (II) exhibits three polymorph forms observed experimentally. They are described here along with some crystallographic information. The experimental data presented here are primarily extracted from the extensive work of G. Denes and collaborators. For comparison and as a starting point for my calculations, theoretical structural data were also retrieved from the Materials Project database [66, 67, 68].

$\alpha-$**SnF**$_2$

The first phase of SnF_2 is called $\alpha-SnF_2$. It is the form observed at ambient temperature. It corresponds to the space group $C2/c$. This means the crystal system is monoclinic: each unit cell parameter might be different, and one of the angles differs from 90°. They are presented in Tab. 4.1. The crystallographic structure is displayed in Fig. 4.1.

	Experiment [9]	**Reference [66]**	**My Calculations**
a (Å)	13.3532(31)	13.09	12.731
b (Å)	4.9073(11)	4.88	4.956
c (Å)	13.7860(33)	13.73	13.852
β (°)	109,467 (18)	108.89	107.628

Table 4.1: Cell parameters of $\alpha-SnF_2$. Experiments are realised at a temperature of 20°C (293.15K). My calculations were performed with $ecut$=45 Ha and $\mathbf{k}-$point grid :$1 \times 6 \times 1$

The primitive unit cell is composed of 24 atoms: 8 tin and 16 fluoride. This form of tin fluoride is achiral as it belongs to the point group $2/m$. It presents a mirror (see Section 2.5.3), breaking the possibility for chirality. Similarly, it is not optically active (see Section 2.5). Being stable at room temperature and pressure, it is the most studied form of SnF_2 in experiments and applications.

$\beta-$**SnF**$_2$

The second phase of SnF_2 is called $\beta-SnF_2$. It belongs to the space group $P2_12_12_1$. This means the crystal system is orthorhombic: each unit cell parameter might be different. They are presented in Tab. 4.2. The crystallographic structure is displayed in Fig. 4.2.

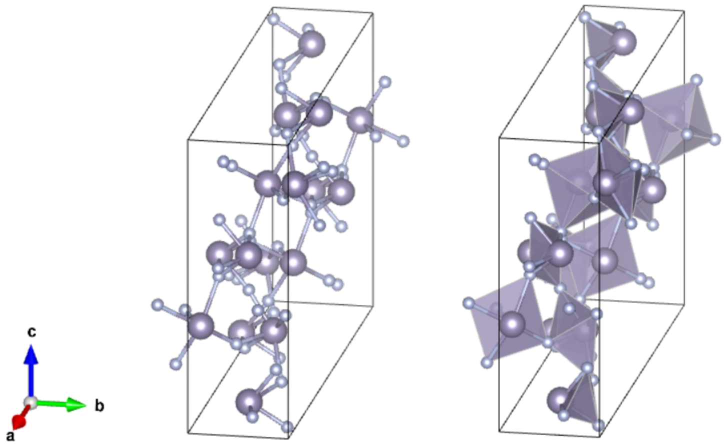

Figure 4.1: Representation of the structure of $\alpha-\mathrm{SnF}_2$ with and without polyhedra. It is a monoclinic structure belonging to the space group $C2/c$. Medium purple spheres represent Sn atoms, while small light purple ones represent F atoms.

	Experiment [7]	**Reference** [67]	**My Calculations**
a (Å)	4.9889(7)	4.90	4.937
b (Å)	5.1392(6)	5.16	5.186
c (Å)	8.4777(14)	8.43	8.191

Table 4.2: Cell parameters of $\beta-\mathrm{SnF}_2$. Experiments obtained $\beta-\mathrm{SnF}_2$ by heating $\alpha-\mathrm{SnF}_2$ at a temperature of 190°C (463.15K) for 1 hour before quenching it to room temperature, 20°C (293K). My calculations were performed with ecut=40 Ha and $\mathbf{k}-$point grid :$4 \times 4 \times 2$.

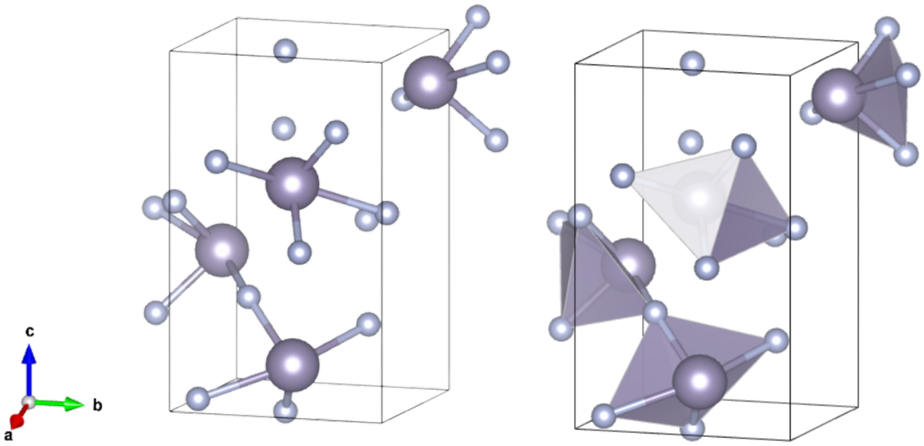

Figure 4.2: Representation of the structure of $\beta-\mathrm{SnF}_2$ with and without polyhedra. It is an orthorhombic structure belonging to the space group $P2_12_12_1$.

The primitive unit cell is composed of 12 atoms: 4 tin and 8 fluoride. Belonging to the point group 222, the form belongs to a non-enantiomorphic Sohncke group chiral (see Section 2.5.3). The structure is chiral, as illustrated with the example of the potato in Figure 2.3. As it is chiral, it is necessarily optically active (see Section 2.5).

$\gamma-$**SnF**$_2$

The third form of SnF$_2$ is called $\gamma-$SnF$_2$. It belongs to the space group $P4_12_12_1$. This means the crystal system is tetragonal: two unit cell parameters are identical, and the last one might be different. The results are presented in Tab. 4.3. The crystallographic structure is displayed in Figure 4.3.

	Experiment [7]	**Reference** [68]	**My Calculations**
a (Å)	5.0733(9)	5.04	5.075
c (Å)	8.4910(33)	8.43	8.188

Table 4.3: Different cell parameters of $\gamma-$SnF$_2$. Experiments were conducted at a temperature of 80°C (353.15K). My calculations were performed with ecut=40 Ha and $\mathbf{k}-$point grid :$4 \times 4 \times 2$.

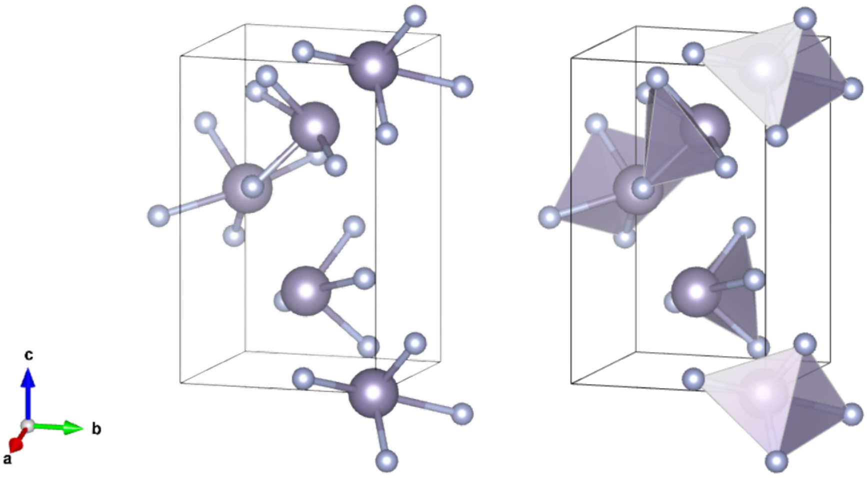

Figure 4.3: Representation of the structure of $\gamma-$SnF$_2$ with and without polyhedra. It is a tetragonal structure belonging to the space group $P4_12_12$. It corresponds to a chiral phase of SnF$_2$. The helicoidal 4_1 is visible, rotating anti-clockwise. It is the right enantiomer (see Section 2.3.2).

The primitive unit cell is composed of 12 atoms: 4 tin and 8 fluoride. Being part of the space group $P4_12_12$. It means that it belongs to an enantiomorphic Sohncke group chiral (see Section 2.5.3). Therefore, the structure is chiral and possesses an enantiomeric form in the associated space group $P4_32_12$. As it is chiral, it is necessarily optically active (see Section 2.5).
Normally, both enantiomers have the same probabilities of being observed in nature. The reason behind the mention of only right $\gamma-$SnF$_2$ might be the similar composition of both forms. Therefore, scientists arbitrarily classified all observations under $\gamma-$SnF$_2$ in space group $P4_12_12$.

4.1.3 Experimental Phase Transition

Since the experimental forms have been described, it is now possible to portray the relationship between them. The descriptions are summarised in Figure 4.5. This part is mainly based on Refs. [8, 10, 69]

It starts from $\alpha-$SnF$_2$ since it is the stable form at room temperature. By heating the crystal to 155°C, it shifts towards $\gamma-$SnF$_2$. If the temperature is still increased, γ-SnF$_2$ continues to be stable up to 213°C. This corresponds to the fusion temperature. If the temperature decreases from liquid SnF$_2$, it needs to reach a lower temperature (185°C) to undergo a transformation towards $\gamma-$SnF$_2$. It will be stable until 110°C. At that point, it becomes metastable down to 66°C, and some crystal shifts back to $\alpha-$SnF$_2$.

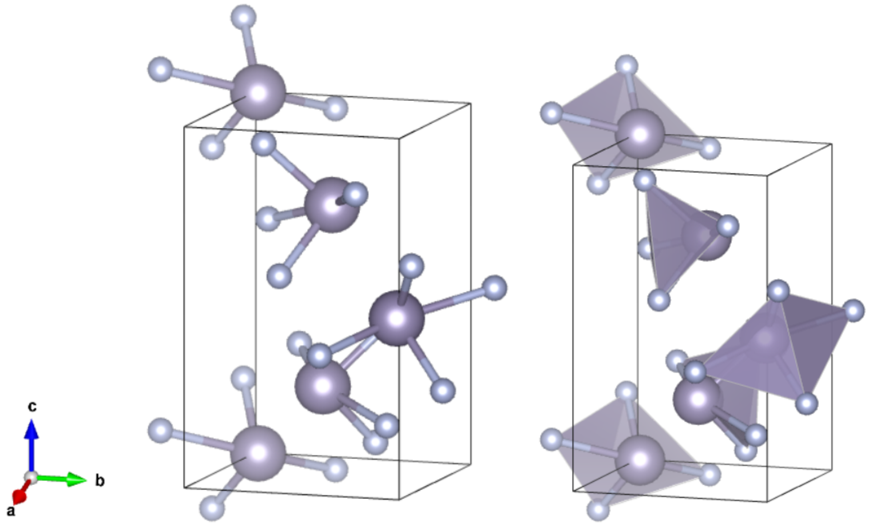

Figure 4.4: Representation of the mirror structure of $\gamma-\mathrm{SnF}_2$ with and without polyhedra. It is a tetragonal structure belonging to the space group $P4_32_12$. The helicoidal 4_3 is visible, rotating clockwise. It is the left enantiomer (see Section 2.3.2).

Around 66°C, reversible transformations between $\beta-$ and $\gamma-$ SnF_2. Below that temperature, $\beta-\mathrm{SnF}_2$ stays metastable while α is stable. Therefore, β is always metastable.

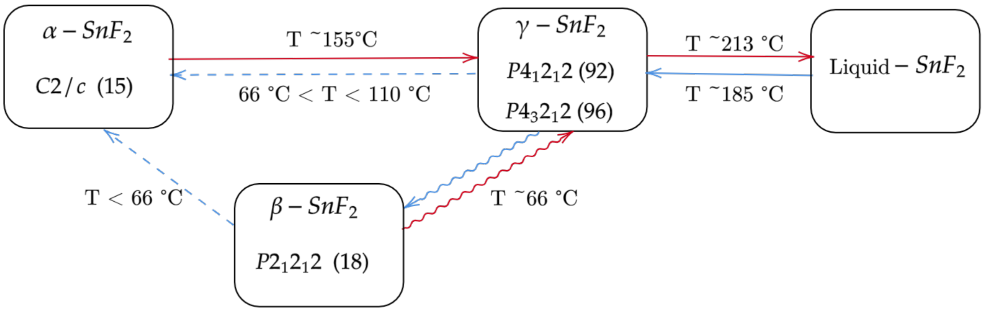

Figure 4.5: Experimental phase transition diagram of SnF_2 [10]. Red arrows correspond to heating the crystal, while blue means cooling it down. Dashed arrows correspond to metastable transitions. Wavy arrows correspond to reversible transitions. It is reproduced based on a similar diagram in [10].

According to Buerger's early classification [70, 71, 72], the $\alpha \rightarrow \gamma$ transition in SnF_2 is considered **reconstructive**. It leads to a break and a reformation of the first-neighbour bonds.

Furthermore, there is no symmetry relation between the two phases. There are large discontinuities between characteristics, energy, and so on. This suggests that this is not a displacive (Landau-type) transition.

The transition between $\beta-$ and $\gamma-$ is smoother, as β is only a deformation of γ. This is supported by the existence of a group-subgroup[1] relation between their space groups: the orthorhombic space group $P2_12_12_1$ of β-SnF_2 is a subgroup of the tetragonal space groups $P4_12_12$ and $P4_32_12$ that describe the enantiomorphic forms of γ-SnF_2. Therefore, there are minimal breaks of symmetry involved,

---

[1] In crystallography, a space group G' is defined as a *subgroup* of another space group G if the symmetry operations of G' are included in those in G. The lattice of G' can be derived from that of G. This relation is often used to describe possible phase transitions, where a high-symmetry phase (G) transforms into a lower-symmetry one (G').

and it does not require the breaking of first-neighbour bonds. This is consistent with a displacive (Landau-type) transition. Their unit cell volumes and energies remain nearly identical, supporting this classification.

4.1.4 Summary

To provide a clear overview of SnF_2, its main crystallographic properties and stability conditions are summarised in Tab.4.4.

Phase	$\alpha-$SnF$_2$	$\beta-$SnF$_2$	$\gamma-$SnF$_2$
Crystal system	Monoclinic	Orthorhombic	Tetragonal
Space group (No.)	$C2/c$ (15)	$P2_12_12$ (18)	$P4_32_12$ (92)/ $P4_32_12$ (96)
Point group	$2/m$	222	422
Chirality	Achiral	Chiral	Chiral
Enantiomorphic pair	/	No	Yes
Optically active	No	Yes	Yes
Stability	Always stable	Always metastable	Stable or metastable
Temperature range	T < 130°C	T<66°C	Stable if 185 °C < T < 213 °C Metastable if 66°C < T < 185°C
Symmetry relation	No symmetry relation with β or γ	Displacive from γ	Parent phase of β

Table 4.4: Summary of key crystallographic properties and stability ranges for the observed polymorphs of SnF_2. Temperature ranges for stability are approximate and based on experimental observations [8, 10]

4.2 Achiral high symmetry phase

As explained in the introduction, a main objective of this work is to observe the evolution of natural optical activity with the emergence of chirality. This is best studied by analysing a phase transition from an achiral phase to a chiral one. However, as explained in the Section 4.1.3, the experimentally observed transition from achiral $\alpha-$SnF$_2$ to the chiral $\gamma-$SnF$_2$ is reconstructive. Such transitions are not described by a regular order parameter related to chirality.

To solve this issue, a methodology recently highlighted in the literature [12] is applied. This involves postulating the existence of an achiral high-symmetry phase. It is considered a parent phase to the chiral phases. They are linked through displacive transitions, driven by unstable phonon modes. This concept of phonon-driven emergence of chirality and algorithmic ways to identify such transitions has been notably developed by Fava et al. [11] and Gómez-Ortiz et al. [12].

In this section, the first part describes why that mechanism is also applicable to SnF_2. Then, the second one presents the achiral phase and its properties.

4.2.1 Justification

To apply this mechanism to SnF_2, the first step is to identify a plausible achiral high-symmetry parent phase. Several criteria guide the choice. It involves, for instance, the crystallographic relationship with lower-symmetry phases of SnF_2. Inspired by previous studies [11, 12] and by the structural chemistry of similar components, a hypothesis is realised: the chiral γ-SnF_2 phase ($P4_12_12$ or $P4_32_12$) comes from a displacive transition driven by phonon instabilities in a rutile-type parent structure. The rutile structure belongs to the achiral space group $P4_2/mnm$ (No. 136), which is a common and relatively simple structure for many AX_2 compounds. Most importantly, $P4_2/mnm$ is a higher-symmetry supergroup of the space groups describing γ-SnF_2. This is a necessary condition for a displacive transition.

In cases where no direct group-subgroup relationship exists, pseudo-symmetry offers a valuable alternative. A distorted phase may closely approximate a higher-symmetry structure. This suggests that small atomic displacements could restore the parent symmetry. As shown by Gómez-Ortiz et al. [12], combining pseudo-symmetry with phonon mode analysis reveals hidden displacive pathways to chirality that standard symmetry analysis might miss.

The hypothesis of a rutile phase for SnF_2 is strongly supported by analogies with other AX_2 materials. A notable case is Tellurium Dioxide (TeO_2). TeO_2 crystallises in the chiral α-TeO_2 phase (paratellurite). It belongs to the space group $P4_12_12$, similarly to γ-SnF_2. While rutile-TeO_2 is not stable under ambient conditions, Peng et al. [73] demonstrated that it can be stabilised via epitaxial growth. This supports that rutile-SnF_2 remains a meaningful high-symmetry reference for theoretical investigations, even if it is not observed as a bulk phase.

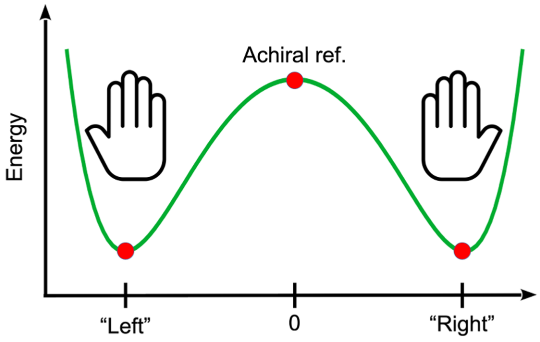

Figure 4.6: Schematic representation of a displacive phase transition from a high-symmetry achiral reference state to two chiral ground states. The x-axis represents the amplitude of a symmetry-breaking distortion, and the y-axis represents the system's energy. The achiral phase is a local maximum, while the chiral phases are energy minima.

The condensation of a specific unstable phonon mode in this hypothetical rutile-SnF_2 phase would break the necessary symmetries to produce the chiral γ-phase. Represented in Figure 4.6, this idea provides the framework for the investigation. The achiral rutile structure is the reference, and the "Left" and "Right" minima correspond to the two enantiomeric forms of the chiral daughter phase.

In the next part, this rutile structure is characterised using first-principles calculations. It focuses on its dynamics to identify the phonon instabilities that could drive the transition to a chiral state.

4.2.2 Characterisation

Now that the justification for considering a rutile-type structure is established, it can be characterised. All calculations are performed with ABINIT, as mentioned in the introduction of the section. The plane-wave energy cut-off has a value of 40 Ha, and the $\mathbf{k}-$point grid used is $6 \times 6 \times 6$.

Equilibrium structure

The relaxed structure of SnF_2 is in the $P4_2/m\,n\,m$ space group. The calculated equilibrium lattice parameters are $a = b =$ 5.472 Å and $c =$ 3.799 Å. The Sn atoms are located at Wyckoff position 2a (0,0,0), and the F atoms at Wyckoff position 4g (0.80621, 0.19379, 0.00000). A representation of this optimised structure is shown in Figure 4.7.

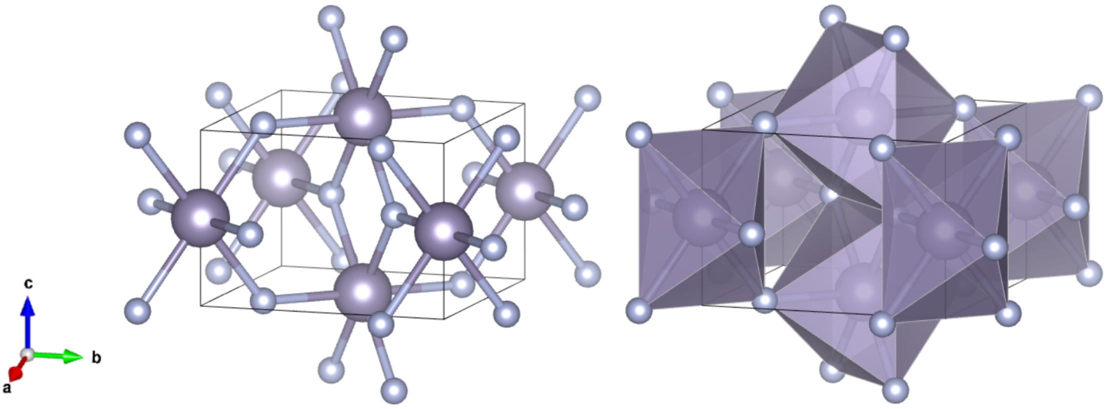

Figure 4.7: Representation of the structure of rutile SnF_2 with and without polyhedra. It is a tetragonal structure in the space group $P4_2/m\,n\,m$.

Electronic band structure

The electronic properties of the rutile structure were investigated through the calculations of the electronic band structure and the density of states (DOS).
The calculations are performed in the reciprocal space. This means high-symmetry points are necessary for the band structure interpolation. Due to the tetragonal symmetry, the directions along x and y are equivalent. The symmetry points used are listed in Tab. 4.5.

K-point	Positions in reciprocal space
Γ	$(0\,,\,0\,,\,0)$
X	$(\frac{1}{2}\,,\,0\,,\,0)\quad(0\,,\,\frac{1}{2}\,,\,0)$
Z	$(0\,,\,0\,,\,\frac{1}{2})$
M	$(\frac{1}{2}\,,\,\frac{1}{2}\,,\,0)$
R	$(\frac{1}{2}\,,\,0\,,\,\frac{1}{2})\quad(0\,,\,\frac{1}{2}\,,\,\frac{1}{2})$
A	$(\frac{1}{2}\,,\,\frac{1}{2}\,,\,\frac{1}{2})$

Table 4.5: **k**-point in the reciprocal space used for the band structure. Since the considered structure is tetragonal, positions in x and y are considered equivalent.

The calculations reveal that rutile-SnF_2 is an insulator. It has a calculated indirect bandgap of 2.513 eV. The Valence Band Maximum (VBM) is located between Γ and Z points, and the Conduction Band Minimum (CBM) at the M point, as observed in Figure 4.8.

From the projected DOS, one observes that the valence band is mainly composed of fluorine $2p$ orbitals, with small contributions from tin $5p$ and $5s$ orbitals. On the other hand, the conduction band is dominated by tin $5s$ orbitals with fluorine $2p$ orbitals. This observation is consistent with the valence electronic configurations of the atoms involved:

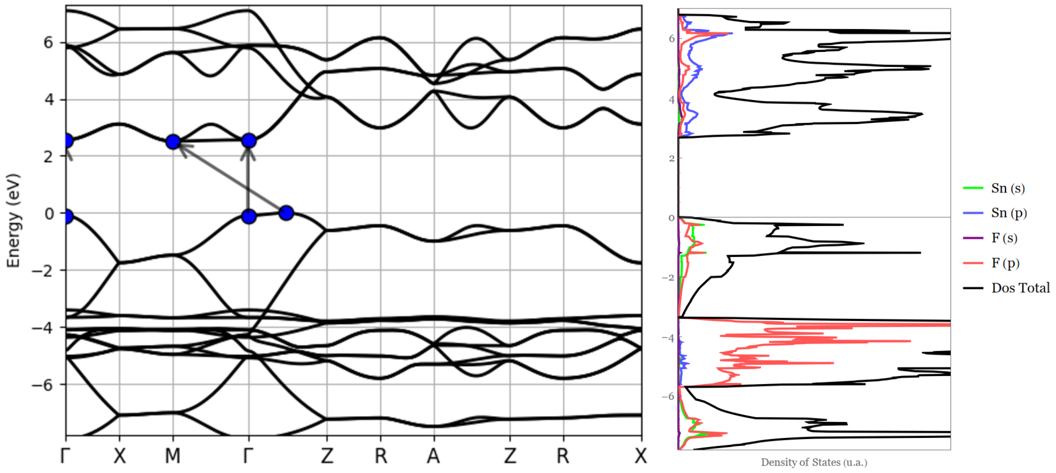

Figure 4.8: Electronic band structure of rutile SnF2, along the path $\Gamma - X - M - \Gamma - Z - R - A - Z - R - X$, associated with the density of states. The figure is shifted to have the Fermi level (the energy of the last occupied band) at zero. It had an initial value of 1.81316 eV. The band gap is indirect as the highest point in the valence band is between Γ and Z, and the lowest point in the conduction band is in M. The bandgap is around 2.513 eV.

- Tin (Sn): $[Kr]\, 4d^{10}\, 5s^2\, 5p^2 \rightarrow$ valence orbitals: $5s^2\, 5p^2$,
- Fluorine (F): $1s^2\, 2s^2\, 2p^5 \rightarrow$ valence orbitals: $2s^2\, 2p^5$.

Their electronegativity needs to be taken into account as well. It has a value of 3.98 for fluorine and 1.96 for tin atoms.
These orbital contributions suggest that the bonding in SnF_2 has a dominant ionic character due to the large electronegativity difference between Sn and F. However, the partial overlap between the fluorine $2p$ and tin $5p$ orbitals also indicates a non-negligible covalent component in the bonds.

Phonon band structure

The next step is to study the dynamical stability of the rutile phase. It is realised by studying the phonon dispersion along the high-symmetry points in the Brillouin zone. This is provided by Figure 4.9.
The phonon spectrum reveals the presence of multiple bands with imaginary frequencies. As a convention, it is plotted as negative values on the y axis. It indicates that this rutile structure is dynamically unstable at 0 K. These imaginary modes correspond to atomic displacement patterns for which the crystal has no restoring forces. Therefore, it will spontaneously distort to lower its energy.
Significant instabilities are observed at every high-symmetry **k**-points. A detailed summary of these unstable modes is presented in Table 4.6. It includes the following information:

- Main label mode: This refers to the symmetry classification of the specific atomic vibration pattern that is most unstable at a particular point in the Brillouin zone. Essentially, it is the notation of the softest (most unstable) way the crystal wants to deform at that specific wavevector.
- Domain: When a crystal structure becomes unstable due to a phonon mode, the atoms move in specific directions (allowed by symmetry). This term describes the particular orientation or combination of these atomic displacements. It provides information about the direction of the distortion of the mode.
  - A single component like (a) indicates a one-dimensional mode, where the distortion is described by a single amplitude displacement along one crystallographic axis.
  - A pair like (a, b) refers to a multidimensional instability, where the distortion is a combination of two mode components with amplitudes a and b.

  - A form like $(a, -a)$ describes symmetry-constrained displacements along two directions with a fixed relationship.

  When a notation contains semicolons (e.g., in (a,b;0,0)), it means that the phonon mode can be decomposed into two independent parts. For example, (0,0) indicates the absence of atomic displacements in one subspace, while (a,b) indicates a deformation in another.

- Space group: This indicates the space group that the crystal would adopt if the atoms were to permanently shift according to the pattern of this particular unstable phonon mode. This process is called "condensation" of the mode. It tells precisely which symmetry elements of the original high-symmetry phase are lost during this distortion.

- ΔE: The total energy difference between the relaxed distorted structure and the high-symmetry rutile phase. A negative ΔE implies that the distorted phase is energetically more favourable.

- SAM (Secondary Amplitude Modes): Additional symmetry-adapted distortion modes that appear as a consequence of the primary unstable mode. These secondary modes are not unstable on their own in the parent high-symmetry phase but become active once the primary mode has broken certain symmetries. Then, they couple to the primary distortion and contribute to the final geometry of the distorted structure.

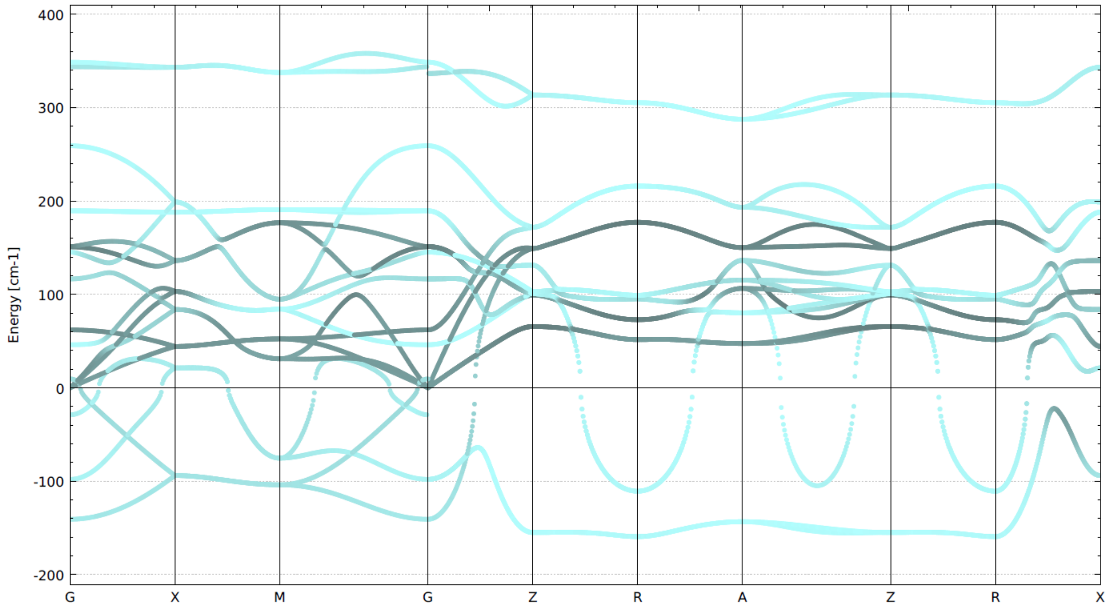

Figure 4.9: Phonon band structure of rutile SnF_2 along the path $\Gamma - X - M - \Gamma - Z - R - A - Z - R - X$. Light blue corresponds to the F atom, while grey corresponds to Sn. Light blue seems much more present; as for the calculations, the system does it from the point of view of the heavier atom (Sn). Many frequencies go below 0, meaning they are imaginary. They correspond to structural instabilities, indicating that this rutile phase is highly unstable.

All relaxations that lead to lower energy phases are represented in an energy diagram in Figure 4.10. Not surprisingly, phases observed experimentally are the lowest in energy.

k−Point	**Eigenfrequencies** (1/cm)	**Main Label Mode**	**Domain**	**Space Group**	ΔE (meV/atom)	**SAM**
Γ: 2	-141	Γ_2^-	(a)	$P\bar{4}_21m$ (113)	-66	Γ_1^+
	-98*	Γ_5^-	(a,b)	$Pmn2_1$ (31)	[UC]	Γ_1^+, Γ_2^+
X: 1	-94*	X_1	$(0,0;a,b)$	Pc (7)	-87	$\Gamma_1^+, \Gamma_2^+, \Gamma_3^+, \Gamma_4^+, \Gamma_5^-$
Z: 1	-154*	Z_4	$(0,a)$	$Cmcm$ (63)	-35	Γ_1^+, Γ_4^+
			(a,a)	$P4_12_12$ (92)	-88	Γ_1^+
			$(a,-a)$	$P4_32_12$ (96)	-88	Γ_1^+
M: 2	-103*	$M_2^- M_3^-$	(a,b)	$Pmmm$ (59)	[UC]	Γ_1^+, Γ_4^+
	-75*	M_5^-	(a,b)	$P2/m$ (10)	[UC]	$\Gamma_1^+, \Gamma_2^+, \Gamma_3^+, \Gamma_4^+$
R: 2	-159*	R_1^+	$(a,b;0,0)$	$P\bar{1}$ (2)	-84	$\Gamma_1^+, \Gamma_2^+, \Gamma_3^+, \Gamma_4^+, \Gamma_5^+$
	-110*	R_1^+	$(a,b;0,0)$	$P\bar{1}$ (2)	-69	$\Gamma_1^+, \Gamma_2^+, \Gamma_3^+, \Gamma_4^+, \Gamma_5^+$
A: 1	-143*	A_4	$(0,a)$	$Imma$ (74)	[UC]	Γ_1^+, Γ_4^+

Table 4.6: Summary of unstable phonon points at high-symmetry **k**−Point for the hypothetical rutile phase of SnF_2. Eigenfrequencies are given in cm^{-1}, * indicates the mode is degenerated two times. ΔE corresponds to the energy difference from the rutile phase to the lower symmetry phase, in $\mathrm{meV/atom}$. A negative ΔE indicates a more stable distorted phase. Entries marked with '[UC]' (unconverged) for ΔE correspond to cases where the structural relaxation did not converge to a state energetically lower than the rutile phase. It possibly indicates a trap in a local energy minimum or the need for a more complex relaxation.

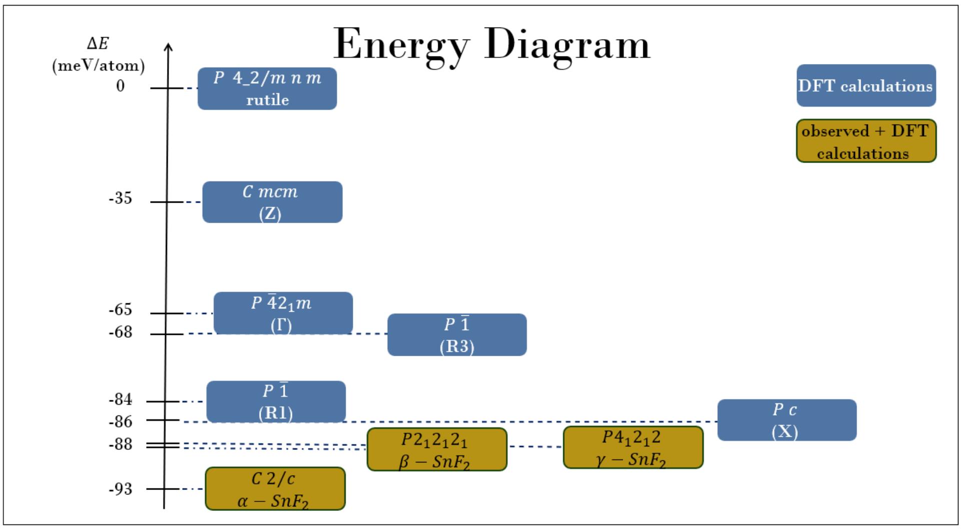

Figure 4.10: Energy diagram of SnF2. It shows the phase observed experimentally, but the one calculated theoretically, thanks to DFT calculations. Not surprisingly, lower phases correspond to the one observed experimentally.

The analysis of the lattice dynamics of the hypothetical rutile phase reveals a landscape rich in structural instabilities. Among these unstable modes, the Z_4 mode at the Z-point of the Brillouin zone stands out. As indicated, the condensation of this Z_4 mode along specific distortion domains (respectively, (a, a) and $(a, -a)$) leads directly to the enantiomorphic chiral space groups $P4_12_12$ and $P4_32_12$. These space groups correspond precisely to those of the experimentally observed chiral γ-SnF_2 phase.

Furthermore, the calculated energy difference ΔE associated with these distortions is the most significant among all calculated instabilities. It reaches -88 meV/atom. This makes the Z_4 mode the most pertinent phonon instability to investigate a displacive transition from an achiral parent to a chiral state in SnF_2.

Therefore, in the next section, the focus is put on this specific phonon-driven pathway.

4.3 Transition from rutile phase to chiral phases

The characterisation of the hypothetical rutile phase of SnF_2 (in Section 4.2.2) has revealed a crucial element. This achiral phase is dynamically unstable, showing many soft phonon modes. Among those, the Z_4 mode at the Z-point in the Brillouin zone is particularly pertinent. Indeed, the condensation of that mode along a specific domain leads to the enantiomorphic space groups $P4_12_12$ and $P4_32_12$.

However, even if Z_4 is the primary mode driving the system towards chirality, it is not the only distortion involved. As mentioned in Tabular 4.6, there is also a Γ_1^+ mode listed as a secondary amplitude mode associated with the first instability. It corresponds to a lattice relaxation preserving the chiral symmetry. Therefore, the transition studied describes a pathway combining those two distortions.

To investigate this transition in detail, the atomic displacements corresponding to the combination of Z_4 and Γ_1^+ are studied. The amplitude of the collective distortion is varied from 0% (undistorted rutile phase) to 100% (fully relaxed chiral phase). For each amplitude, the system's response is analysed under two different structural constraints: fixed rutile cell parameters and relaxed chiral cell parameters.

By comparing these two constraints, the purpose is to dissociate the effects due to pure atomic displacements versus the whole relaxation. This approach provides a framework for understanding the transition and determining whether chirality can be characterised as an order parameter. The specific details of the transition pathway and the analysis of energy, helicity, and NOA will be presented in the following subsections.

4.3.1 Condensation and structural evolution

As identified and explained before, the Z_4 phonon mode provides a direct displacive route to chiral $\gamma-$SnF$_2$ structure. This part describes the nature of the displacements described by that mode. It then explains how the transition is modelled using that.

Nature of the phonon mode

The Z_4 mode means that the rutile cell needs to be doubled along the z direction, as the instability is at the Z-point $\left(0\ ,\ 0\ ,\ \frac{1}{2}\right)$.
It primarily involves small displacements of tin atoms in the xy plane and no displacement in the z direction. The mode involves rotations of polyhedra around the c-axis. These rotations alternate: polyhedra in the $z = 0$ and $z = 1/2$ planes rotate in opposite directions. This influences more fluorine atoms: they exhibit a greater distortion amplitude. Figure 4.11 illustrates the displacements pattern for (a, a) and $(a, -a)$, resulting in the respectively $P4_12_12$ and $P4_32_12$ phases. These displacements break mirror symmetry in the rutile parent phase, leading to the enantiomorphic space groups.

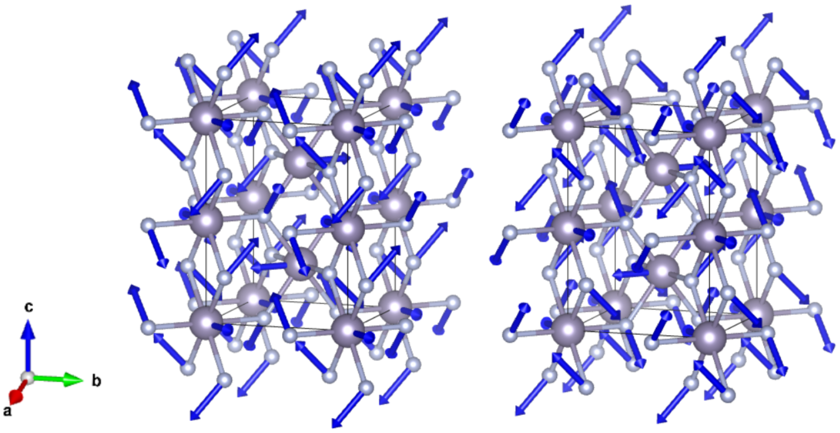

Figure 4.11: Representation of $Z4$ mode. The first one indicates the mode along the $(a, -a)$ direction to go in left $\gamma-$SnF$_2$. The second one represents it along (a, a) to reach right $\gamma-$SnF$_2$. Those are similar; the only difference is the opposite sign along the (x, y) plane.

The Z$_4$ mode in the $P4_2/mnm$ space group is a degenerate mode: its eigenfrequency is degenerate twice, and its irreducible representation is two-dimensional. This means there are two independent basis distortion patterns associated with this instability. The actual distortion of the crystal can be any linear combination of the amplitudes of these two basis distortions. The energy landscape as a function of these two amplitudes dictates the preferred distortion pathways and the resulting lower-symmetry phases.

Figure 4.12 provides a schematic 2D projection of this energy surface for the Z$_4$ mode condensation. The two axes of the plot can be considered as representing the amplitudes of distortion. The central black circle at (0,0) represents the high-symmetry achiral rutile phase ($P4_2/mnm$).

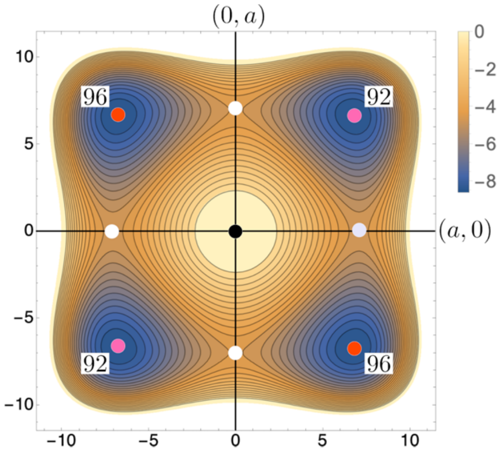

Figure 4.12: Schematic 2D projection of the potential energy surface resulting from the condensation of the two-dimensional Z_4 mode in the rutile parent phase (amplitudes in arbitrary units). The central black circle corresponds to the high-symmetry $P4_2/mnm$ phase. The four white circles indicate saddle points leading to the achiral $Cmcm$ phase. The four deeper energy minima, highlighted with red and pink-filled circles, correspond to the degenerate ground state points of the enantiomorphic chiral phases $P4_32_12$ and $P4_12_12$. (Adapted from [11]).

As illustrated, different directions of distortion lead to different daughter phases. Distortions along the axes of this 2D space lead to four equivalent local energy minima with $Cmcm$ symmetry (white circles in Figure 4.12). This phase is achiral. Distortions along the diagonals with the same amplitude lead to four deeper, degenerate energy minima. These correspond to the two enantiomorphic chiral phases: $P4_12_12$ (pink circles in Figure 4.12) and $P4_32_12$ (red circles in Figure 4.12). Four equivalent ground-state domains exist (two for each enantiomer). This is a direct consequence of the 2D nature of the Z_4 mode and the symmetry of the parent phase. If the amplitudes along the diagonal are different, it leads to the achiral phase $C222_1$.

The presence of these Z_4 mode instabilities and the fact that its condensation along specific domains leads to the lowest energy chiral phases (Figure 4.12 and Table 4.6) makes it the most pertinent instability for investigating a displacive transition to a chiral state in SnF_2.

As explained before, that primary mode is associated with a secondary mode Γ_1^+. Its displacements only affect fluorine atoms, as illustrated in Figure 4.13.

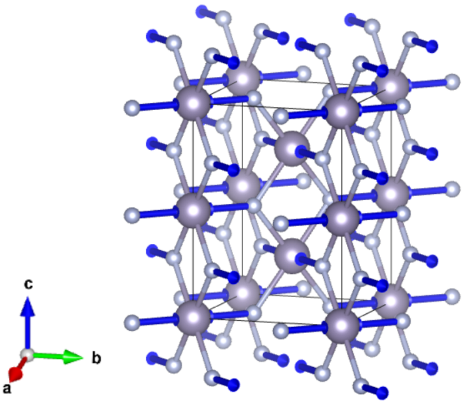

Figure 4.13: Representation of Γ_1^+ mode. The mode is the same for both enantiomers, and it does not change the symmetry of the atoms. Fluorine atoms get closer to tin atoms in the same xy plane.

Model of the transition

To study the evolution of properties during this transition, the amplitude of the distortion is varied from the undistorted rutile to the fully relaxed γ-SnF$_2$. The calculations are performed under two conditions:

1. **Fixed Rutile Cell:** Atomic positions are displaced to be in the chiral space group, but lattice parameters are constrained to those of the optimised rutile parent phase double along the z axis: $a = b = 5.471$ Å, $c = 7.600$ Å.

2. **Fixed Chiral Cell:** Atomic positions are displaced to obtain the fully relaxed rutile structure (100% distortion). The structure has calculated lattice parameters of $a = b = 5.075$ Å and $c = 8.188$ Å. Atoms are then displaced to go from rutile atomic positions to chiral ones gradually.

The difference in cell parameters is quite significant since it corresponds to a decrease of 7.25% in the x and y directions and an increase of 7.74% in the z direction.
This results in a notable difference in the relaxed atomic positions of the chiral phase structures in both cases. The relaxed atomic coordinates are provided in the Appendix B. These two cases allow us to see the difference induced by the lattice parameters difference. The following subsections will present the evolution of energy, helicity, and natural optical activity along this pathway for both constraint conditions.

4.3.2 Energy

The evolution of the total energy during the displacive transition from the rutile parent phase to chiral phases is depicted in Figure 4.14. The x-axis quantifies the amplitude of the distortion. 0% corresponds to the undistorted rutile structure, and 100% represents the atomic positions of the fully relaxed chiral right γ-SnF$_2$ phase (in $P4_12_12$). -100% corresponds to the fully relaxed left enantiomers (in $P4_32_12$). Two scenarios are compared: calculations performed with fixed rutile cell parameters (red curve) and with fixed chiral cell parameters (blue curve).

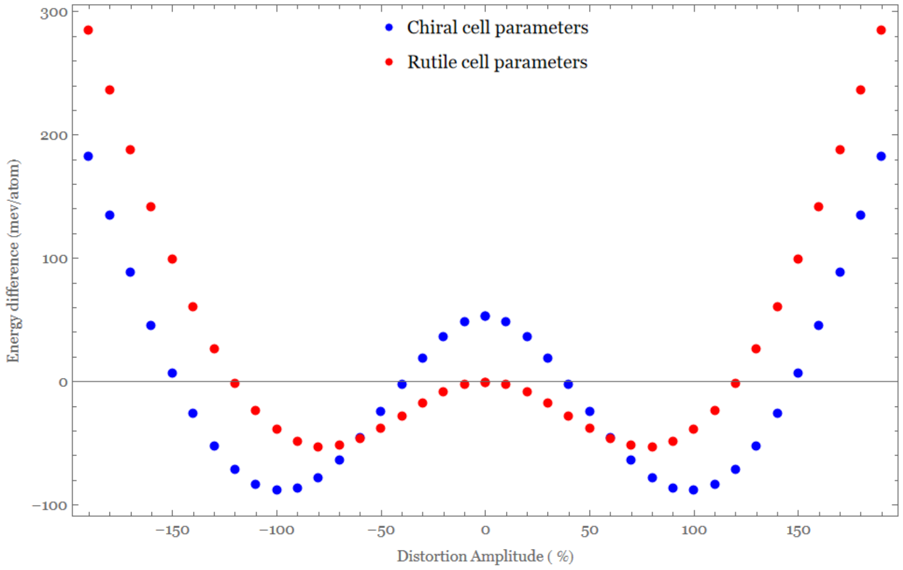

Figure 4.14: The figure corresponds to the energy difference with the rutile phase depending on the distortion amplitude towards chiral phases. 100% and -100% are the relaxed atomic positions of the right and left enantiomers, respectively, for the considered cell parameters. The red plot corresponds to the energy plot with the rutile cell parameters, while the blue plot corresponds to the chiral cell parameters. The energy of the undistorted rutile phase is taken as the zero reference.

By definition, at zero distortion (0%), the rutile phase is the zero energy reference. When a small distortion is introduced with fixed rutile cell parameters (red curve), the energy decreases, showing that the structure is unstable. The minimum of this curve is reached before 100% displacement, with an energy significantly lower than the initial rutile phase, but it does not represent the true ground state.

When the cell parameters are chiral (blue curve), a similar energy profile appears. The undistorted structure is initially higher in energy than the rutile reference by approximately 52.7 meV/atom. This energy difference can be interpreted as the elastic energy stored if the rutile atomic arrangement were forced into the chiral cell's dimensions without allowing any atomic displacements. However, as the distortion is applied, the energy of the system decreases significantly. It forms a characteristic double-well potential. The minima of this potential correspond to the "left" and "right" enantiomeric forms of the γ-SnF$_2$ phase at -100% and +100% displacement, respectively.

This confirms that the chiral distortion, coupled with lattice relaxation, leads to a substantially more stable structure.

The local maximum at 0% displacement on the blue curve now represents the energy barrier for interconversion between the two enantiomers, passing through an achiral transition state. In practice, the barrier is lower than indicate on the graph as the transition will mix both curves. It will start in the rutile structure with the rutile cell parameters ($E = 0$). The energy gain after transforming from rutile to the relaxed chiral phase is consistent with the $\Delta E = -88\mathrm{meV}/atom$ reported in Table 4.6 for the Z$_4$ mode condensation.

4.3.3 Helicity

To quantify the emergence of structural chirality during the transition, the helicity $\mathcal{H}$ was calculated (as defined in Section 2.4). It was evaluated as a function of the atomic displacements. Figure 4.15 presents the evolution of helicity for both fixed rutile cell parameters (red curve) and fixed chiral cell parameters (blue curve).

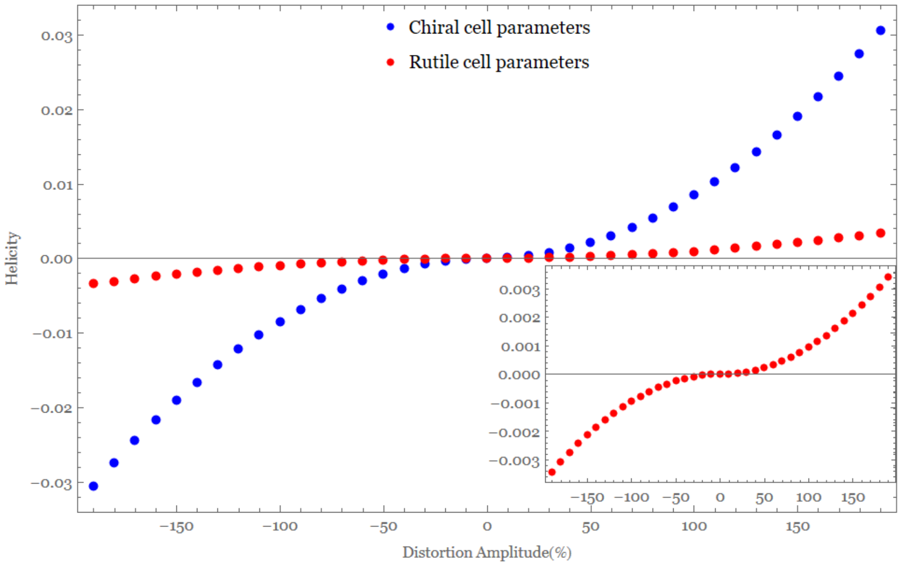

Figure 4.15: Helicity as a function of the distortion amplitude. The red curve corresponds to the calculations with the rutile cell parameters, while the blue one corresponds to the chiral cell parameters. Both curves follow the same tendency but differ in magnitude.

At 0% displacement (rutile phase), the calculated helicity is strictly zero. It confirms the achiral nature of the rutile structure. As the distortion is introduced, a non-zero helicity develops. It indicates the breaking of mirror symmetries and the development of a handed structural arrangement. The sign of the helicity (+ or -) distinguishes between the two enantiomeric distortions. It corresponds to the (a, a) and $(a, -a)$ domains of the Z_4 mode.

A key observation from Figure 4.15 is the significant impact of cell relaxation on the magnitude of the helicity. The blue curve (chiral cell) shows a significant increase in helicity, reaching an absolute value of $\mathcal{H} = 8.48 \cdot 10^{-3}$ at 100% distortion. This value is similar to values obtained for other chiral crystals in literature [12]. The red curve (rutile cell) exhibits helicity values that are approximately ten times smaller (as highlighted by the inset).

This difference illustrates the indirect influence of the cell parameters on helicity. They do not have a direct role, as it is not included in the formula of helicity $\mathcal{H}$ (see Equation (2.3)). However, it influences the relaxed atomic positions of chiral phases. This has an impact on the displacement field $\mathbf{v}(\mathbf{r})$, which has an impact on the helicity $\mathcal{H}$.

As detailed in Appendix B, the cell relaxation is particularly influential on tin atoms. Their displacements are amplified by nearly an order of magnitude in the relaxed chiral cell, while fluorine displacements remain nearly unchanged.

The helicity evolves smoothly with the distortion. It behaves like a continuous order parameter that is zero in the high-symmetry phase and non-zero in the lower-symmetry chiral phase.

The curve follows a quadratic evolution, which is coherent with the formula of the helicity $\mathcal{H}$ (see Equation (2.3)). It depends on the square of the displacement field $\mathbf{v}(\mathbf{r})$. Since the helicity expression is independent of the total energy of the system, it continues to increase with distortion and does not exhibit a maximum at the relaxed structure.

4.3.4 Natural Optical Activity

Having established the emergence of structural chirality, it is time to investigate a direct physical consequence: Natural Optical Activity (NOA). As discussed in Section 2.5.2 and Section 3.3.4, NOA is described using gyration and NOA tensors. For chiral phases belonging to the point group 422 (such as γ-SnF_2), the NOA tensor $\eta_{\alpha\beta\gamma}$ has specific non-zero components (see Table 3.2). All components were calculated, leading to only two non-zero independent coefficients: η_{123} and η_{132}. Figures 4.16 and 4.17 show the evolution of these η tensor components for fixed chiral cell parameters and fixed rutile cell parameters, respectively.

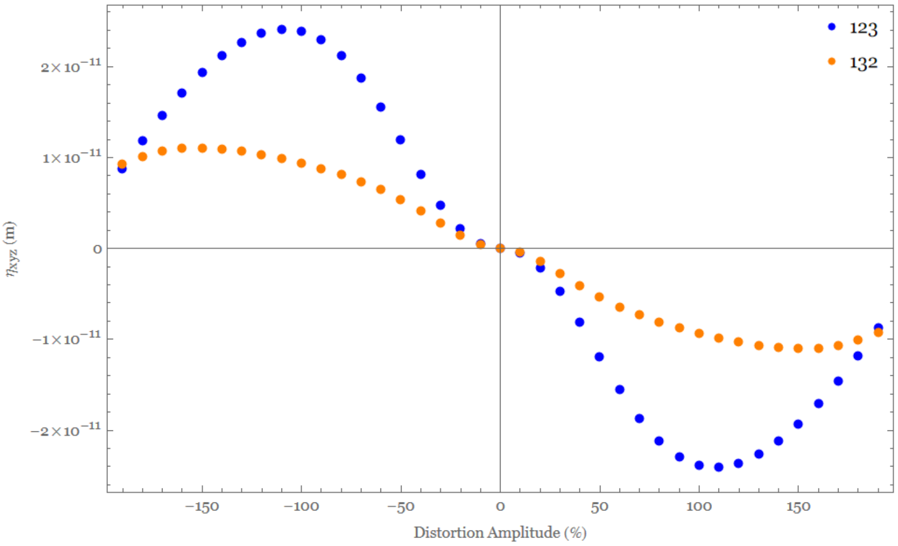

Figure 4.16: Evolution of the two independent coefficients of natural optical activity tensor $\eta_{\alpha\beta\gamma}$ (m) in terms of the distortion amplitude with chiral cell parameters. The right side corresponds to the right enantiomer, and the left side for the left enantiomer. The maximum absolute value seems to be around the relaxed atomic positions corresponding to expectations.

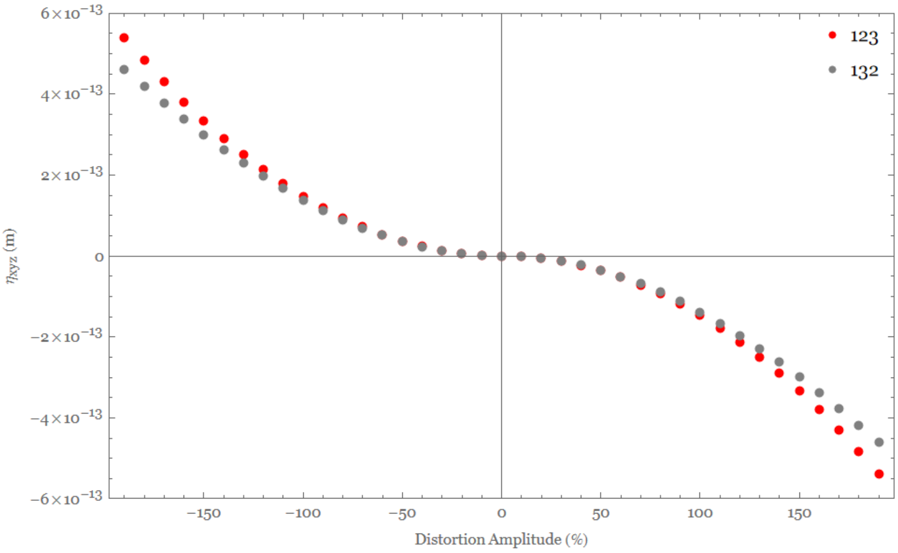

Figure 4.17: Evolution of the two independent coefficients of natural optical activity tensor $\eta_{\alpha\beta\gamma}$ (m) in terms of the distortion amplitude with the rutile cell parameters. The right side corresponds to the right enantiomer, and vice versa for the left side. In this case, components of NOA seem to increase more and more in magnitude.

In both figures, the tensor components are zero for the undistorted structure and develop non-zero values as the chiral distortion is introduced. An observation is the signs of the components being opposite for the two enantiomeric distortion pathways (-100% vs +100%). This reflects the opposite handedness.

Similar to helicity, the magnitudes of the η tensor components are significantly larger when the chiral cell parameters are chosen, compared to the fixed rutile cell case. If the maximal value for η_{123} is compared in both cases, it is around forty to fifty times bigger. It again highlights the importance of lattice relaxation in the strength of chirality-induced properties.

A clear difference is observed in the magnitude of the η tensor components between the two scenarios. When the cell parameters are fixed to those of the target chiral, the η components are significantly larger compared to the case where the cell parameters are constrained to those of the parent rutile phase. For instance, the maximal absolute value of η_{123} is approximately forty to fifty times greater in the first case.
This amplification highlights that adopting cell parameters favouring the chiral structure plays a dominant role. It determines the strength of the NOA response, even without full atomic relaxation at each step. It also suggests that the "geometrical fit" of the atomic arrangement within an appropriate chiral lattice is more critical for large η values than the subtle internal relaxations that might occur if all degrees of freedom were relaxed at each distortion step.
The two figures also exhibit different tendencies with increasing distortion amplitude. For the calculations performed with fixed chiral cell parameters (Figure 4.16), the absolute values of the η components reach a maximum around 90-100% of the full distortion and then notably decrease as the distortion continues. This suggests that there is an optimal structural configuration that maximises NOA. Forcing the atoms to move might lead to internal stresses or slightly less favourable electronic transitions for NOA, causing a diminution in the η components. This behaviour might be attributed to complex non-linear relationships between the precise atomic geometry and the electronic transitions responsible for NOA. It is not simply that higher energy implies lower NOA, but rather that specific structural arrangements maximise the effect.
In contrast, when the calculation is performed with fixed rutile cell parameters (Figure 4.17), the magnitude of the η components appears to increase with the distortion amplitude. It does not show a clear

maximum or decrease within the plotted range. The continuous increase likely results from a progressive symmetry breaking, while the fixed cell prevents the system from fully adapting to its chiral configuration.

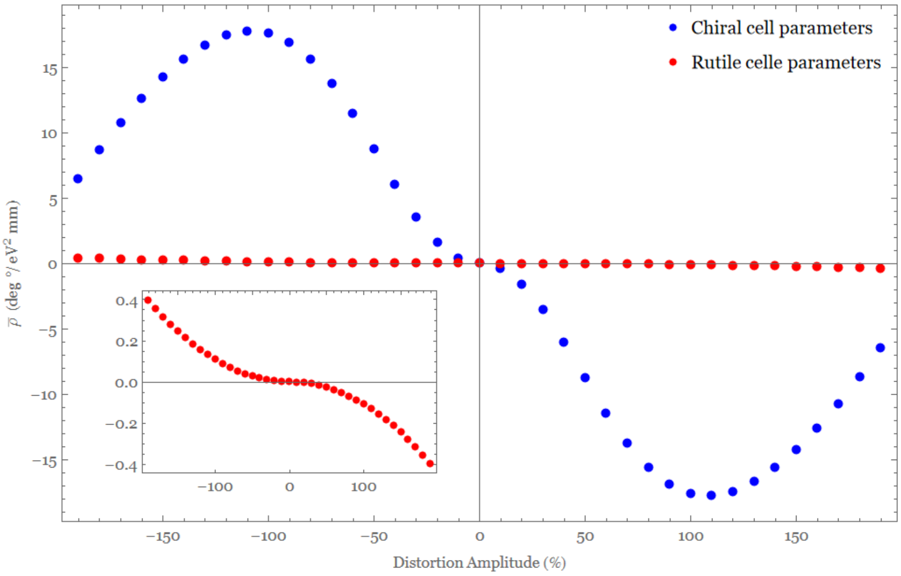

Figure 4.18: Evolution of the rotatory power (deg/[mm(eV)^2]) in terms of the distortion amplitude. The inset provides a zoom on the smaller values obtained with fixed rutile cell parameters.

To relate these tensor components to an observable quantity, a conversion is performed. In the considered case, η_{123} (corresponding to g_{33}) is converted into the macroscopic rotatory power $\bar{\rho}$ using Eq. (2.5). The evolution of $\bar{\rho}$ with atomic displacement is presented in Figure 4.18.

Figure 4.18 clearly demonstrates that the rotatory power grows in magnitude as the chiral distortion is introduced from the achiral rutile phase. The difference in magnitude underscores the critical role of the overall cell geometry. Adopting cell parameters characteristic of the chiral phase is necessary to obtain a significant NOA response.

4.3.5 Relationship between Helicity and NOA

The evolution of structural chirality (quantified by helicity $\mathcal{H}$) and Natural Optical Activity (quantified by the rotatory power$\bar{\rho}$) has been characterised as a function of the Z_4 distortion amplitude. The goal is now to analyse the link between the NOA and the helicity amplitude and to go further in understanding if chirality can be treated as an order parameter. To this end, the calculated rotatory power $\bar{\rho}$ is plotted as a function of the calculated helicity $\mathcal{H}$. The results are presented in Figure 4.19.
Figure 4.19 reveals a certain correlation between the emergent structural chirality and the induced optical activity. For small values of helicity, the rotatory power $\bar{\rho}$ appears to be linearly proportional to the helicity H. This linear relationship, $\bar{\rho} \propto \mathcal{H}$, is observed for both calculations with both fixed chiral and fixed rutile cell parameters.
This linear dependence, $\bar{\rho} \propto \mathcal{H}$, is characteristic of what one would expect if helicity acts as a primary order parameter for the apparition of NOA.

As the distortion (and thus helicity) increases towards the fully relaxed chiral structure, the behaviour for the case with fixed chiral cell parameters (blue curve) becomes more complex. It reaches maxima in absolute value around relaxed chiral structures: $|\bar{\rho}| \approx 17.7$ deg/[mm(eV)^2] at a helicity of $|\mathcal{H}| \approx 0.009$. Beyond this point, the magnitude of $\bar{\rho}$ starts to decrease. This saturation and the following reduction of NOA at large chiral distortions suggest the beginning of non-linear effects. It could also be complex

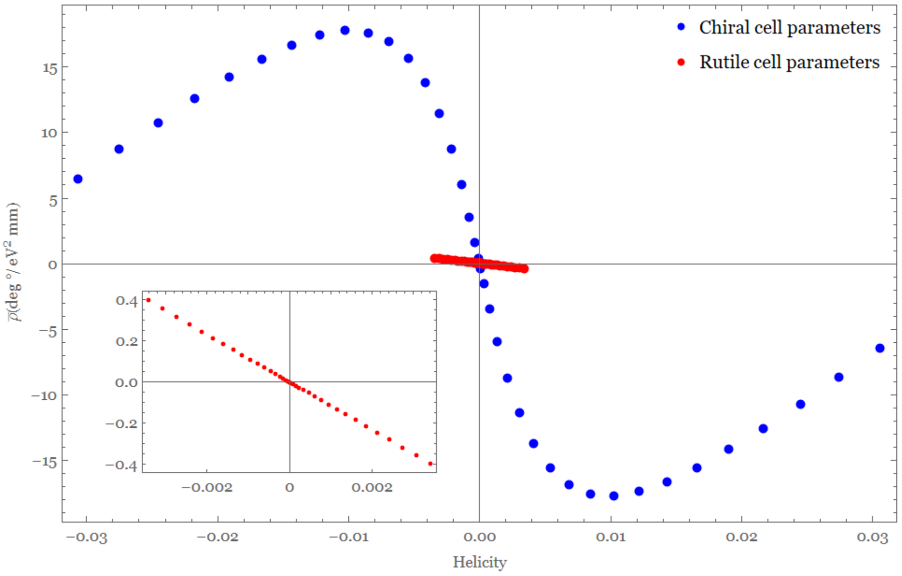

Figure 4.19: Evolution of the rotatory power $\bar{\rho}$ (deg/[mm(eV)^2]) in terms of the structural helicity $\mathcal{H}$. The blue curve corresponds to fixed chiral cell parameters, while red represents fixed rutile cell parameters.

changes in the electronic transitions responsible for optical activity. Those are not captured by a simple linear coupling to the structural distortion.

To further investigate the form of this relationship, Figure 4.20 presents the absolute value of $\bar{\rho}$ as a function of the absolute value of $\mathcal{H}$ on a log-log scale. It is particularly relevant in the regime of small to intermediate helicity.

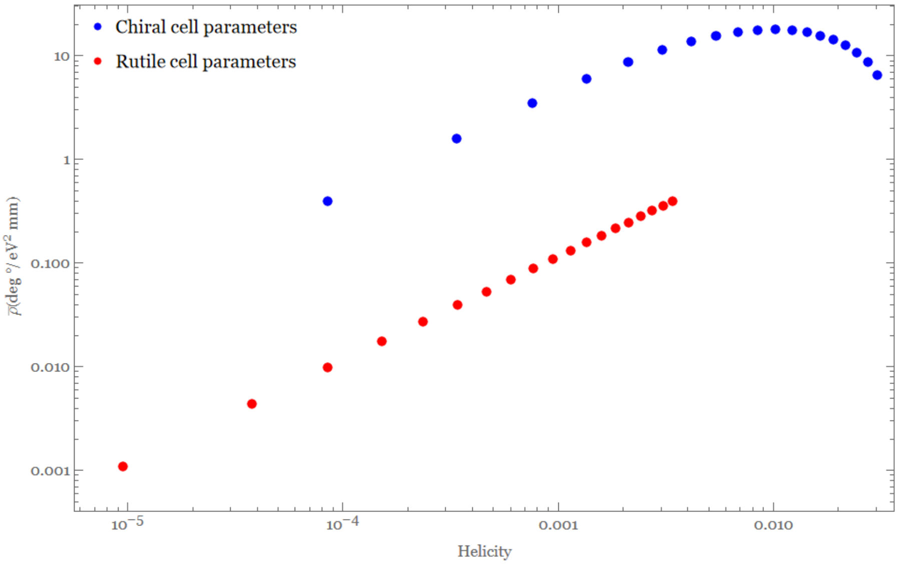

Figure 4.20: Evolution of the absolute value of rotatory power $\bar{\rho}$ (deg/[mm(eV)^2]) in terms of absolute value of the structural helicity $\mathcal{H}$ on a log-log scale.

The log-log plot in Figure 4.20 clearly shows a linear progression for the smallest $|\mathcal{H}|$ values. This suggests a polynomial dependence between the two physical quantities.
For larger values of helicity, the data points deviate from this initial linear trend. It is consistent with the saturation and decrease observed in Figure 4.19. The behaviour after the maxima in Figure 4.19

remains complex to characterise with a simple analytical function.

These results suggest that structural chirality, quantified by helicity, could be considered as a primary order parameter for this chiral displacive phase transition. NOA emerges as a direct physical manifestation linearly coupled to it, at least in the regime of small distortions.
The deviation from linearity at larger distortions highlights the complexity of the relationship between structural changes and optical response in highly distorted chiral systems.

4.4 Driving forces of the structural transition

The previous sections demonstrated that the hypothetical achiral rutile phase of SnF_2 (space group $P4_2/mnm$) is dynamically unstable. It is specifically unstable with a Z_4 phonon mode that opens a displacive pathway to the experimentally observed chiral γ-SnF_2 phase. This finding establishes a plausible mechanism for the spontaneous emergence of chirality in this material.
This raises a question: what intrinsic factors predispose certain materials with a rutile parent structure to undergo such symmetry-breaking distortions leading towards a chiral state, particularly via a Z-point instability?

One likely candidate is the active $5s^2$ lone pair of electrons carried by Sn^{2+} cations in SnF_2. Such lone pairs are well known in chemistry for their tendency to induce anisotropic electron density distributions, often driving structural distortions and lowering symmetry.
Therefore, it is natural to hypothesise that the presence of this lone pair could play a key role in enabling or enhancing phonon instabilities. It could be the case for the Z_4 mode, necessary for the transition from an achiral $P4_2/mnm$ phase to a chiral structure.

To evaluate this hypothesis, a comparative first-principles study is conducted across a range of AX_2 compounds. This investigation examines the correlation between the presence of a cation lone pair and the existence of Z-point phonon instabilities in their high-symmetry parent phase (typically $P4_2/mnm$). It then examines whether such distortions lead to energetically favourable chiral phases. The selected compounds and their electronic configurations are introduced, followed by an examination of the results.

4.4.1 Role of the lone pair

The stereochemically active $5s^2$ lone pair of electrons on the Sn^{2+} cation seems to be a key factor influencing the structural properties of SnF_2. Such lone pairs tend to occupy a significant volume instead of remaining spherical around the cation. This often leads to distortions from high-symmetry environments.
This makes SnF_2 a particularly relevant model system to study symmetry-breaking processes, especially displacive phase transitions. It is specifically interesting for the emergence of chiral crystal structures from higher-symmetry parent phases.

The goal is to investigate the potential role of the lone pair in promoting the specific Z-point phonon instabilities that can lead to chiral phases (such as the Z_4 mode in rutile-SnF_2). To do that, a comparative analysis is performed across several AX_2 compounds. For each compound, the first step is to determine whether the compound has a stereochemically active lone pair on the cation. Then, the phonon dispersion is calculated to check for instabilities at the Z-point of a rutile high-symmetry parent structure.

Compound	**Cations**	**Valence Configuration**	**Lone Pair?**
SnF$_2$	Sn^{2+}	[Kr] 4d^{10} **5s**^{2} 5p^{0}	Yes
SnO$_2$	Sn^{4+}	[Kr] 4d^{10} 5s^{0} 5p^{0}	No
GeF$_2$	Ge^{2+}	[Ar] 3d^{10} **4s**^{2} 4p^{0}	Yes
GeO$_2$	Ge^{4+}	[Ar] 3d^{10} 4s^{0} 4p^{0}	No
PbF$_2$, PbCl$_2$	Pb^{2+}	[Xe] 4f^{14} 5d^{10} **6s**^{2} 6p^{0}	Yes
PbO$_2$	Pb^{4+}	[Xe] 4f^{14} 5d^{10} 6s^{0} 6p^{0}	No
SeO$_2$	Se^{4+}	[Ar] 3d^{10} **4s**^{2} 4p^{0}	Yes
TeO$_2$	Te^{4+}	[Kr] 4d^{10} **5s**^{2} 5p^{0}	Yes

Table 4.7: Valence configurations of the cations in selected AX$_2$ compounds and the presence of a stereochemically active lone pair.

The results of this comparative study are summarised in Table 4.8.

Compound AX$_2$	**Lone Pair ?**	**Instabilities in Z ? (Phonon)**	ω^2 (cm^{-1})	ΔE (eV/atom)
SnF$_2$	Yes	Yes	-154*	-0.088
SnO$_2$	No	No	-	-
GeF$_2$	Yes	Yes	-197*	-437
GeO$_2$	No	No	-	-
PbCl$_2$	Yes	No	-	-
PbF$_2$	Yes	Yes	-51*	-183
PbO$_2$	No	No	-	-
SeO$_2$	Yes	Yes	-382*	-475
TeO$_2$	Yes	Yes	-363*	-0.090

Table 4.8: Comparison of Z-point phonon instabilities in various AX$_2$ compounds with and without active lone pairs on the cation A. ω^2 is the frequency of the most unstable Z-point mode (in cm^{-1}). ΔE is the energy gain (in eV/atom) after relaxing into the chiral structure relative to the high-symmetry rutile parent. * indicates the mode is degenerated two times.

To be complete, Table 4.9 summarised the experimentally observed phases of chosen compounds.

Compound	**Experimentally observed ?**	
AX$_2$	$P4_2/mnm$	$P4_12_12$ $P4_32_12$
SnF$_2$	×	✓
SnO$_2$	✓	×
GeF$_2$	×	×
GeO$_2$	✓	✓
PbCl$_2$	✓	×
PbF$_2$	×	×
PbO$_2$	✓	×
SeO$_2$	×	×
TeO$_2$	✓	✓

Table 4.9: Verification of the experimental observation of various compound AX$_2$ in chosen rutile and chiral phases.

These results of Tables 4.8 and 4.9 provide significant information concerning the role of the cation lone pair in promoting Z-point phonon instabilities in these AX_2 compounds. A visual representation of phonon band structure of the compounds in provided in Appendix C.

Firstly, in compounds where the cation lacks a lone pair, the calculations show no imaginary phonon modes at the Z-point. It means that these structures are dynamically stable with Z-point distortions. Correspondingly, Table 4.9 shows that these specific compounds (SnO_2, rutile-GeO_2, PbO_2) are indeed observed experimentally in the achiral rutile $P4_2/mnm$ phase and are typically not reported in the chiral $P4_12_12$ or $P4_32_12$.

Conversely, a strong correlation is observed between the presence of a lone pair on the cation and the existence of Z-point phonon instabilities in the hypothetical rutile parent phase. These instabilities are often strong, as indicated by the large imaginary frequencies (ω^2), and are often characterised by substantial energy gains (ΔE). This suggests that the anisotropic charge distribution induced by the lone pair causes the high-symmetry rutile structure to distort. It includes distortions that can lead to chirality.

These observations strongly suggest that the presence of the lone pair is a **necessary condition** for this type of Z-point instability, which can drive the transition from a rutile parent towards the $P4_12_12$ or $P4_32_12$ chiral structures.

However, the case of $PbCl_2$ is particularly instructive. While Pb^{2+} in $PbCl_2$ possesses a $6s^2$ lone pair, our calculations indicate no Z-point instability in its high-symmetry rutile parent phase. This crucial observation implies that while the presence of a lone pair appears necessary, it is not a sufficient condition on its own to guarantee a Z-point instability leading to chirality.

It leads to the question of what additional factors influence the occurrence of Z-point instabilities. The difference between $PbCl_2$ and PbF_2 indicates that the nature of the anion (X) has an influence. It could be through its electronegativity, size, and polarisation. Those will influence the bonding characteristics and the way the lone pair can express its stereochemical activity.

The situation with GeO_2 requires careful consideration. While rutile-GeO_2 is stable at the Z-point as discussed, Table 4.9 indicates that GeO_2 has been reported in the chiral $P4_12_12$ space group [74]. This necessitates a verification of the stability of that phase.

If a $P4_12_12$ GeO_2 phase is indeed experimentally accessible, it would imply that pathways to this chiral structure exist for GeO_2 and do not rely on a lone pair or a Z-point instability of a rutile parent. This does not contradict our hypothesis, which specifically concerns lone-pair-driven Z-point instabilities in rutile. It highlights that multiple routes to similar chiral symmetries can exist in different chemical systems. The focus here is on whether the lone pair allows a particular Z-point driven pathway from a common parent like rutile.

Regarding the magnitudes of the calculated energy gains (ΔE) in Table 4.8 for compounds like GeF_2, PbF_2 and SeO_2 (-437 eV/atom and -475 eV/atom, respectively), these values are indeed very large compared to SnF_2 (-0.088 eV/atom). Calculations need to be verified, as the values are extremely large for a phase transition. The discussion considers that the values are correct.

Such immense energy lowering upon distortion from the hypothetical rutile parent suggests that these rutile forms are possibly inexistent. This high degree of instability for the parent phase could explain why these specific chiral $P4_12_12$-type phases of GeF_2 or SeO_2 are not commonly observed experimentally or are perhaps only accessible as metastable phases under very specific synthesis conditions (Table 4.9). The system might prefer to adopt entirely different, more stable crystal structures rather than follow a displacive path from such a highly unfavourable rutile configuration, or the actual ground state might be reached via a reconstructive transition from a different parent.

In conclusion, this comparative study strongly indicates that the stereochemically active lone pair on the cation is likely a condition for the Z-point instabilities observed in the chosen compounds. However, its presence alone does not automatically ensure such a pathway to chirality. A specific mix between the electronic structure of the cation, the properties of the anion, and the overall energetic landscape of competing phases dictates whether such a chiral phase will be an observable and stable polymorph.

Chapter 5

Conclusion

This thesis explored whether structural chirality in solids can be treated as an order parameter in displacive phase transitions. Treating tin(II) fluoride (SnF_2) as a case study, the question was explored using first-principles simulations (DFT, DFPT) and symmetry analysis. The focus was put on a displacive transition from a hypothetical achiral high-symmetry parent phase to the chiral γ-SnF_2 phase $P4_12_12$, $P4_32_12$.

A rutile-type structure ($P4_2/mnm$) was characterised and proven to be a plausible high-symmetry parent phase for γ-SnF_2 phase. The calculations of its lattice dynamics revealed many significant instabilities. An unstable mode Z_4 at the Z-point was particularly interesting as it provided a displacive pathway towards chiral SnF_2 phases.
The condensation of this Z_4 mode along specific distortion domains ((a, a) and $(a, -a)$) was shown to lead directly to the enantiomorphic chiral space groups $P4_12_12$ and $P4_32_12$. With a substantial energy gain of -88 meV/atom, this confirmed a viable displacive pathway to chirality.

The evolution of chirality on a continuous transition path going from the achiral rutile reference phase to the chiral phase was quantified through the helicity H. H appears to be a good quantification parameter, as it is zero in the achiral phase and becomes non-zero in the chiral structure with a continuous evolution on the path, and it changes sign between the enantiomeric structures.

Natural Optical Activity (NOA), a physical manifestation of chirality, was quantified by the macroscopic rotatory power $\bar{\rho}$. The latter was derived from one component of the calculated NOA tensor η, η_{123}. The rotatory power $\bar{\rho}$ was calculated along the pathway and was found to correlate with the structural helicity.
A linear relationship, $\bar{\rho} \propto \mathcal{H}$, is observed for small to moderate distortions. This relationship supports the interpretation that helicity quantification and, hence, chirality, and the amplitude of the NOA are intimately linked. However, deviations from linearity at larger distortions indicate the presence of higher-order effects and/or a more complex connection between the detailed atomic structure and the electronic transitions governing NOA.

Another important observation was the impact of the unit cell on the magnitude of both helicity and NOA. Calculations performed with cell parameters fixed to those of the target chiral phase produced helicity and NOA values several orders of magnitude larger than those obtained with cell parameters constrained to the parent rutile phase. This highlights the important role of cell shape in stabilising chiral configurations in the rutile-like parent structures, while atomic displacements break the symmetry.

Beyond SnF_2, a comparative study across various AX_2 compounds was performed. It revealed a strong correlation between the presence of a stereochemically active lone pair and the existence of Z-point phonon instabilities that can drive chirality. However, exceptions like $PbCl_2$ demonstrated that the lone pair is probably a necessary but not sufficient condition. Other factors, such as the nature of the anion or competing structural phases, also play essential roles.

In summary, this work contributes to the growing understanding of chirality. It confirms the notion that chirality can emerge from well-defined lattice instabilities but also be quantified like a conventional order parameter. This opens the door to treating chirality not only as a geometric property but as a tunable and functional property in solid-state materials.

While this study provides significant insights, it also paves the way for further investigations.
To determine if chirality can be considered a ferroic order parameter, it is necessary to examine the existence of a conjugate field that allows for its switching. However, identifying a thermodynamically conjugate field to structural chirality remains a major theoretical challenge.
A key property of order parameters is their control. It is therefore interesting to explore how chirality (and NOA) could be tuned via pressure, strain, electric fields, or even magnetic fields. It would be essential for the development of new technological applications.
In this study, SnF_2 serves as an excellent model. Yet, to establish the generality of chirality as an order parameter in phonon-driven transitions, further studies on a wider range of materials exhibiting different crystal symmetries and chemical compositions are needed. The algorithmic approaches developed by Gómez-Ortiz et al. [12] could be instrumental for that purpose.
Some of the phases studied in this work remain hypothetical. Therefore, collaboration with experimental groups could help test the existence or synthesis of these chiral forms, especially under epitaxial conditions as recently done for TeO_2 [73].
Another possibility is the definition of new quantitative measures for chirality in periodic solids. Helicity is useful and intuitive, but another quantity could provide even deeper insights [4].

In conclusion, this thesis provides evidence supporting the consideration of structural chirality as a new order parameter for phonon-driven displacive phase transitions. This work enhances the understanding of SnF_2, but also contributes to a broader investigation. It helped to have additional insights about the question of the incorporation of chirality into the fundamental framework of ordering phenomena in condensed matter. The long-term vision is the design and control of chiral functionalities for innovative applications.

Appendix A

Convergence tests

The following appendix details the convergence tests performed to determine appropriate parameters ($ECUT$, k-point-grid) for calculations in this work. The graphs presented here focus on $\gamma{-}\mathrm{SnF}_2$, as it is a central phase for this work.

The convergence of the total energy and lattice parameters was tested. The goal was to obtain a precision lower than 1 $\mathrm{meV/atom}$ for the energy and around 0.001 Å for the cell parameters.

Figures A.1, A.2, A.3, A.4 show that a value of 40 Ha for the energy cut-off and a k point grid of $4 \times 4 \times 2$ respect those conditions. That justifies the value of parameters mentioned in Tab.4.3.

Similar convergence criteria were applied to other phases and calculations to ensure reliability of the results.

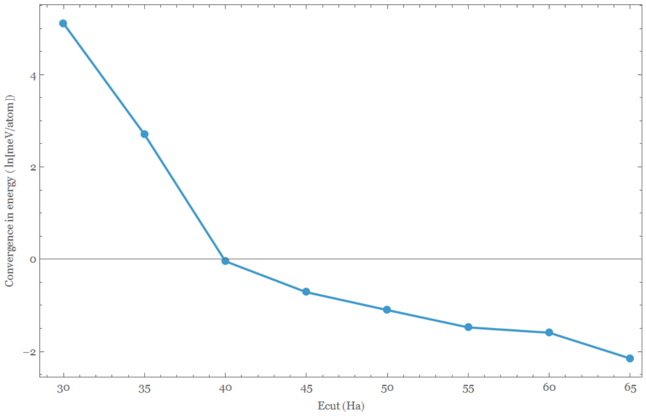

Figure A.1: Convergence of the total energy (relative difference in $\mathrm{meV/atom}$) of γ-SnF_2 as a function of the plane-wave energy cutoff (Ecut, in Ha). The energy at the highest Ecut is taken as the reference.

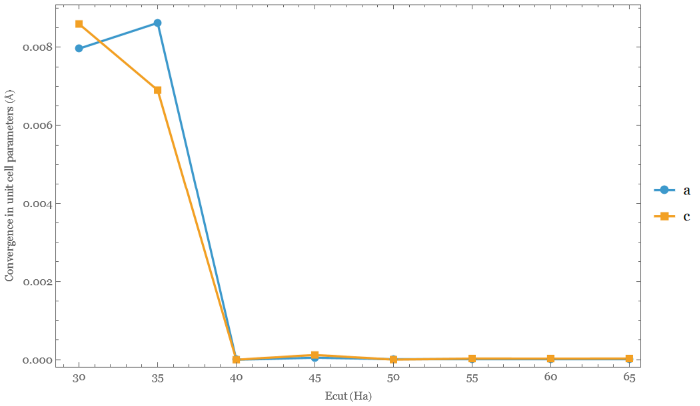

Figure A.2: Convergence of the lattice parameters a (blue) and c (orange) of γ-SnF$_2$ (absolute difference in Å) as a function of the plane-wave energy cutoff (Ecut, in Ha). The parameters at the highest Ecut are taken as the reference.

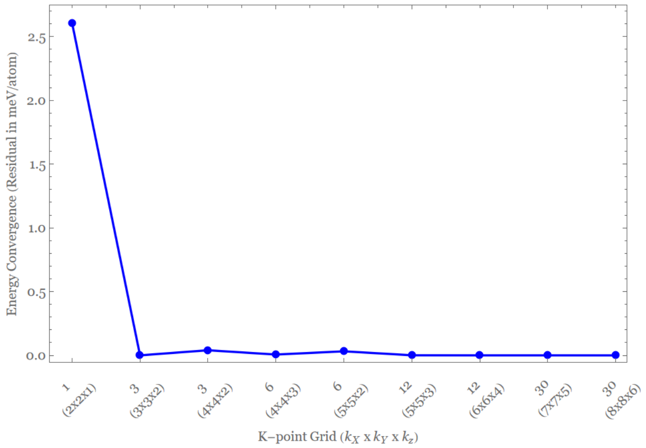

Figure A.3: Convergence of the total energy residual (in meV/atom) of γ-SnF$_2$ as a function of the k-point grid density. The x-axis shows the number of irreducible k-points (Nkpt) and the corresponding $(k_x \times k_y \times k_z)$ grid.

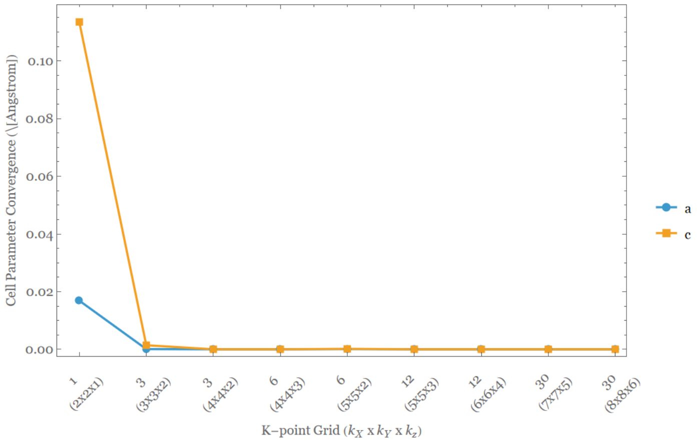

Figure A.4: Convergence of the lattice parameter changes Δa (blue) and Δc (orange) (in Å) of γ-SnF$_2$ r as a function of the k-point grid density. The x-axis shows the number of irreducible k-points (Nkpt) and the corresponding $(k_x \times k_y \times k_z)$ grid.

Appendix B

Detailed atomic positions

This appendix provides the calculated reduced atomic coordinates for the key structures discussed in Chapter 4. All coordinates are given in units of the respective lattice vectors.

Atom	**x**	**y**	**z**
Sn	0.0000	0.0000	0.0000
Sn	0.5000	0.5000	0.2500
F	0.3062	0.6938	0.0000
F	0.6938	0.3062	0.0000
F	0.1938	0.1938	0.2500
F	0.8062	0.8062	0.2500
Sn	0.0000	0.0000	0.5000
Sn	0.5000	0.5000	0.7500
F	0.3062	0.6938	0.5000
F	0.6938	0.3062	0.5000
F	0.1938	0.1938	0.7500
F	0.8062	0.8062	0.7500

Table B.1: Calculated reduced atomic coordinates for SnF_2 in the rutile $P2/mnm$ structure. It uses a $1 \times 1 \times 2$ supercell based on the primitive rutile cell to match the periodicity of the Z-point distortion. These coordinates represent the 0% distortion reference point.

Atom	**x**	**y**	**z**
Sn	0.0164	0.0164	0.5000
Sn	0.4836	0.5164	0.7500
F	0.2503	0.6404	0.4262
F	0.6404	0.2503	0.5738
F	0.2497	0.1404	0.8238
F	0.8596	0.7503	0.6762
Sn	0.9836	0.9836	0.0000
Sn	0.5164	0.4836	0.2500
F	0.3596	0.7497	0.0738
F	0.7497	0.3596	0.9262
F	0.1404	0.2497	0.1762
F	0.7503	0.8596	0.3238

(a) Right enantiomer ($P4_12_12$)

Atom	**x**	**y**	**z**
Sn	0.0164	0.0164	0.5000
Sn	0.5164	0.4836	0.7500
F	0.2503	0.6404	0.5738
F	0.6404	0.2503	0.4262
F	0.1404	0.2497	0.8238
F	0.7503	0.8596	0.6762
Sn	0.9836	0.9836	0.0000
Sn	0.4836	0.5164	0.2500
F	0.3596	0.7497	0.9262
F	0.7497	0.3596	0.0738
F	0.2497	0.1404	0.1762
F	0.8596	0.7503	0.3238

(b) Left enantiomer ($P4_32_12$)

Table B.2: Calculated reduced atomic positions of fully relaxed SnF_2 in its two enantiomorphic forms. These coordinates correspond to the 100% and -100% distortion points when using relaxed chiral cell parameters.

Atom	**x**	**y**	**z**
Sn	0.9978	0.9978	0.5000
Sn	0.5022	0.4978	0.7500
F	0.2527	0.6587	0.4363
F	0.6587	0.2527	0.5637
F	0.2473	0.1587	0.8137
F	0.8413	0.7527	0.6863
Sn	0.0022	0.0022	0.0000
Sn	0.4978	0.5022	0.2500
F	0.3413	0.7473	0.0637
F	0.7473	0.3413	0.9363
F	0.1587	0.2473	0.1863
F	0.7527	0.8413	0.3137

(a) Right enantiomer ($P4_12_12$)

Atom	**x**	**y**	**z**
Sn	0.9978	0.9978	0.5000
Sn	0.4978	0.5022	0.7500
F	0.2527	0.6587	0.5637
F	0.6587	0.2527	0.4363
F	0.1587	0.2473	0.8137
F	0.7527	0.8413	0.6863
Sn	0.0022	0.0022	0.0000
Sn	0.5022	0.4978	0.2500
F	0.3413	0.7473	0.9363
F	0.7473	0.3413	0.0637
F	0.2473	0.1587	0.1863
F	0.8413	0.7527	0.3137

(b) Left enantiomer ($P4_32_12$)

Table B.3: Calculated reduced atomic positions of fully relaxed SnF_2 in its two enantiomorphic forms. These coordinates correspond to the 100% and -100% distortion points when the structure is constrained to fixed rutile cell parameters.

The atomic displacement field, $\Delta\mathbf{r}_{red}$, that transforms the undistorted rutile structure (Table B.2) into the fully distorted chiral structures (100% distortion, Tables B.2 and B.3), can now be determined.
To correctly map atoms between the parent rutile cell and the doubled cell resulting from the Z-point

mode condensation, a reference shift along the z-axis is applied when calculating these displacements. The following tables present these reduced displacement vectors for both enantiomers under both cell constraint conditions.

Atom	Δx	Δy	Δz
Sn	-0.0164	-0.0164	0.0000
Sn	0.0164	-0.0164	0.0000
F	0.0559	0.0534	0.0738
F	0.0534	0.0559	-0.0738
F	-0.0559	0.0534	-0.0738
F	-0.0534	0.0559	0.0738
Sn	0.0164	0.0164	0.0000
Sn	-0.0164	0.0164	0.0000
F	-0.0534	-0.0559	-0.0738
F	-0.0559	-0.0534	0.0738
F	0.0534	-0.0559	0.0738
F	0.0559	-0.0534	-0.0738

(a) $\Delta \mathbf{x}_{\text{red}}$ — $P4_12_12$

Atom	Δx	Δy	Δz
Sn	-0.0164	-0.0164	0.0000
Sn	-0.0164	0.0164	0.0000
F	0.0559	0.0534	-0.0738
F	0.0534	0.0559	0.0738
F	0.0534	-0.0559	-0.0738
F	0.0559	-0.0534	0.0738
Sn	0.0164	0.0164	0.0000
Sn	0.0164	-0.0164	0.0000
F	-0.0534	-0.0559	0.0738
F	-0.0559	-0.0534	-0.0738
F	-0.0559	0.0534	0.0738
F	-0.0534	0.0559	-0.0738

(b) $\Delta \mathbf{x}_{\text{red}}$ — $P4_32_12$

Table B.4: Reduced displacement vectors $\Delta \mathbf{r}_{\text{red}}$ from the reference rutile positions (Table B.1, with a z-axis shift of 0.5 applied to reference coordinates) to the two chiral distortion patterns (Table B.2) calculated using fixed chiral cell parameters.

Atom	Δx	Δy	Δz
Sn	0.0022	0.0022	0.0000
Sn	-0.0022	0.0022	0.0000
F	0.0535	0.0351	0.0637
F	0.0351	0.0535	-0.0637
F	-0.0535	0.0351	-0.0637
F	-0.0351	0.0535	0.0637
Sn	-0.0022	-0.0022	0.0000
Sn	0.0022	-0.0022	0.0000
F	-0.0351	-0.0535	-0.0637
F	-0.0535	-0.0351	0.0637
F	0.0351	-0.0535	0.0637
F	0.0535	-0.0351	-0.0637

(a) $\Delta \mathbf{x}_{\text{red}}$ — $P4_12_12$

Atom	Δx	Δy	Δz
Sn	0.0022	0.0022	0.0000
Sn	0.0022	-0.0022	0.0000
F	0.0535	0.0351	-0.0637
F	0.0351	0.0535	0.0637
F	0.0351	-0.0535	-0.0637
F	0.0535	-0.0351	0.0637
Sn	-0.0022	-0.0022	0.0000
Sn	-0.0022	0.0022	0.0000
F	-0.0351	-0.0535	0.0637
F	-0.0535	-0.0351	-0.0637
F	-0.0535	0.0351	0.0637
F	-0.0351	0.0535	-0.0637

(b) $\Delta \mathbf{x}_{\text{red}}$ — $P4_32_12$

Table B.5: Reduced displacement vectors $\Delta \mathbf{r}_{\text{red}}$ from the reference rutile positions (Table B.1, with a z-axis shift of 0.5 applied to reference coordinates) to the two chiral distortion patterns (Table B.3) calculated using fixed rutile cell parameters.

Appendix C

Phonon band structures of AX_2 compounds

This appendix presents the calculated phonon band structures for several AX_2 compounds that were analysed in Section 4.4. All structures were considered in their hypothetical rutile-type phase (space group $P4_2/mnm$, No. 136).

The phonon dispersions are plotted along the same high-symmetry k-point path used for rutile-SnF_2 in Figure 4.9 : $\Gamma - X - M - \Gamma - Z - R - A - Z - R - X$. Phonon frequencies are presented in units of eV.

The phonon dispersions presented visually support the discussion in Section ??. When considered in a hypothetical rutile parent structure, AX_2 compounds with active cation lone pairs tend to exhibit significant Z-point (and other) phonon instabilities, while those without lone pairs show dynamically stable rutile phases.

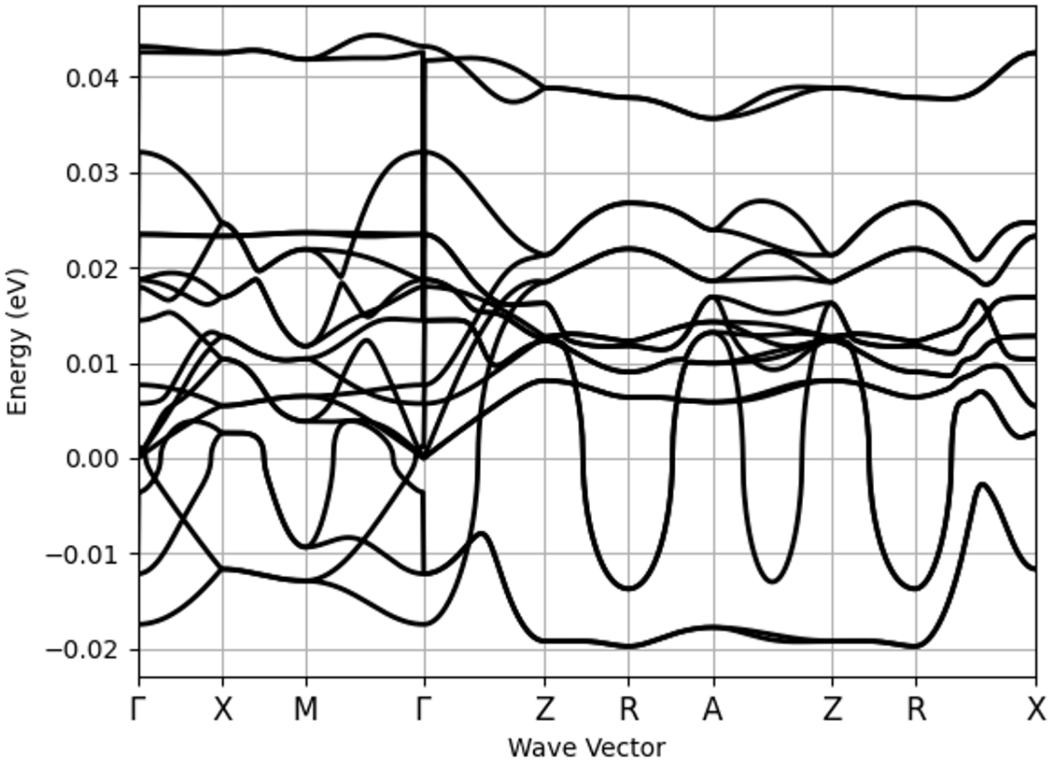

Figure C.1: Calculated phonon band structure of rutile-type SnF_2 ($P4_2/mnm$). Imaginary frequencies (negative values) are observed at all symmetry points.

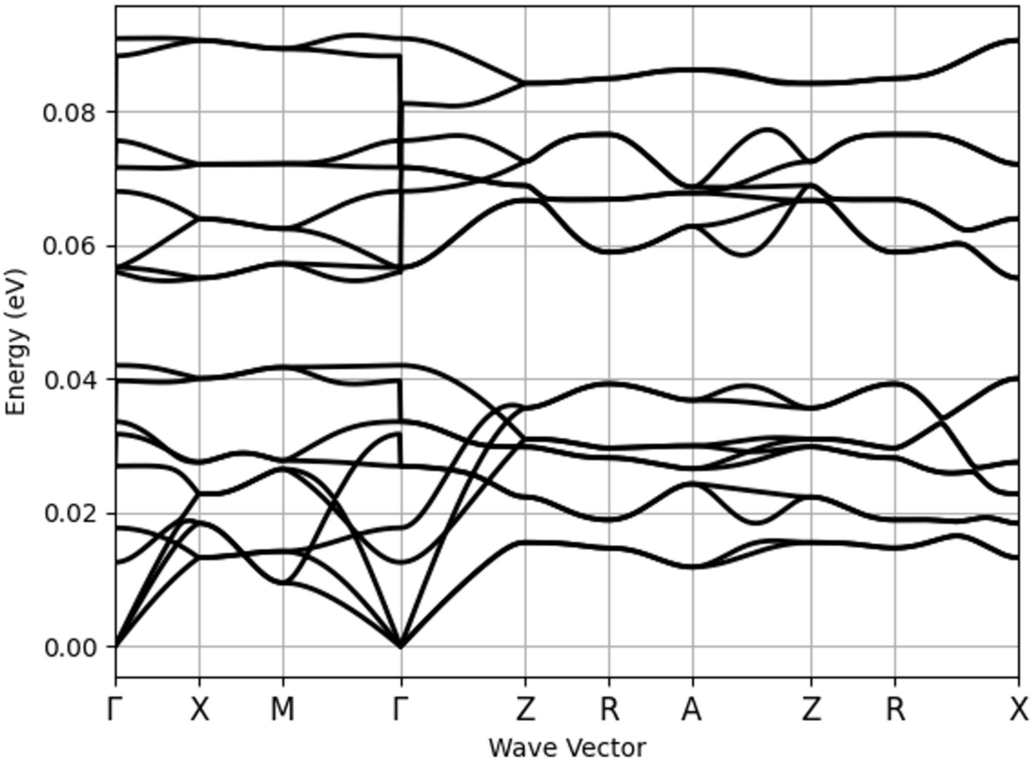

Figure C.2: Calculated phonon band structure of rutile-type SnO_2 ($P4_2/mnm$). No imaginary frequencies are observed along the plotted path, consistent with the dynamical stability of this phase.

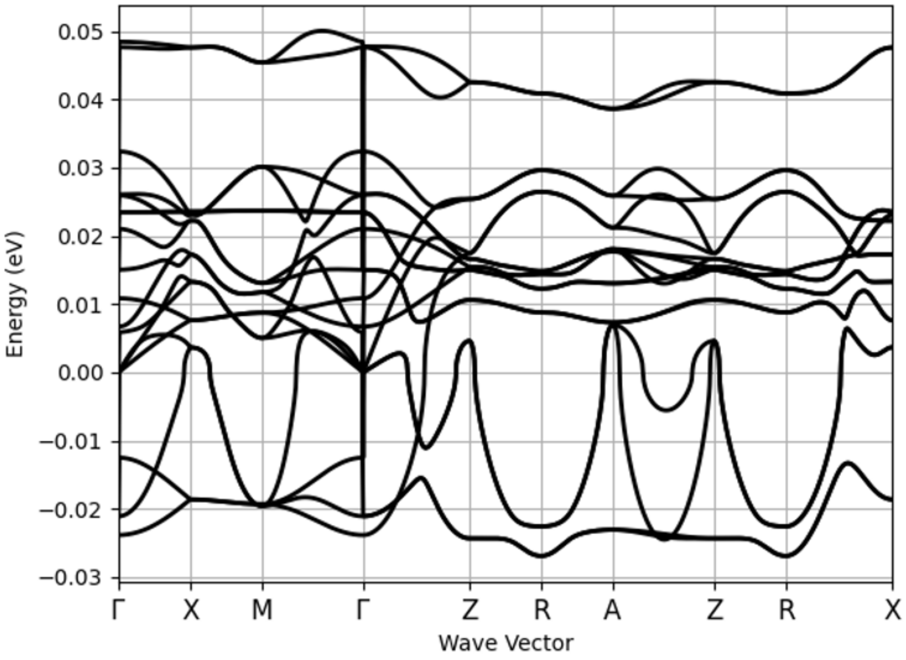

Figure C.3: Calculated phonon band structure of hypothetical rutile-type GeF_2 ($P4_2/mnm$). Imaginary frequencies (negative values) are observed at all symmetry points.

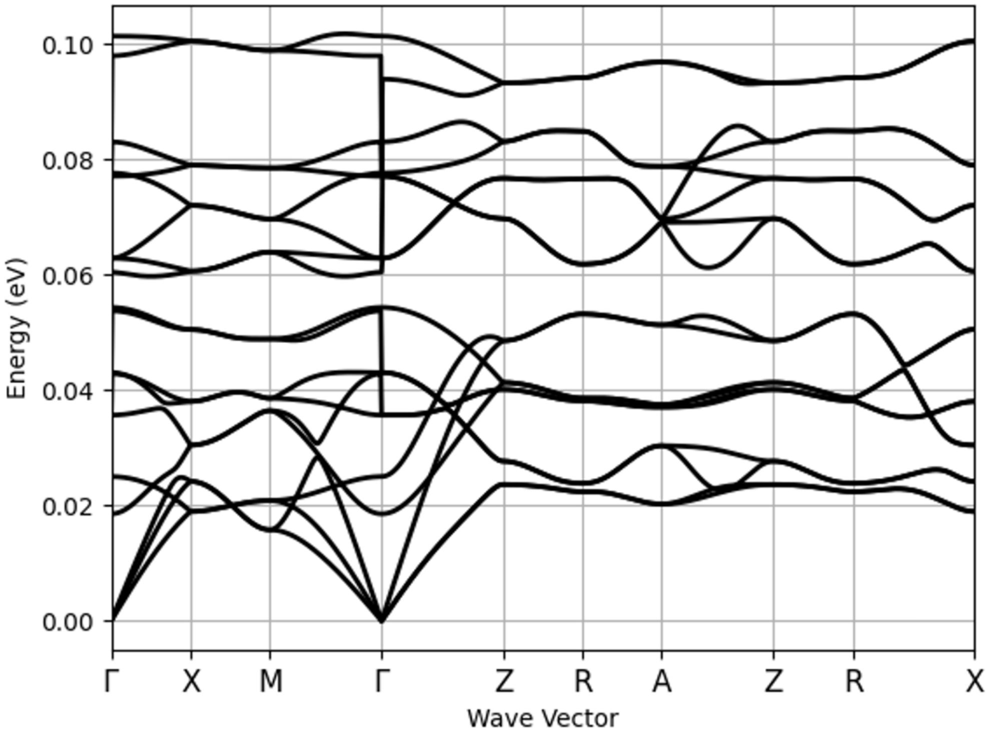

Figure C.4: Calculated phonon band structure of rutile-type GeO$_2$ ($P4_2/mnm$). No imaginary frequencies are observed along the plotted path, consistent with the dynamical stability of this phase.

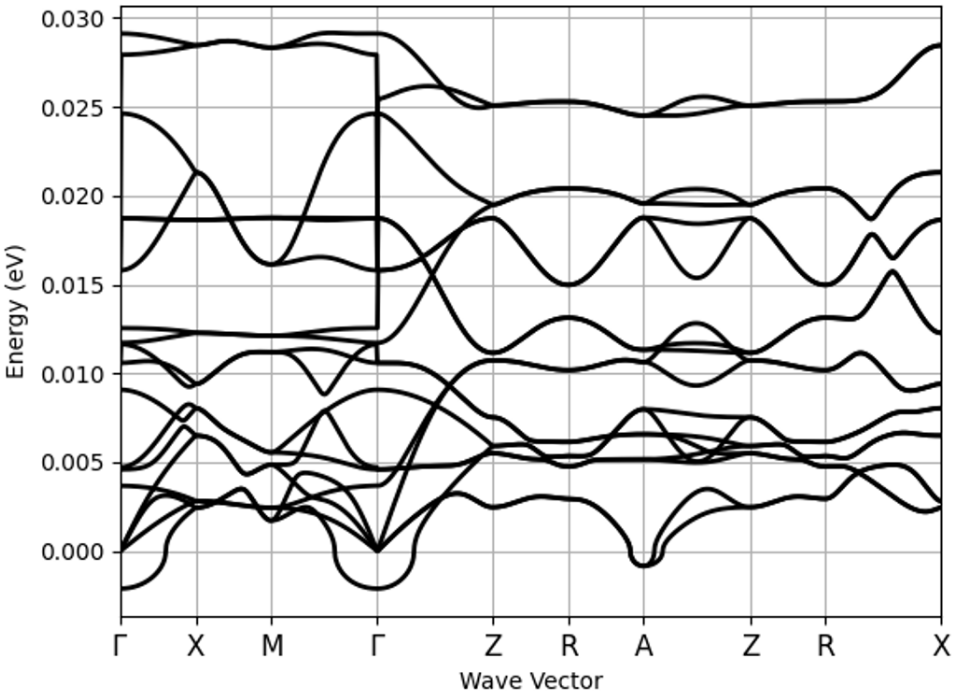

Figure C.5: Calculated phonon band structure of rutile-type PbCl$_2$ ($P4_2/mnm$). Imaginary frequencies (negative values) are observed, particularly at the Γ, and A points.

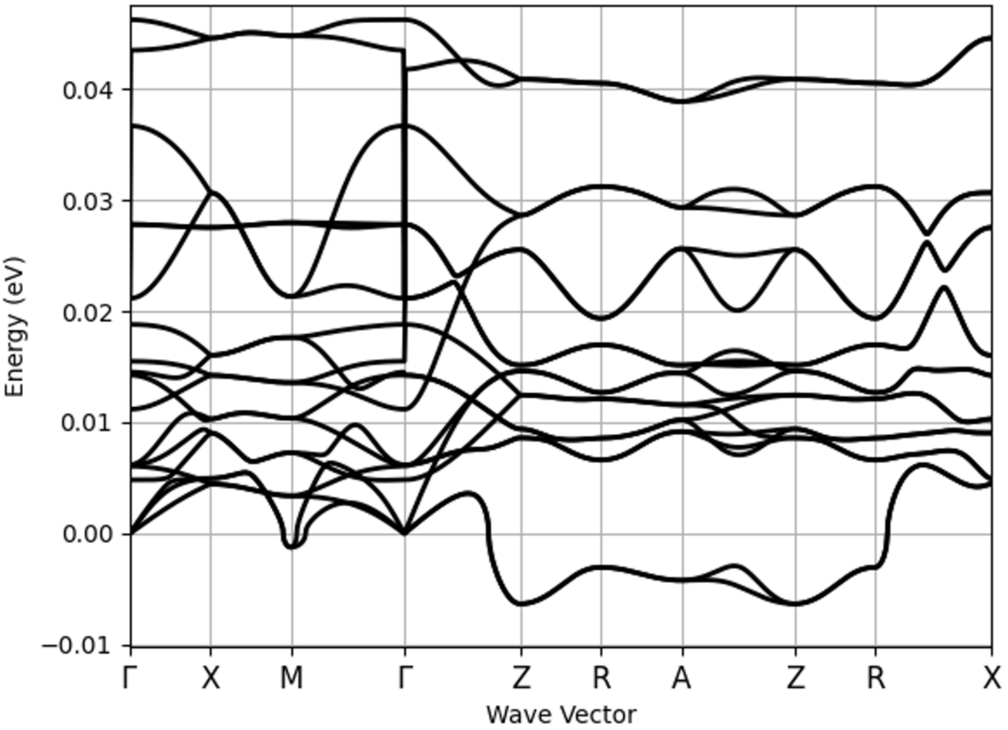

Figure C.6: Calculated phonon band structure of rutile-type PbF_2 ($P4_2/mnm$). Imaginary frequencies (negative values) are observed, particularly at the Z, M, R and A points.

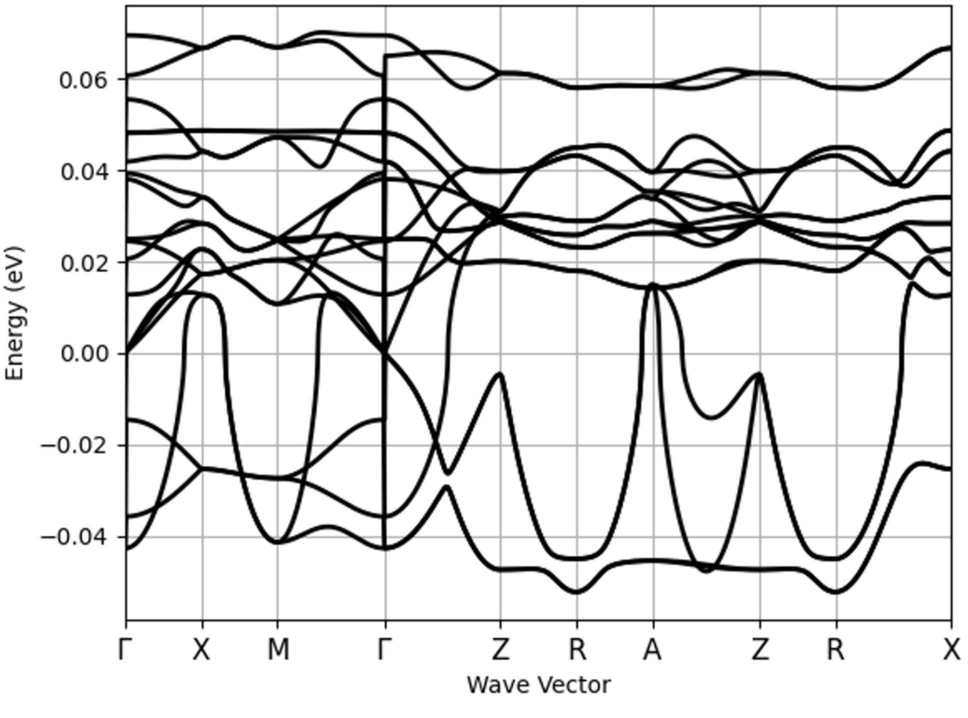

Figure C.7: Calculated phonon band structure of rutile-type SeO_2 ($P4_2/mnm$). Imaginary frequencies (negative values) are observed at all symmetry points.

Bibliography

[1] Gerhard H. Fecher, Jürgen Kübler, and Claudia Felser. Chirality in the solid state: Chiral crystal structures in chiral and achiral space groups. *Materials*, 15(17):5812, 2022. doi: 10.3390/ma15175812. URL https://www.mdpi.com/1996-1944/15/17/5812.

[2] Joseph Gal. Molecular chirality in chemistry and biology: Historical milestones. *Helvetica Chimica Acta*, 96(9):1617–1657, 2013. doi: https://doi.org/10.1002/hlca.201300300. URL https://onlinelibrary.wiley.com/doi/abs/10.1002/hlca.201300300.

[3] Chris L Lin. Chirality through classical physics. *European Journal of Physics*, 41(4):045802, jun 2020. doi: 10.1088/1361-6404/ab895d. URL https://dx.doi.org/10.1088/1361-6404/ab895d.

[4] Eric Bousquet, Mauro Fava, Zachary Romestan, Fernando Gómez-Ortiz, Emma E. McCabe, and Aldo H. Romero. Structural chirality and related properties in periodic inorganic solids: review and perspectives. *Journal of Physics: Condensed Matter*, 37(18), 2025. doi: 10.1088/1361-648X/adb674.

[5] Seo-Hyeon Ham, Moon Han, and Minkyu Kim. Chiral materials for optics and electronics: Ready to rise? *Micromachines*, 15:528, 04 2024. doi: 10.3390/mi15040528.

[6] Jae-Hyun Lee, Hyeon-Jin Kim, Jae-Hyun Kim, and Young-Kyun Kim. Recent advances in chiral nanomaterials with unique electric and magnetic properties. *Nano Convergence*, 9(1):32, 2022. doi: 10.1186/s40580-022-00322-w.

[7] G. Denes, J. Pannetier, and J. Lucas. About snf2 stannous fluoride. ii. crystal structure of $\beta-$ and $\gamma-$snf$_2$. *Journal of Solid State Chemistry*, 33(1):1–11, 1980. ISSN 0022-4596. doi: https://doi.org/10.1016/0022-4596(80)90541-1. URL https://www.sciencedirect.com/science/article/pii/0022459680905411.

[8] G. Denes. About SnF$_2$ stannous fluoride. IV. Kinetics of the $\alpha \to \gamma$ and β, $\gamma \to \alpha$ transitions. *Journal of Solid State Chemistry*, 37(1):16–23, 1981. doi: 10.1016/0022-4596(81)90003-7.

[9] G. Denes, J. Pannetier, J. Lucas, and J.Y. Le Marouille. About snf$_2$ stannous fluoride. i. crystallochemistry of α-snf$_2$. *Journal of Solid State Chemistry*, 30(3):335–343, 1979. ISSN 0022-4596. doi: https://doi.org/10.1016/0022-4596(79)90245-7. URL https://www.sciencedirect.com/science/article/pii/0022459679902457.

[10] Georges Dénès. About snf$_2$ stannous fluoride. vi. phase transitions. *Materials Research Bulletin*, 15(6):807–819, 1980. ISSN 0025-5408. doi: 10.1016/0025-5408(80)90015-X.

[11] Mauro Fava, Emma McCabe, Aldo H. Romero, and Eric Bousquet. A phonon-driven mechanism for an emergent and reversible chirality in crystals. *arXiv preprint arXiv:2407.19706*, 2024. URL https://arxiv.org/abs/2407.19706. Submitted July 30, 2024.

[12] Fernando Gómez-Ortiz, Aldo H. Romero, and Eric Bousquet. Pathways to crystal chirality: An algorithm to identify new displacive chiral phase transitions. *arXiv preprint arXiv:2503.13076*, 2025. URL `https://doi.org/10.48550/arXiv.2503.13076`. Submitted on 17 Mar 2025.

[13] Fernando Gómez-Ortiz, Mauro Fava, Emma E. McCabe, Aldo H. Romero, and Eric Bousquet. Structural chirality measurements and computation of handedness in periodic solids. *Physical Review B*, 110(17):174112, November 2024. doi: 10.1103/PhysRevB.110.174112.

[14] Kevin Mowery. An introduction to chirality. `https://www.makingmolecules.com/blog/chirality`, 2021. Accessed: 2024-10-21.

[15] Hiroshi Yamamoto. Distinguishing between right and left with magnets – electron spins reflect chiral molecules without the mirror. `https://www.ims.ac.jp/en/news/2023/01/0119.html`, 2023. Accessed: 2024-10-21.

[16] Anne Zehnacker and Pascale Roubin. Petite histoire de la chiralité, de pasteur à la physique d'aujourd'hui. *Reflets de la Physique*, (73):5–9, 2022. URL `https://www.refletsdelaphysique.fr/articles/refdp/pdf/2022/03/refdp202273p5.pdf`.

[17] Étienne Louis Malus. Sur une propriété de la lumière réfléchie. *Mémoires de physique et de chimie de la Société d'Arcueil*, 2:143–158, 1809.

[18] François Arago. Mémoire sur une modification remarquable qu'éprouvent les rayons lumineux dans leur passage à travers certains corps diaphanes, et sur quelques autres nouveaux phénomènes d'optique. *Mémoires de la classe des sciences mathématiques et physiques de l'Institut Impérial de France*, 1:93–134, 1811. URL `https://books.google.com/books/about/MÃlmoire_sur_une_modification_remarquabl.html?id=xgU-MwEACAAJ`.

[19] Jean-Baptiste Biot. Sur de nouveaux rapports qui existent entre la réflexion et la polarisation de la lumière des corps cristallisés. *Mémoires de la classe des sciences mathématiques et physiques de l'Institut Impérial de France*, 13:1–X, 1812.

[20] René-Just Haüy. *Traité de minéralogie, Tome 1*. Chez Louis, 1801. URL `https://gallica.bnf.fr/ark:/12148/bpt6k3898g.texteImage`.

[21] Robert Glaser. Hemihedralism in quartz crystals: Setting the stage for the birth of stereochemistry. In *Symmetry, Spectroscopy, and Crystallography: The Structural Nexus*, pages 43–. Wiley-VCH, 2015. ISBN 978-3-527-33847-3. doi: 10.1002/9783527684199.refs. URL `https://doi.org/10.1002/9783527684199.refs`.

[22] John F. W. Herschel. On the rotation impressed by plates of rock crystal on the planes of polarization of the rays of light, as connected with certain peculiarities in its crystallization. *Transactions of the Cambridge Philosophical Society*, 1:43–51, 1820.

[23] Jean-Baptiste Biot. Phénomène de polarisation successive, observés dans des fluides homogènes. *Bulletin des Sciences, par la Société Philomatique de Paris*, pages 190–192, 1815. URL `https://www.biodiversitylibrary.org/item/26553`.

[24] Louis Pasteur. Recherches sur les relations qui peuvent exister entre la forme cristalline, la composition chimique et le sens de la polarisation rotatoire. *Annales de Chimie et de Physique*, 24(3):442–459, 1848.

[25] Johannes Wislicenus. Ueber die räumliche Anordnung der Atome in organischen Molekülen und ihre Beziehungen zur physiologischen Wirkung der letzteren. *Berichte der Deutschen Chemischen Gesellschaft*, 17:1853–1862, 1884. doi: 10.1002/cber.188401702142. URL `https://onlinelibrary.wiley.com/doi/abs/10.1002/cber.188401702142`.

[26] Louis Pasteur. Mémoire sur la fermentation alcoolique. *Comptes Rendus de l'Académie des Sciences*, 45:1032–1036, 1857. URL `https://gallica.bnf.fr/ark:/12148/bpt6k2990c/f1036.item`.

[27] Lord Kelvin William Thomson. *Baltimore Lectures on Molecular Dynamics and the Wave Theory of Light*. C.J. Clay and Sons, Cambridge University Press, Cambridge, 1904. URL `https://archive.org/details/baltimorelecture00kelviala`. Lecture series delivered at Johns Hopkins University in 1884–1885.

[28] Donna G. Blackmond. The origin of biological homochirality. *Cold Spring Harbor Perspectives in Biology*, 2(5):a002147, 2010. doi: 10.1101/cshperspect.a002147. URL `https://doi.org/10.1101/cshperspect.a002147`.

[29] Joseph Achille Le Bel. Sur les relations qui existent entre les formules atomiques des corps organiques et le pouvoir rotatoire de leurs dissolutions. *Bulletin de la Société Chimique de France*, 22: 337–347, 1874. URL `https://gallica.bnf.fr/ark:/12148/bpt6k54945584/f345.item`. Consulté le 5 avril 2025.

[30] Pierre Curie. Sur la symétrie dans les phénomènes physiques, symétrie d'un champ électrique et d'un champ magnétique. *Journal de Physique Théorique et Appliquée*, 3(1):393–415, 1894. doi: 10.1051/jphystap:018940030039300. URL `https://doi.org/10.1051/jphystap:018940030039300`.

[31] Lord Kelvin Sir William Thomson. *The Molecular Tactics of a Crystal*. Clarendon Press, Oxford, 1894. URL `https://archive.org/details/moleculartactics00kelviala`.

[32] Pedro Cintas. Tracing the origins and evolution of chirality and handedness in chemical language. *Angewandte Chemie International Edition*, 46(22):4016–4024, May 2007. doi: 10.1002/anie.200603714.

[33] James H. Kim and Anthony R. Scialli. Thalidomide: the tragedy of birth defects and the effective treatment of disease. *Toxicological Sciences*, 122(1):1–6, 2011. doi: 10.1093/toxsci/kfr088. URL `https://doi.org/10.1093/toxsci/kfr088`.

[34] L. D. Barron. True and false chirality and parity violation. *Chemical Physics Letters*, 123(5):423–427, 1986. doi: 10.1016/0009-2614(86)80205-4.

[35] Zbigniew Dauter and Mariusz Jaskolski. How to read (and understand) volume a of international tables for crystallography: An introduction for nonspecialists. *Journal of Applied Crystallography*, 43(43):1150–1171, 2010. doi: 10.1107/S0021889810026956. Figure 8: The 14 Bravais lattices.

[36] Aleksandr Shirokanev, D. V. Kirsh, and Alexander Kupriyanov. The study of effectiveness of a high-performance crystal lattice parametric identification algorithm based on cuda technology. *Journal of Physics: Conference Series*, 1368(5):052040, 2019. doi: 10.1088/1742-6596/1368/5/052040. Figure 1: Bravais unit cells of seven lattice systems.

[37] H. Zabrodsky and D. Avnir. Continuous symmetry measures. 4. chirality. *Journal of the American Chemical Society*, 117(2):462–473, 1995. doi: 10.1021/ja00106a010.

[38] M. Pinsky and D. Avnir. Continuous symmetry measures. 5. the classical polyhedra. *Inorganic Chemistry*, 37(21):5575–5582, 1998. doi: 10.1021/ic9804925.

[39] Andrzej B. Buda and Kurt Mislow. A hausdorff chirality measure. *Journal of the American Chemical Society*, 114(15):6006–6012, 1992. doi: 10.1021/ja00041a016. URL `https://doi.org/10.1021/ja00041a016`.

[40] André Rassat and Patrick W. Fowler. Is there a “most chiral tetrahedron”? *Chemistry – A European Journal*, 10(24):6575–6580, 2004. doi: 10.1002/chem.200400869. URL `https://doi.org/10.1002/chem.200400869`.

[41] A. M. Glazer and K. Stadnicka. On the origin of optical activity in crystal structures. *Journal of Applied Crystallography*, 19(2):108–122, April 1986. doi: 10.1107/S0021889886089823.

[42] J. F. Nye. *Physical Properties of Crystals: Their Representation by Tensors and Matrices.* Oxford University Press, 1985. ISBN 9780198511656. URL `https://books.google.fr/books?hl=fr&lr=&id=ugwql-uVB44C&oi=fnd&pg=PR5&dq=physical+origins+of+optical+activity+Nye&ots=M9GqZH5TST&sig=X6NJHnEMcnWx8KXzMcst3y1Vczc#v=onepage&q&f=false`.

[43] S. Fukuda, T. Shiosaki, and A. Kawabata. Infrared optical activity in tellurium. *physica status solidi (b)*, 68(2):K107–K110, 1975. doi: 10.1002/pssb.2220680247.

[44] Hans Ch. Siegmann and Joachim Stöhr. *Magnetism: From Fundamentals to Nanoscale Dynamics*, volume 152 of *Springer Series in Solid-State Sciences*. Springer, Berlin, 2006. ISBN 978-3-540-30283-5.

[45] L. D. Landau and E. M. Lifshitz. *Electrodynamics of Continuous Media*, volume 8 of *Course of Theoretical Physics*. Pergamon Press, Oxford, 2nd edition, 1984. ISBN 978-0-08-030275-1. URL `https://www.sciencedirect.com/book/9780080302751/electrodynamics-of-continuous-media`.

[46] Asier Zabalo and Massimiliano Stengel. Natural optical activity from density-functional perturbation theory. *Physical Review Letters*, 131(8):086902, August 2023. doi: 10.1103/PhysRevLett.131.086902.

[47] Asier Zabala. *First-principles theory of spatial dispersion.* Phd thesis, Universitat Autònoma de Barcelona, 2024. URL `https://www.tesisenred.net/handle/10803/693116#page=1`.

[48] Louis Bastogne. Étude et modélisation du titanate de plomb au départ des premiers et seconds principes. Master thesis, Université de Liège, 2019-2020. URL `https://matheo.uliege.be/handle/2268.2/9382`.

[49] Pierre Hohenberg and Walter Kohn. Inhomogeneous electron gas. *Physical Review*, 136(3B):B864, 1964.

[50] Feliciano Giustino. *Materials Modelling using Density Functional Theory: Properties and Predictions.* Oxford University Press, Oxford, 2014. ISBN 9780199662447.

[51] Philippe Ghosez. Materials modelling: Chapter 2, practical density functional theory, 2024. Lecture slides, Université de Liège, Département de Physique, Physique Théorique des Matériaux.

[52] John P. Perdew, Kieron Burke, and Matthias Ernzerhof. Generalized gradient approximation made simple. *Physical Review Letters*, 77(18):3865–3868, October 1996. doi: 10.1103/PhysRevLett.77.3865. URL `https://doi.org/10.1103/PhysRevLett.77.3865`.

[53] John P. Perdew, Adrienn Ruzsinszky, Gábor I. Csonka, Oleg A. Vydrov, Gustavo E. Scuseria, Lucian A. Constantin, Xiaolan Zhou, and Kieron Burke. Erratum: Restoring the density-gradient expansion for exchange in solids and surfaces. *Physical Review Letters*, 102(3):039902, January 2009. doi: 10.1103/PhysRevLett.102.039902. URL `https://doi.org/10.1103/PhysRevLett.102.039902`.

[54] L. Bastogne and Ph. Ghosez. PHYS0981: Quantum modelling of materials properties – Summary cards. Lecture slides, 2024-2025. Lecture notes, University of Liège.

[55] Felix Bloch. Über die quantenmechanik der elektronen in kristallgittern. *Zeitschrift für Physik*, 52(7-8):555–600, 1929.

[56] Neil W Ashcroft and N David Mermin. *Solid State Physics*. Holt, Rinehart and Winston, 1976.

[57] D. R. Hamann. Optimized norm-conserving vanderbilt pseudopotentials. *Physical Review B*, 88 (8):085117, 2013.

[58] R. M. Sternheimer. Electronic polarizabilities of ions from the perturbation-theory wave functions. *Physical Review*, 96:951–968, 1954.

[59] Xavier Gonze. Adiabatic density-functional perturbation theory. *Physical Review A*, 52(2):1096–1114, 1995. doi: 10.1103/PhysRevA.52.1096.

[60] Stefano Baroni, Stefano de Gironcoli, Andrea Dal Corso, and Paolo Giannozzi. Phonons and related crystal properties from density-functional perturbation theory. *Reviews of Modern Physics*, 73(2):515, 2001.

[61] Laxmi Narayana Patro and K. Hariharan. Ac conductivity and scaling studies of polycrystalline snf. *Journal of Non-Crystalline Solids*, 353(47–51):4473–4477, 2007. doi: 10.1016/j.jnoncrysol.2007.08.043. URL `https://doi.org/10.1016/j.jnoncrysol.2007.08.043`.

[62] L.H. Hove, B. Holme, A. Young, and A.B. Tveit. The protective effect of tif4, snf2 and naf against erosion-like lesions in situ. *Caries Research*, 42(1):68–72, 12 2007. ISSN 0008-6568. doi: 10.1159/000112816. URL `https://doi.org/10.1159/000112816`.

[63] Chaochao Wei, Chen Liu, Yujie Xiao, Zhongkai Wu, Qiyue Luo, Ziling Jiang, Zhenyu Wang, Long Zhang, Shijie Cheng, and Chuang Yu. Snf-induced multifunctional interface-stabilized li.ps.cl.-based all-solid-state lithium metal batteries. *Advanced Energy Materials*, 10(44):2002682, 2020. doi: 10.1002/aenm.202002682. URL `https://doi.org/10.1002/aenm.202002682`.

[64] Lian Shen, Lanyao Shen, Zhaoxiang Wang, and Liquan Chen. Lithium storage in heat-treated snf/polyacrylonitrile anode. *Chemistry – A European Journal*, 21(25):9352–9357, 2015. doi: 10.1002/chem.201500620. URL `https://doi.org/10.1002/chem.201500620`.

[65] Jingyu Guo, Abudukadi Tudi, Shujuan Han, Zhihua Yang, and Shilie Pan. -snf: A uv birefringent material with large birefringence and easy crystal growth. *Angewandte Chemie International Edition*, 59(50):22494–22498, 2020. doi: 10.1002/anie.202014279. URL `https://doi.org/10.1002/anie.202014279`.

[66] Materials Project. Materials data for -SnF$_2$ (mp-2843) from the Materials Project. `https://next-gen.materialsproject.org/materials/mp-2843`, 2024. Accessed on 22 Oct 2024.

[67] Materials Project. Materials data for -SnF$_2$ (mp-7456) from the Materials Project. `https://next-gen.materialsproject.org/materials/mp-7456`, 2024. Accessed on 22 Oct 2024.

[68] Materials Project. Materials data for -SnF$_2$ (mp-7457) from the Materials Project. `https://next-gen.materialsproject.org/materials/mp-7457`, 2024. Accessed on 22 Oct 2024.

[69] Thomas Birchall, Georges Dénès, Krzysztof Ruebenbauer, and Jean Pannetier. A tin-119 mössbauer study of the phase transitions in snf. *Journal of the Chemical Society, Dalton Transactions*, pages 1831–1836, 1981. doi: 10.1039/DT9810001831. URL `https://doi.org/10.1039/DT9810001831`.

[70] Martin J. Buerger. *Phase Transformations in Solids*. John Wiley & Sons, New York, 1951.

[71] Martin J. Buerger. Interpretation of phase transformations in terms of structural principles. *Fortschritte der Mineralogie*, 39:9–40, 1961.

[72] Martin J. Buerger. Structural aspects of phase transitions. *Kristallografiya*, 16:1048–1054, 1971. English translation: Soviet Physics Crystallography, 16, 959 (1971).

[73] Kun Peng, Wei Ren, Ying Wu, and et al. Observation of metallic teo$_2$ thin film with rutile structure on fete surface. *Journal of Materials Science*, 57(22):10487–10494, 2022. doi: 10.1007/s10853-022-07165-0.

[74] H. J. Seifert, H. N. Nowotny, and E. Hauser. Zur struktur von cristobalit geo. *Monatshefte für Chemie*, 102:1006–1009, 1971. doi: 10.1007/BF00901438.